RALT-131

THE DETECTION AND ANALYSIS OF MUONS IN LEPTONIC DECAYS OF THE Z^0 PARTICLE AT OPAL.

Stephen James Hillier

Thesis submitted for the degree of Doctor of Philosophy

School of Physics and Space Research
Faculty of Science
University of Birmingham

February 1992

Synopsis

A description of the muon endcap detector at OPAL and an analysis of its performance is presented in the context of the process $e^+e^- \to \mu^+\mu^-$ at the LEP collider. The techniques used to identify and select muon tracks within the detector are described both at the trigger level and in subsequent data analysis. The effectiveness of the detector to contribute to the precise measurements needed to test theoretical predictions is shown.

The $\tau \to \mu\overline{\nu}_\mu\nu_\tau$ branching ratio is calculated from a study of $e^+e^- \to \tau^+\tau^-$ events in data taken at OPAL in 1990. The events are also investigated to determine the average polarisation of tau particles produced at LEP, and their forward backward polarisation asymmetry. These are used to derive a value for the ratio of vector and axial couplings of the electron and tau to the Z^0 particle and a value of the effective weak mixing angle. The main results are:

$$\begin{aligned}
B(\tau \to \mu\overline{\nu}_\mu\nu_\tau) &= 17.1 \pm 0.4 \pm 0.5\% \\
< P_{\tau^-} > &= -0.20 \pm 0.14 \pm 0.13 \\
A_{\mathrm{FB}}^{\tau^-\mathrm{pol}} &= -0.13 \pm 0.14 \pm 0.11 \\
\frac{v_\tau}{a_\tau} &= 0.10 \pm 0.07 \pm 0.06 \quad \Rightarrow \quad \sin^2\overline{\theta}_{\mathrm{W}} = 0.22 \pm 0.02 \pm 0.02 \\
\frac{v_e}{a_e} &= 0.09 \pm 0.10 \pm 0.08 \quad \Rightarrow \quad \sin^2\overline{\theta}_{\mathrm{W}} = 0.23 \pm 0.03 \pm 0.03,
\end{aligned}$$

which are all consistent with current theoretical predictions and experimental results. An investigation of polarisation correlation in the two tau particles produced in the process $e^+e^- \to \tau^+\tau^-$ is also presented.

The Author's Contribution

The size of most experimental collaborations in modern high energy physics means that most physicists spend much of their time working in a very specialised area with contact only with those close to their work. Often it becomes unclear to those outside a group (and sometimes within) exactly who is performing what tasks. In an effort to distinguish my work from that of others, a summary of my main contributions over the past 3 years is presented below.

I joined the Birmingham group about one year before colliding beams were available at LEP. At that stage, much of the muon endcap was still to be built, and I spent some time helping with the construction of parts at Birmingham and later was involved with the installation of the detector at CERN. At this stage I became involved in the data acquisition and specifically the trigger software. I programmed the trigger logic and tested the hardware, along with helping to write some of the online software. I helped in the frantic LEP start-up period to commission the muon endcap detector in time to take data with the rest of OPAL for the first physics run. After the initial running period of LEP, I became responsible for maintaining the data acquisition software through various stages of bug finding and improvements, including the addition of the patch chambers. During this time I wrote extensive monitoring packages for the readout and trigger which helped to identify occasional problems in the front end electronics.

In offline work, I started as part of the muon pair working group, where my most important contributions were writing the filter and physics selections for useful muon endcap events. I then joined the tau branching ratio working group where I worked on improving the $\tau \rightarrow \mu\overline{\nu}_\mu\nu_\tau$ analysis. The analysis presented in this thesis was mostly performed independently, although it is based on work performed by the tau group.

Acknowledgements

I would like to thank the Birmingham High Energy Physics group for providing such a friendly atmosphere in which to study. Right from the highest of the high, Professors Derek Colley and John Dowell, down to the lowliest PhD student, I have always found the department helpful and pleasant. My study would of course have been impossible without funding obtained through the SERC. I thank the education system for still supporting pure research, and I hope it continues to do so in the future.

My colleagues on OPAL are no exception to the above rule of friendliness and I would like to thank them all. I don't know how long it would have taken me to write up but for the encouragement of Pete Watkins. Pedja Jovanovic has given me useful advice over the years, both on electronics and skiing. John Wilson and Tom McMahon are equally good at asking awkward questions just when I think I've solved a problem, but at least they do it with a smile. I thank Jim Homer for introducing me to the financial opportunities of investing in rugby club prize draws. Bill Stokes achieved the impossible by making VAXes and assembler comprehensible. The other members of staff involved with OPAL, Ian Bloodworth Pete Hattersley, Mel Jobes, Richard Staley, have all done their bit to help too. Of the other staff at Birmingham, I will certainly never forget the times sitting around the coop with the OMEGA group discussing politics and life — although my lungs will probably never forgive me.

I would never have got anywhere without the help of the younger people on OPAL. I must thank Tim Smith, who often says he taught me everything I know. It's not quite true, because Nigel Watson filled me in on the rest. The muon endcap might have been very different without their presence. Dave Rees has been a good friend and helper as we struggled through the complexities of online and offline work as contemporaries. I am thankful to Alan Watson for taking on the heavy responsibility of muon endcap data acquisition expert, so that I could lead a carefree (beep-free?) existence. Matty, Jon and Nick have helped to keep work in perspective.

I thoroughly enjoyed the online work at CERN, and must thank the trigger group, particularly Ken Bell and Gunter Quast, for their patience and encouragement. The OPAL group is run in the same helpful, friendly way as Birmingham. This is in part due to the spokesman, Aldo Michelini, and also the secretaries, Mette and Sue. I also found Terry Wyatt and Keith Riles full of advice for offline work.

Now I would like to thank all those that kept my sanity intact during my long stay in Geneva and also while at Birmingham. I know I can be a bit of a pain at times, but thanks for bearing with me. Firstly I must thank some of my more long term friends. Russell and Maria in Southend are always dependable when I'm back in town. From undergraduate days, I'd be very much worse off without Mike Baker and Martin Noble, who were always happy to give me sanctuary in Cambridge and Heidelberg respectively when I needed a break. I've also been happy to keep up with Tim, Duncan and Julius, providing me with the opportunity of exploring new parts of Britain.

At CERN, my life was brightened by many people over the two years — one of the advantages of a constantly changing community. Andy Kirk stopped me from being a workaholic and taught me how to ski. Jim McNutt almost turned me into an alcoholic, and I completely failed to teach him how to ski. Mark Lehto was a good friend and skiing companion. Robert McGowan was a good friend, shame about the skiing. Simon Patton provided the service of a Mah-Jongh set and the opportunity for me to buy many drinks when I won. Roger Jones is probably forever fated to be acknowledged as a good drinking partner, and this is no exception. He also deserves some credit for introducing me to Paul and Marion, who made my return to Birmingham pleasant, and very gastronomic. My work colleagues Tim, Nige, Alan and Dave were of course also good friends. A late entry for Geneva friendships is Sandrine Orodan, who contributed to a novel and very enjoyable final trip to CERN.

When I first arrived at Birmingham, the problems of cold and potentially depressing accommodation was relieved by my contemporary students — the countless Daves, Mark and Andy. My return to Birmingham was made interesting by the 'Orlit Gang' which consisted of Richard 'Teatime' Barnes, Chris 'Morris Day' Dodenhoff, Mike 'Gilbert' Ratchet, Gareth 'Mister' Noyes and Mark 'Crusher' Whalley, who introduced me a different side of office life. I also cannot get away without mentioning Dave Evans (Conservative), with whom I've enjoyed many a good argument and whisky.

Finally my biggest thanks must go to my family. I generally take them for granted, so this is a good opportunity to thank them all for putting up with me and giving me the help and support needed to continue being a 'poor' student. Thank you Mum, Dad and Richard.

Steve, February 13th 1992, Birmingham.

Contents

List of Figures

List of Tables

Chapter 1

Physics Background

1.1 Introduction

The method of producing an accurate description of the nature of the physical universe has been guided over the years by the observation and identification of patterns of behaviour and the linking of apparently different phenomena under one conceptual framework. An historical example of this is the rationalisation of planetary motion and its connection with terrestrial gravity. In the Twentieth Century, attention has turned to understanding the fundamental nature of matter and the forces governing its interactions. Again, when experimental evidence displayed a confusing profusion of particles and phenomena, the principles of symmetry at a basic level have led to a set of theories, known as the 'Standard Model', which describes all known forces, except for gravity, in a consistent way. This model can successfully predict many of today's precise experimental results in terms of a very small number of particles which are pointlike and structureless and their mutual interactions.

Despite the success of the standard model, it is still under intense investigation by various High Energy Physics experiments around the world. These provide very careful tests of its predictions and can help to fill in gaps in the theory. One such experiment is the OPAL detector at LEP, on which some results are presented in this thesis. Firstly a brief account of the standard model is presented in this chapter.

1.2 The Standard Model

The standard model [1] is based on the principle that forces can be described by a set of quantum field theories which possess gauge symmetry and are constructed in such a way as to be renormalisable. These terms are discussed later. The forces are mediated by particles known as gauge bosons which govern the interactions between a small set of 'matter' particles called fermions. All particles in the model are believed to be structureless and pointlike, which is consistent with current experimental observations. One unified gauge theory describes the electromagnetic and weak nuclear forces, and another the strong nuclear force. The only other known force, gravity, has not yet been included in this model due to problems in its formulation as a quantum field theory, but its effect on physical properties measured in current accelerators is too small to be measurable.

1.2.1 Fermions — the Matter Particles

Fermions are distinguished from bosons in having spin-$\frac{1}{2}$ rather than integral spin in units of $\hbar$. They are the fundamental constituents of matter, although only some of them actually combine to form everyday macroscopic material. A total of 12 fermions (excluding anti-particles) has been either observed directly in experiments or implied by experimental results.

Fermions are sub-divided into two types, the leptons and the quarks, the difference being that the leptons do not undergo strong interactions. There are six leptons of which three possess electric charge (e^-, μ^-, τ^-) and the other three are the associated electrically neutral neutrinos (ν_e, ν_μ, ν_τ). The quarks similarly have two types; three have charge $-\frac{1}{3}$e (d,s,b) and the others have charge $+\frac{2}{3}$e (u,c,t). It is observed that their properties show similarities which suggest a grouping of the elementary fermions into 'generations', where each higher generation is a replica of the last, except that each member (with the possible exception of neutrinos) has a greater mass. These generations are

$$(\mathrm{e}, \nu_\mathrm{e}; u, d) \qquad (\mu, \nu_\mu; c, s) \qquad (\tau, \nu_\tau; t, b),$$

The top quark, t, is included here to complete the symmetry of the generations, although it has not yet been observed directly in experiments presumably because its mass is too high to be produced in current experiments [2]. One of the most important early results from LEP was to limit the number of light neutrinos to three [3,4], *i.e.* those already discovered, and so if it is assumed that each generation has a light neutrino, there can only be three generations.

1.2.2 Bosons — the Mediators of Interactions

Bosons have integer spin and are the gauge field quanta that mediate the fundamental forces. Quantum field theories suggest an interpretation of interactions as the exchange of virtual bosons which carry momentum and definite quantum numbers. It is therefore possible to describe not only interactions such as scattering, when only the momentum of each particle is affected, but also interactions where particles decay or new particles are created. An important feature is that the coupling of the gauge bosons to fermions has a universal strength throughout the three generations described above; this is how the symmetry of the fermions became apparent. This universality is a fundamental property of the quantum field theories used to describe the forces.

The elementary bosons found in the the standard model all have spin-1. The massless photon is the mediator for the electromagnetic force, the massive $W^{\pm}$ and Z^0 bosons are the equivalent for the weak interaction and the strong force is the result of the exchange of an octet of massless gluons. The vastly different physical properties of the photon and the intermediate vector bosons, $W^{\pm}$ and Z^0, disguise the fact that they can be described as different aspects of the same (electroweak) gauge theory. For example, the mass of the vector bosons ($>$ 80 GeV) means that the weak interaction only acts over very short distances, whereas the electromagnetic force is macroscopic.

1.2.3 Gauge Invariance in Quantum Field Theories

Originally, theories of forces were formulated by adding interaction terms into a Lagrangian for the system until the observed properties were simulated. However, quantum field theories offered a new perspective on deriving interactions [5].

Initially the fermions are introduced as complex fields in the Lagrangian. It is noted that these fields have a quantum mechanical phase which is physically unobservable. At this stage, the basic postulate of Gauge Field Theories is introduced. It is required that the Lagrangian is invariant under a space-time dependent transformation of the phase. This phase transformation is called a *local* transformation as opposed to a *global* transformation which is a constant shift at all points. Such transformations are called a gauge transformations.

Quantum field theory specifies the necessary form for a fermion Lagrangian and, when an arbitrary local gauge transformation is applied to this, extra terms are formed. This means that the original simple Lagrangian was not invariant. In order to make it gauge invariant as required, new fields are added which behave in a different way to fermions under gauge transformations. These new fields are chosen to transform in such a way that the whole Lagrangian is made gauge invariant. Now when the properties of these new fields are studied, they are are seen to correspond to the gauge bosons. The Lagrangian now also includes interaction terms which correspond to observable forces. The particles and interactions described by the new Lagrangian form the basis for calculations in this new formulation of forces — which is in general called a Gauge Theory.

There are many gauge theories that can be constructed from the basic invariance principle, only a few of which correspond to those observed in nature, but it is encouraging that all the interactions in the Standard Model can be described in terms of Gauge Theories. There is no good explanation why this should be so, but the way in which the forces fall out from a demand of symmetry at a very fundamental level has the underlying simplicity that is common to many good theories, *c.f.* the theory of relativity, which is derived from the principle that the laws of physics are independent of velocity of the observer.

The many complex aspects of interactions in nature are derived from demanding gauge invariance under operations of various symmetry groups. The way in which the fermionic field transforms in turn specifies the properties of the gauge field that is then introduced. The simplest example is Quantum Electro-Dynamics (QED) in which the transformation is that of the simplest group U(1). This introduces just one single gauge field — the photon. More complicated symmetry group transformations are needed to describe the other forces.

1.2.4 Renormalisability of Gauge Theories

The most important feature of any model is that it can make predictions which can be directly compared with observations. For quantum field theories, results have to be calculated from perturbation theory. Unfortunately, simple applications of this introduce divergent integrals into the calculations. To be able to overcome this difficulty, the infinities somehow must be cancelled out of all physical observations. This process is called renormalisation, and it can be proved that all the Gauge Theories in the Standard Model can be renormalised [6].

Consider the electron-photon vertex in a simple QED scattering process. Figure 1.1(a) shows the basic zeroth order vertex. The first order perturbation illustrated in figure 1.1(b) is well behaved and can be calculated, and its effect is seen in precisely measured scattering experiments. However figures 1.1(c) and (d) are of a different type. Here the creation of an electron-positron pair by the photon or the emission of a photon by an incoming electron are purely internal to one line of the original Feynman diagram. It is the inclusion of these diagrams that causes problems when trying to calculate additions to the lowest order graph. The momenta of the internal lines are free and so have to be integrated over an infinite range, and these integrals are found to diverge.

The solution to this problem is to 'absorb' mathematically all such diagrams into the original definition of the electron or photon lines of the Feynman graphs. For example, the infinities associated with the electrons are hidden away as unobservable 'bare' charges. The fact that the observed charge is finite can be visualised as the effect of all the virtual photonic activity surrounding the electron which corresponds to the higher order internal Feynman graphs for a single electron line. Consider an electron emitting a virtual photon which then converts into an e^+e^- pair. The charge of the electron would tend to polarise the sea of virtual pairs, thus screening the bare electron charge. One consequence of this is that the more penetrating the probe into the electron structure (*e.g.* a higher energy scattering

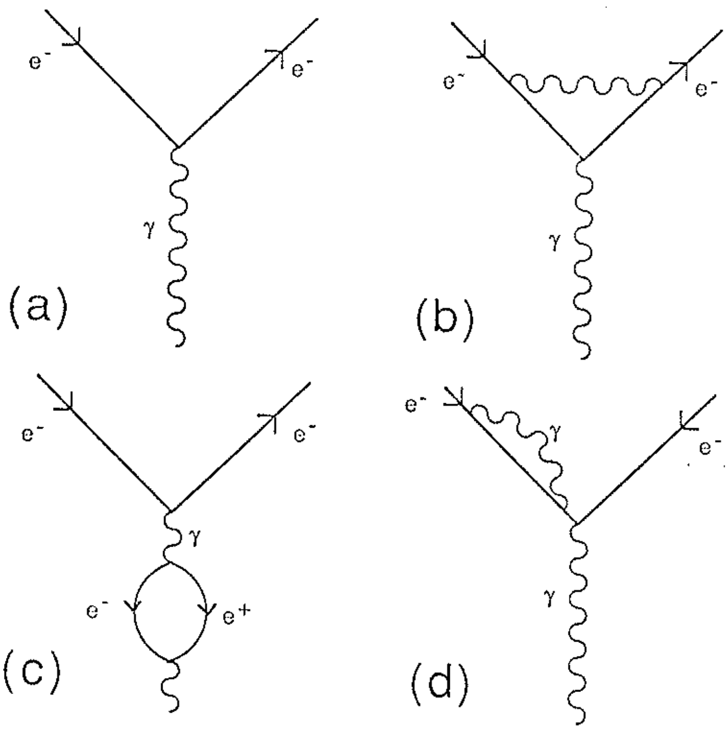

Figure 1.1: Feynman diagrams for an electron-photon vertex.

experiment), the larger the charge of the electron appears to be as the outer regions of the shielding are passed. This is accounted for in theory by having a running coupling constant, α, which increases as momentum transfer in the interaction increases.

Similar renormalisation schemes apply to all theories in the standard model, the general principle being that although many infinite quantities are introduced, anything that is actually observable is finite and calculable.

1.2.5 Electroweak Theory

The unification of the electromagnetic and weak force into one gauge theory is one of the most remarkable successes of the application of the gauge principle. The Glashow-Salam-Weinberg (GSW) theory manages to combine many very different phenomena under one framework and also make completely new predictions which, since its formulation, have been confirmed by experiments.

In order to cope with the parity violating nature of the weak interaction (described in chapter 6), it is first necessary to treat left and right handed fermions differently. The left handed fermions are grouped into weak isospin doublets, and the right handed fermions left as isospin singlets, *e.g.* the first generation becomes:

$$\begin{pmatrix} \nu_e \\ \mathrm{e} \end{pmatrix}_{\mathrm{L}} \quad \begin{pmatrix} \mathrm{u} \\ \mathrm{d} \end{pmatrix}_{\mathrm{L}} \quad \mathrm{e_R} \quad \mathrm{u_R} \quad \mathrm{d_R} \; .$$

Only the doublets are allowed to transform according to the gauge group of weak isospin, $\mathrm{SU(2)_L}$. All the fermions undergo transformation according to the weak hypercharge group $\mathrm{U(1)_Y}$. Hypercharge, Y, is defined by

$$Q = T^3 + \frac{Y}{2},$$

where Q is the electric charge and T^3 is the third component of weak isospin, *i.e.* zero for isospin singlets and $\pm\frac{1}{2}$ for doublets. Mathematically, the joint $\mathrm{SU(2)_L} \times \mathrm{U(1)_Y}$ transformation looks like:

$$\begin{aligned} \mathrm{E_L} \rightarrow \mathrm{E'_L} &= e^{ig'\frac{1}{2}\Lambda - ig\frac{1}{2}\underline{\tau}\cdot\underline{\Lambda}}\mathrm{E_L} \\ \mathrm{e_R} \rightarrow \mathrm{e'_R} &= e^{ig'\frac{1}{2}\Lambda}\mathrm{e_R} \end{aligned}$$

where $\mathrm{E_L}$ represents the left handed electron-neutrino doublet, g and g' are the weak isospin and weak hypercharge coupling constants, the $\underline{\tau}$ is a vector of three matrices forming a representation of the SU(2) group - usually chosen as the Pauli spin matrices; Λ and $\underline{\Lambda}$ are arbitrary variables that define the transformation.

When invariance of the fermionic Lagrangian is required, it is found that four new fields must be introduced, and their transformation properties are defined. Three of these fields, W^1, W^2 and W^3, couple to the weak isospin current whereas one, B^0, couples only to the weak hypercharge. It is found that when suitable linear combinations of W^1 and W^2 are taken, the correct parity violating properties of the physical $\mathrm{W^{\pm}}$ particles emerge from the theory. All that remains is to pick out the properties of the neutral weak current, $\mathrm{Z^0}$, and the photon, A. The W^3 couples only to left handed fermions and therefore cannot be directly associated with the $\mathrm{Z^0}$ particle which couples to all fermions. However, a linear combination of the theoretical fields leads to a description of the physical fields of both the $\mathrm{Z^0}$ and the photon:

$$\begin{aligned} \mathrm{Z} &= W^3\cos\theta_{\mathrm{W}} - B\sin\theta_{\mathrm{W}} \\ \mathrm{A} &= W^3\sin\theta_{\mathrm{W}} + B\cos\theta_{\mathrm{W}}. \end{aligned}$$

The mixing is characterised by the weak mixing (or Weinberg) angle, θ_W. This mixing angle then governs the relative strength of the weak and electromagnetic forces:

$$g \sin \theta_W = e = g' \cos \theta_W.$$

It is one of the most important parameters that can be measured in current experiments.

When the full Lagrangian is investigated, it is found that further interaction terms have been introduced which correspond to interactions between the gauge fields themselves. These appear because of the non-commutative nature of the transformation groups (otherwise known as non-Abelian). It is a feature of non-Abelian theories that these self-interaction terms appear, unlike in QED, where the photon has no charge and so cannot interact with itself.

1.2.6 The Higgs Mechanism

Buried in the mathematical formalism of the electroweak gauge field theory is one major problem — the model only works for massless particles. When mass terms are added into the Lagrangian, its gauge symmetry is lost. This might not be such a problem in itself except that the gauge invariance is intrinsically linked with the renormalisability of quantum field theories, and so the predictive value is lost. The solution is the introduction of a further field, called the Higgs field, which allows the possibility of having a 'spontaneously broken symmetry'. The meaning of this is that the Lagrangian is still ultimately symmetrical, but in the vacuum state the gauge symmetry is broken allowing particles to have mass. The underlying symmetry is still sufficient to make the theory renormalisable [7].

In order to visualise this it can be imagined that the added Higgs field has a symmetrical self-interaction potential as in:

$$V(\phi^* \phi) = -\mu^2 \phi^* \phi + \lambda (\phi^* \phi)^2.$$

This is obviously symmetrical about the origin, but if both μ^2 and λ are positive, then the origin is a local maximum of the potential. There is an infinite set of minima at $|\phi|^2 = \mu^2/2\lambda$. By choosing one of these as the vacuum state, the symmetry is broken.

In fact, in the minimal model, four Higgs fields are introduced in the form of an isospin doublet of complex scalar fields. Careful choice of the couplings and the vacuum state results in the vacuum developing weak isospin and hypercharge. Other particles can then couple to this field and mass terms are generated. Furthermore it is found that by combining three of the Higgs fields with the weak bosons, the $W^{\pm}$ and Z^0 particles become massive as required and only one Higgs scalar remains. Thus the Higgs model provides a mechanism to allow particles to have mass, although there is no prediction of what these masses should be. One problem is that it introduces an extra undiscovered particle, the neutral Higgs boson. Again there is no mass prediction for this boson, although its interactions can be calculated if the mass is known. The only mass relation given by the Higgs mechanism is that between the $W^{\pm}$ and Z^0 masses:

$$M_W = M_Z \cos\theta_W.$$

This relation can be tested experimentally, and a search made for the Higgs boson. To date no candidate Higgs has been found and its mass is constrained to be greater than about 40 GeV [10].

1.2.7 Quantum Chromodynamics

The other major theory in the standard model is Quantum Chromodynamics (QCD) which governs the strong interaction. It is based on the symmetry group SU(3) of colour. This colour is the 'charge-like' quantum number carried by all quarks, which can be one of three colours (R, G or B). It is thought that only particles which are 'colourless' (*i.e.* colour singlets) can be observed directly and so quarks, which are always coloured, cannot exist on their own. This is called colour confinement and is a consequence of the nature of the strong force at long range, as described below.

When developing the gauge theory of QCD, an octet of coloured gauge bosons appears; these are called the gluons. Gluons can interact with each other as well as with quarks. In contrast to QED, the strong coupling constant varies with energy such that it is large in small momentum transfer interactions. In fact it is too large to allow satisfactory perturbation calculations to be performed for QCD in low momentum interactions ($\alpha_s \sim 1$). However at higher momentum transfers, such as in high energy scattering, sensible predictions are possible from perturbation theory. This feature of QCD is also shown by the fact that the strong force increases with distance, whereas at small distances the coupling is very small — this is known as asymptotic freedom.

The problem of the large coupling constant makes QCD less predictive than Electro-Weak theory. However, it is still possible to calculate interactions at small distances. For example, in e^+e^- annihilation to form a quark-antiquark pair, interactions just after the initial creation, such as gluon 'radiation', can be calculated. However, when the quarks subsequently separate and undergo fragmentation into observable particles which spread out to form a 'jet' of charged tracks, the composition of this jet can only be modelled empirically.

1.3 LEP — Exploring the Standard Model

Despite the success of the standard model, there are still many unsatisfactory features, not least the necessity of introducing many arbitrary constants which must be measured experimentally. Even assuming that the top quark and Higgs boson are eventually found at higher energies, the standard model still requires precise verification in order to confirm its position as the best theory available.

The initial LEP operation at centre of mass energies around the Z^0 mass offers a unique opportunity to study the electroweak processes with high statistics. Also many other aspects of the standard model and extensions to the standard model can be studied. A comprehensive review of the possibilities for physics analysis is given in [8]. In the first years of LEP running some of the major objectives have already been achieved — perhaps the most important result being that there are only three light neutrinos.

There are four detectors at LEP taking data on the production and decay of the Z^0. They all produce independent results and thus a good cross-check of

Measured Parameter	Units	Standard Model Prediction	Averaged LEP Result
Z^0 mass	GeV	—	91.175 ± 0.021
Z^0 width	MeV	2494 ± 12	2483 ± 10
Z^0 hadronic width	MeV	1742 ± 11	1736 ± 10
Z^0 electronic width	MeV	83.8 ± 0.4	82.9 ± 0.6
Z^0 muonic width	MeV	83.8 ± 0.4	84.4 ± 1.0
Z^0 tauonic width	MeV	83.8 ± 0.4	83.5 ± 1.1
Z^0 leptonic width (assuming universality)	MeV	83.8 ± 0.4	83.3 ± 0.4
Z^0 invisible width	MeV	500.0 ± 6.0	497.3 ± 9.8
Z^0 hadronic pole cross section	nb	41.40 ± 0.10	41.38 ± 0.29
$\sin^2\theta_W$		—	0.2328 ± 0.0013

Table 1.1: A summary of LEP results in comparison the theory.

each experiment's findings can be made. The results can also be combined to form a better final averaged measurement. A summary of various electroweak parameters and properties of the Z^0 boson calculated from such a combination of LEP results is found in table 1.1. Where possible, standard model predictions are given (assuming three fermion generations) showing the remarkable agreement between theory and experiment. All figures are quoted from [9].

Other results obtained from LEP include lower limits on the masses of the Higgs boson and supersymmetric particles [10,11]. These particles would be directly produced at LEP if kinematically allowable. Some theoretical limits can be placed on the top quark mass from lineshape studies [4]. Its mass is already constrained to be greater than 89 GeV at 95% confidence level by other investigations [2], and so direct production at current LEP energies is impossible, but accurate measurements of couplings and mass of the Z^0 give an insight into higher order Feynman diagrams including virtual top quarks. The mass limit on top from a combination of such studies is $m_t = 137 \pm 40$ GeV. Much investigation is also performed into the nature of QCD. For example it is possible to measure the value of the QCD coupling constant at LEP energies, $\alpha_s = 0.118 \pm 0.008$. This is performed by an observation of the ratio of two to three jet multihadronic events which is dependent on the cross-section for gluon radiation [12].

Chapter 2

The LEP Collider and Experiments

The experimental needs of High Energy Particle Physics nowadays require the construction of large and sophisticated machines built by large collaborations of physicists, engineers and technicians. Although any one physicist involved is generally only an expert in a very limited area of these projects, some knowledge of the other parts is needed in order to perform physics analysis. This chapter gives an overview of both the LEP accelerator and OPAL detector to form a background for the later chapters.

2.1 The LEP Collider

The LEP project at CERN is the latest in a series of e^+e^- colliders built at various laboratories around the world, each generally reaching higher energies than the last. The new energy region around 90 GeV initially explored by LEP is particularly important because of the presence of 'new physics' in the form of the Z^0 resonance. Also it is intended to upgrade LEP after some time to higher energy regions (up to 200 GeV) in order to investigate new effects in that region, *e.g.* the $Z^0 \rightarrow W^+W^-$ vertex.

The LEP synchrotron [13] consists of a ring which is about 26.7 km in circumference where the electron and positron beams rotate in opposite directions within a vacuum pipe. The shape of the ring is octagonal with very rounded corners and its size is governed by the need to minimise loss of beam energy by synchrotron radiation. During a normal running period, four bunches each of electrons and positrons circle the ring continuously, and they cross at 8 points around the ring, although only 4 of these points are instrumented with detectors.

Electrons are stripped from a heated filament and accelerated in the LEP Injector Linac (LIL) to 200 MeV to collide with a target, where the deceleration produces bremstrahlung photons which undergo pair production to e^+e^-. The positrons are separated using a magnetic field, and these are accumulated along with electrons in the Electron Positron Accumulator (EPA) ring at about 600 MeV. After sufficient current has accumulated, the beams are injected successively into the older CERN systems of the PS, to be accelerated to 3.5 GeV, and then the SPS to reach 22 GeV before the final injection into LEP.

Once in LEP the beams are accelerated to full energy by copper radio frequency (RF) cavities coupled to spherical storage cavities called klystrons. From 1989 when LEP first produced collisions and for some years yet, the typical working energy will be around the Z^0 peak at 91 GeV. At these energies the energy loss of one electron or positron per cycle is about 250 MeV. This means the accelerating cavities also have to boost the energy of the beams when they are 'coasting'. This energy loss becomes even more of a problem at the planned higher energies meaning that superconducting cavities will have to built for this purpose in the second stage of LEP.

Essentials for the beam to maintain effectiveness over a long period are the accuracy of the magnets and the vacuum in the beam pipe. There are almost 2000 focusing magnets and over 3000 bending magnets which occupy the majority of LEP's 27 km length. The beam pipe is evacuated to a pressure of less than 3×10^{-9} torr, which reduces beam loss due to collisions with gas particles.

The precision of the apparatus can be judged by the fact that a beam can be maintained for typically six hours while maintaining a high luminosity. Typical luminosities achieved in the second year of running were about $4.5 \times 10^{30}\mathrm{cm}^{-2}\mathrm{s}^{-1}$ and, at best, event rates of about ten Z^0 decays in a minute were observed at OPAL.

The LEP accelerator also has to provide an accurate measurement of the beam energy, which is half the centre of mass energy in the e^+e^- annihilation. One of the major systematic errors on measurements such as the mass of the Z^0 comes from the precision on the absolute energy from LEP. The value of the centre of mass energy in 1990 was known to about 20 MeV, comparable to statistical and other systematic errors for each experiment in that year. With increased statistics and combination of the four detectors results, this becomes by far the dominant error. It is hoped that better calibration will be possible in the future by a measurement of the depolarisation resonance frequency — the error then could be as little as 7 MeV.

2.2 The LEP Detectors

There are four major detectors at LEP which have been operating since the commissioning of the collider in August 1989. These generally consist of a large volume of various layers of sub-detectors surrounding the interaction points as fully as possible. The four experiments — ALEPH [14], DELPHI [15], L3 and OPAL [16] — are built with generally the same aims in mind, and so are quite similar, following the lines of detectors at previous e^+e^- colliders such as PETRA. They each have a tracking chamber in a solenoidal field for identifying charged tracks, a calorimeter for measuring electromagnetic and hadronic showers and an outer tracking layer used for muon detection.

However the experiments do differ considerably in detail. For example OPAL and ALEPH are both built as general purpose detectors, with good resolution for all particles. However OPAL is based on more conventional technology, whereas ALEPH uses apparatus that was more innovative at the time of proposal, such as the Time Projection Chamber (TPC) for tracking. DELPHI is even more advanced with its ambitious sub-detectors such as the Ring Image Cerenkov (RICH) for particle identification. L3 concentrates its effort into very good leptonic identification and measurement. The advantage in having four LEP detectors is that independent results can be obtained with often different systematic errors, giving eventually a more precise measurement of the various physics parameters. Also the different capabilities of each detector allow them to concentrate on particular fields of research with better results.

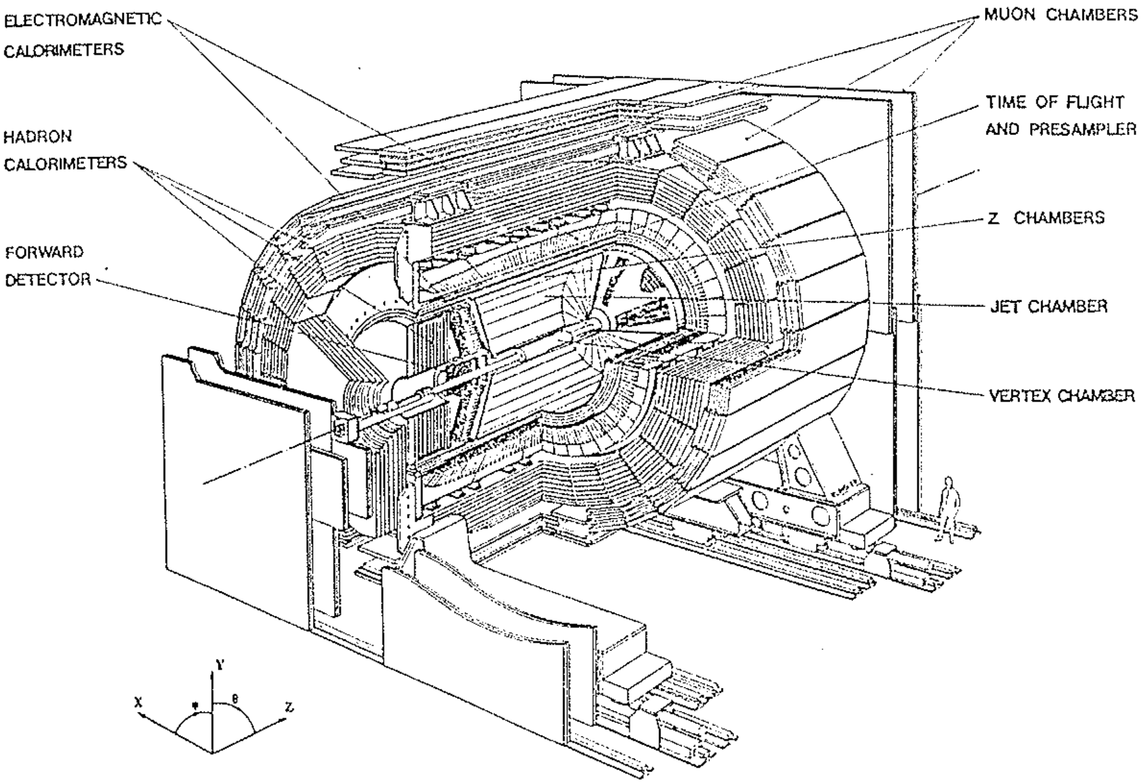

Figure 2.1: A perspective view of the OPAL detector.

This thesis concerns work on one of these detectors, the Omni-Purpose Apparatus for LEP (OPAL) which can be seen in Figure 2.1. The rest of this chapter describes this detector in more detail.

2.3 The OPAL Detector at LEP

OPAL is designed to be a general purpose detector with good overall particle identification and energy resolution. It has very good angular acceptance over almost 4π around the vertex, in which it is possible to identify exclusively almost all the e^+e^- interactions occuring in the detector. The detailed layout of the subdetectors in OPAL can be seen in figure 2.2. The individual elements are described below.

2.3.1 Obtaining Physics Information from OPAL

The heart of a LEP detector is the central tracking chamber, where precise measurements of charged track parameters can be made. The wire chambers in OPAL

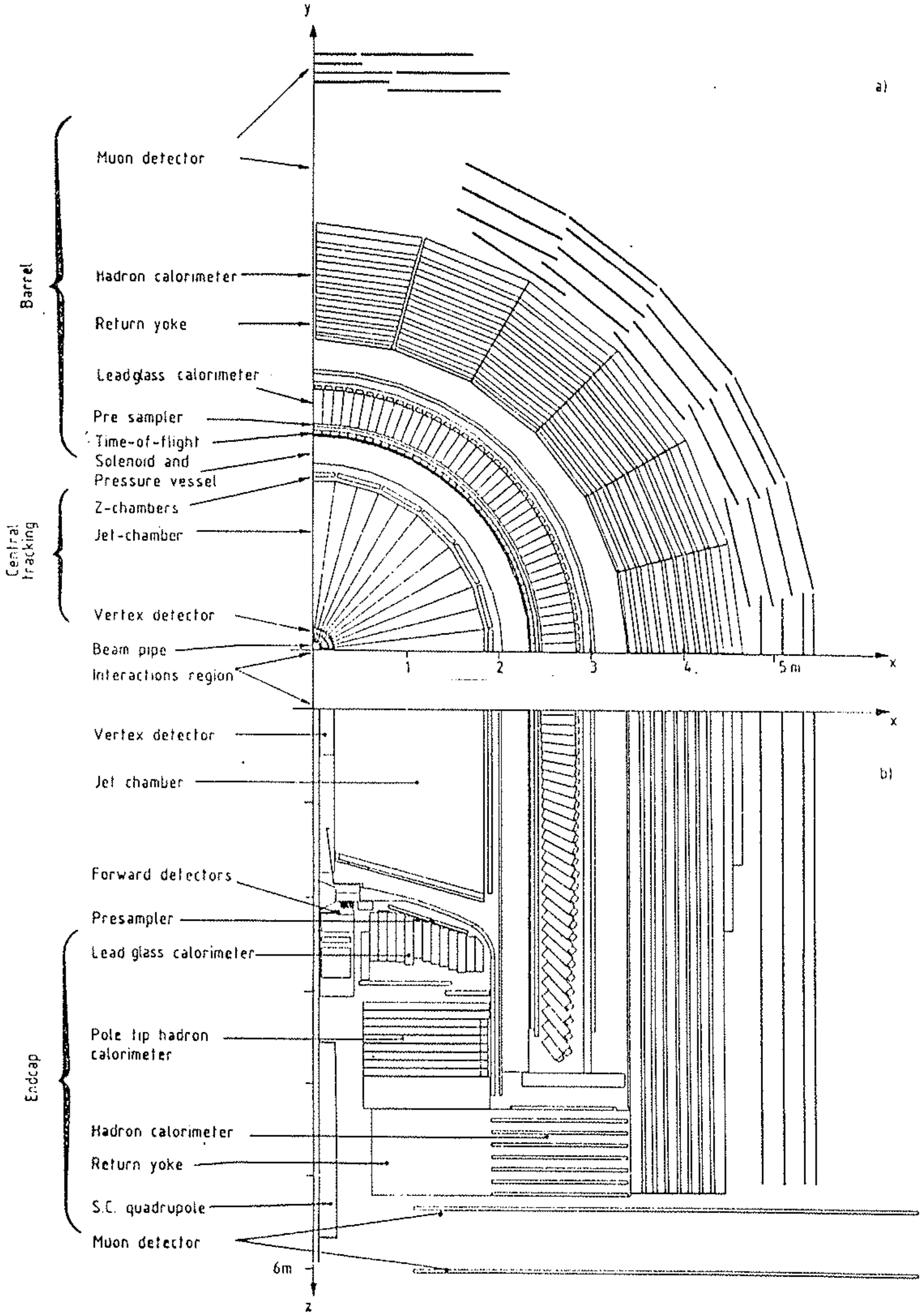

Figure 2.2: Cross section of the OPAL detector showing how the sub-detectors fit together.

are surrounded by a warm coil solenoid producing a 0.435 T field throughout the tracking volume. Thus the momentum of charged tracks can be measured along with the charge from the direction and radius of curvature of the reconstructed trajectories. Along with a knowledge of the magnitude of ionisation ($\frac{dE}{dx}$), an attempt at particle identification can be made.

Outside the central detector, beyond the solenoid, are the calorimeters. Lead glass blocks form about 25 radiation lengths of electromagnetic calorimetry for identification and energy measurement of electrons and photons, and then several layers of chambers fitted between thick slabs of iron doubling as the return yoke of the magnet form the hadron calorimeter, for hadronic energy measurement.

Finally outside the minimum of six interaction lengths of material, there are four layers of muon detectors, which detect any charged particles that have escaped the rest of the detector. These are generally muons, although there will be contamination from hadronic punch-through and sneak-through. Both position and direction are recorded in order to match these tracks with their signals in the inner tracking chambers.

In the very forward region around the beampipe a complex series of calorimeters and wire chambers form the forward detector, essential in luminosity monitoring from the $e^+e^- \rightarrow e^+e^-$ scattering reaction (referred to as Bhabha scattering).

The signatures of some particles as they pass through the detector are illustrated in Figure 2.3, showing how easily some particle differentiation can be achieved. The situation is not always quite so clear, especially when there are many charged and neutral particles in the same region. Therefore sophisticated analysis techniques have to be developed along with Monte Carlo simulations of detector response to understand the more complicated event types.

A detailed description of each of the sub-detectors can be found in the OPAL technical paper [16]. Below a summary is given of each component

2.3.2 Standard OPAL Co-ordinate System and Definitions

The OPAL co-ordinate system is a right-handed Cartesian system with the origin at the centre of the jet chamber, z axis in the direction of electrons in LEP and

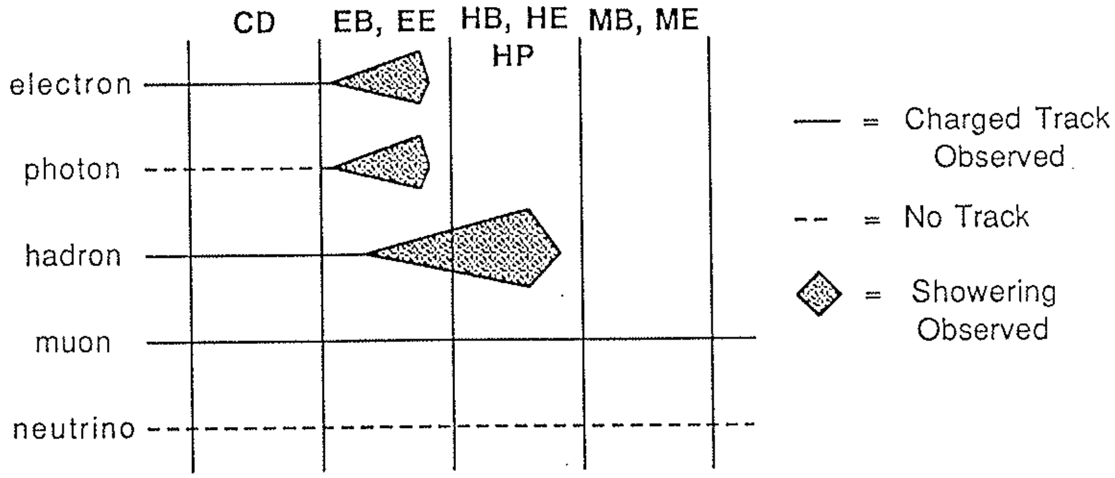

Figure 2.3: Particle differentiation by behaviour in sub-detectors.

θ bin	$\cos(\theta)$ range	ϕ bin	ϕ range
1	-0.980 – -0.596	1	0^o – 30^o
2	-0.823 – -0.213	2	15^o – 45^o
3	-0.596 – 0.213	3	30^o – 60^o
4	-0.213 – 0.596	....	....
5	0.213 – 0.823	23	330^o – 360^o
6	0.596 – 0.980	24	345^o – 15^o

Table 2.1: Standard OPAL trigger θ-ϕ bins.

x axis towards the centre of LEP. This makes make the y axis almost vertical — the LEP ring being slightly inclined to the horizontal. Also the angles θ and ϕ are used. The azimuthal angle, ϕ, is measured about the z axis with $\phi = 0$ along the positive x axis. The polar angle, θ, is measured from the positive z axis. For the purposes of the trigger, the detector is divided into 144 overlapping θ-ϕ bins. These are defined in table 2.1.

Two commonly used track parameters, d_0 and z_0, relate to the proximity of the extrapolated track to the collision point. The impact parameter, d_0, is defined as the distance of closest approach to the origin in the r-ϕ plane. In the OPAL definition it is assigned as positive if the curvature of the track encloses the origin and negative otherwise. The z coordinate at the point of closest approach in the r-ϕ plane is defined as z_0.

2.3.3 The Central Detector

In 1989 and 1990, this consisted of three distinct parts, located outwards from the beampipe to the inner edge of the solenoid. They are drift chambers of varying geometries which are all surrounded by a pressure vessel containing 88.2% argon, 9.8% methane and 2.0% isobutane at a pressure of 4.0 atmospheres. The overall purpose of the three detectors is to measure the momenta, positions and impact parameters of all charged tracks in an event in three dimensions. Also an indication of particle type is deduced from the rate of ionisation in the gas.

The three sub-detectors in the central detector each specialise in different aspects of the tracking process. The innermost vertex detector located just outside the beam pipe is designed to give the best measurement of the impact parameter, d_0, and to locate decay vertices of short lived particles. It also helps to improve momentum resolution. The large jet chamber performs tracking over a large angular range in order to provide accurate measurements of curvature and energy loss in the gas. However the z coordinate measurement in the jet chamber is intrinsically less accurate than measurement in the r-ϕ plane, so it is surrounded by the z-chambers which improve the z measurement. This is necessary both for matching with outer detectors and for invariant mass calculations. The z-chambers only cover the barrel region of OPAL, but to improve z resolution in the endcap, the end-point algorithm can be used. This uses knowledge of the last wire hit in the jet chamber to indicate where the charged particle passed out of the active region and into the instrumentation and pressure vessel. The location of the end of the wire is well known, and using this coordinate and the position of the event vertex gives a good measurement of the azimuthal angle of the track.

The quality of track measurement has been improved continually as better calibration techniques and algorithms were used, leading to better momentum and impact parameter resolutions. The data used in this thesis were taken in 1990 and the resolutions quoted are those found in these data.

Vertex Chamber (CV)

This cylindrical drift chamber is about 1 m in length and 470 mm in diameter. It consists of two separate volumes, the inner with wires parallel to the beam axis, and the outer with so called stereo wires which are angled at about 4^o to this axis in order to measure the z coordinate. Both regions are segmented in 10^o intervals, and they give accurate azimuthal information from drift times to reach the sense wires centred in each of the 36 segments. Also some z information is obtained from time differences at the two ends of the sense wires.

The main purpose of this sub-detector is to obtain accurate impact parameters, d_0. The resolution in the r-ϕ plane was 41 μm in 1990, and the inclusion of vertex chamber hits on a jet chamber track improved the resolution in the r-z plane from 27 mm to 1.7 mm.

Jet Chamber (CJ)

The Jet Chamber is a conventional tracking drift chamber, based heavily on that used in the JADE detector. It is built on a large scale having an outer radius of almost 2 m and a maximum length of about 4 m, narrowing towards the inner radius. There are 24 radial planes of sense wires set parallel to the beam axis. The wires are spaced at 10 mm intervals giving 159 measured space points for a charged particle passing through the barrel region of the detector — up to $|\cos\theta| = 0.731$. Reasonable tracks can still be reconstructed down to $|\cos\theta| = 0.98$ where the particles just pass through the first few wires near to the end-bell.

The sense wires are interspersed with grounded anode wires, the sense wires being offset alternately from the anode wires to resolve left-right ambiguities. Bisecting the region between anode planes are the cathode wires, maintained at a voltage increasing with radius in order to produce a uniform electric drift field for the ionized particles. The signals from the sense wires are digitised at each end and drift time used to determine the position in the r-ϕ plane. Charge division between the two ends is used to give an approximate z coordinate. Integration of the signal can also be used to give $\frac{dE}{dx}$ for the particles.

The jet chamber alone gives good track trajectories (*e.g.* ± 135 μm in r-ϕ and

± 6 cm in z), but more important is the resolution when combined with the Vertex Detector above and the Z Chambers described below. The momentum resolution is about 8% at maximum energies of about 45 GeV and better at lower momenta.

Z Chambers (CZ)

Around the barrel of the Jet chamber, and just within the magnet, lies a layer of drift chambers called the Z chambers. There are 24 chambers, each 4 m long divided lengthwise into eight 50 cm by 50 cm units which are 59 mm thick. There are six sense wires in each unit which are aligned perpendicularly to the z-axis. This means that drift times give an accurate measurement of the z coordinate and charge division is used to determine ϕ in this case. These measurements are used to match the hits in the Z chambers to tracks from the other central detectors.

The eventual resolution in z turns out to be limited by the survey of chamber positions to 300 μm, whereas the intrinsic chamber resolution is around 150 μm and the r-ϕ resolution is 1.5 cm. In data, it is observed that tracks with matched hits from these chambers have a greatly improved resolution in z.

2.3.4 The Time of Flight System

The Time of Flight sub-detector (TOF) consists of 160 scintillation counters surrounding the coil in the barrel region out to $|\cos\theta| = 0.82$. They are primarily intended as a fast trigger, but also the timing information helps to identify particles and is especially useful in rejecting out of time particles from cosmic rays. Each counter is 6.84 m in length with a thickness of 45 mm, and signals are detected by phototubes at both ends. Test chamber data show that it should be possible to achieve a time resolution of 350 ps, with the possibility of an even better resolution if z information from other detectors is used. Current accuracy for $e^+e^- \to \mu^+\mu^-$ events is 460 ps compared to a typical flight time of 10 ns for a relativistic particle travelling from the interaction point.

2.3.5 The Electromagnetic Calorimeter

There are four separate detectors dedicated to giving an accurate energy measurement of the electromagnetic showers of electrons, positrons and photons. These are split into the calorimeters themselves, made of lead glass in which most of the shower occurs, and the presamplers which sample the showers originating in the coil to increase the accuracy for these pre-showered events. There is an average of 2 radiation lengths (2 X_0) of material in front of the presamplers. All detectors outside the coil are divided into those surrounding the barrel, which are cylindrical in shape, and those covering the more forward region which generally have more complicated geometry. The array of lead glass, along with calorimeters in the Forward Detector, form an almost complete 4π coverage for electromagnetic showers.

The electromagnetic showers are caused by a combination of pair production and bremsstrahlung of electrons and positrons induced by the presence of heavy nuclei, in this case the lead in lead glass. Cerenkov radiation is caused by particles travelling faster than the speed of light in the glass, and this light is then detected by photomultiplier tubes. The amount of radiation collected is proportional to the energy deposited to a good level of approximation. The position and shower shape are also determined by measuring the sharing of showers between blocks.

Presampler Barrel (PB)

This consists of a double layer of streamer tubes covering up to $|\cos\theta| = 0.81$. The readout is taken from the wires which lie parallel to the z axis and from charge induction on strips lying at 45^o to the wires. Although they were not used for shower energy correction in 1990, they do give an accurate position for single particles (about 2 mm resolution for minimum ionising particles). Investigations suggest that they could reduce the degradation of energy resolution for low energy particles (around 5 GeV) by a factor of two.

Presampler Endcap (PE)

This consists of multiwire proportional chambers fixed to the surface of the electromagnetic endcap covering $0.83 < |\cos\theta| < 0.95$. Readout is performed on the wires, which lie perpendicular to the beam axis, strips running radially on one side of the chambers. Again, data from this detector were used only for positional information in 1990, the position resolution being 4 mm.

Electromagnetic Barrel (EB)

The complete solid angle up to $|\cos\theta| = 0.82$ is covered by an array of 9,440 lead glass blocks each 37 cm long corresponding to 24.6 X_0. The individually shaped blocks are segmented into 59 rings of 160 blocks, fitting tightly together to minimise gaps in the coverage. They are aligned accurately such that each block points to a point slightly to one side of the interaction point in order both to confine showers within blocks and to avoid the problem of particles escaping through cracks between blocks. Each block subtends about $1.9^o \times 1.9^o$ from the interaction point.

The blocks are located in a region where there is only a small residual magnetic field, and so conventional phototubes can be used. The barrel lead glass can achieve an energy resolution of $\frac{\sigma_E}{E} = \frac{6.3\%}{\sqrt{E}} + 0.2\%$ (where E is the energy of the incident particle in GeV), although it is a little worse in practice with the pre-showering of particles. The spatial resolution is about 11 mm from using shower profiles.

Electromagnetic Endcap (EE)

The remaining angular region up to $|\cos\theta| = 0.98$ is filled by two dome-shaped 'plugs' which fit snugly into the end-bell of the central detector pressure vessel. Each consists of an array of 1,132 blocks, all aligned parallel with the beam-pipe. These vary in length due to geometrical constraints, but give an interaction length of at least 20.5 X_0, usually more.

Due to the large magnetic field surrounding this sub-detector (almost the full 0.435 T), new devices known as vacuum photo triodes were developed for readout, as conventional photomultipliers would not work in these conditions. The intrinsic energy resolution is $\frac{\sigma_E}{E} = \frac{5.0\%}{\sqrt{E}}$ with a similar spatial resolution to the barrel, although the position has to be carefully calibrated with energy and particle type due to the differences in shower development in the non-pointing block geometry.

2.3.6 The Hadron Calorimeter

The purpose of this calorimeter is to measure the profile and energy of showers caused by hadronic particles emerging from the back of the electromagnetic calorimeter and to help in identification of muons. It consists of between 8 and 10 layers of chambers which are embedded in the iron return yoke of the OPAL magnet. The iron forms at least 4 interaction lengths of material over 97% of 4π, adding to the average of 2.2 interaction lengths formed by the inner parts of the OPAL detector. This ensures a good angular coverage for the measurement of hadronic showers and also reduces the background of fake muons reaching the outermost muon detector.

The calorimeter works by sampling the shower development at regular intervals through the iron return yoke. The exact geometry is limited by the shape of the detector. The barrel (HB) (up to $|\cos\theta| = 0.81$) consists of a cylindrical array of 9 active detector layers alternating with eight 10 cm thick slabs of iron. The sense wires in the chambers run parallel to the beampipe. In the endcap (HE), which extends the coverage to $|\cos\theta| = 0.91$, seven layers of iron lie within the eight vertical chambers forming a 'doughnut' shaped plug at each end.

Both the barrel and endcap are instrumented with streamer chambers containing 75% isobutane and 25% argon running at around 4.5 kV in the limited streamer mode. They are read out by measuring signals induced by streamers on the conducting surfaces surrounding the gas tubes. On one side lie aluminium strips running parallel to the wires, and the other side has large pads of conducting material. These pads are shaped in such a way that they form towers of readout regions when combined with pads from other layers. The towers point back to the interaction point so that the energy of hadronic showers can be measured by summing the signals in the towers in the region of the shower. The strip readout gives both information about shower profiles and tracking information on muons passing through the calorimeter.

The angular coverage is completed by the Hadron Poletip (HP) which covers angles down to $|\cos\theta| = 0.99$. This is of a slightly different design to the rest being made of 10 layers of very thin (10 mm) proportional chambers situated in the magnet poletip, nearer to the interaction point than the endcap. The readout is arranged similarly into pads and strips.

The energy resolution of the hadron calorimeter is limited by the large amount of material in front of the detector. The electromagnetic calorimeter itself has poor resolution for hadronic showers originating within its volume. However, by combining information with that from the two calorimeters, an energy resolution of approximately $\frac{\sigma_E}{E} = \frac{120\%}{\sqrt{E}}$ can be achieved.

2.3.7 The Muon Detector

The main objective of this detector is the identification of muons, being particularly important in assisting to distinguish a muon in a background of hadrons. Essentially it consists of just four layers of chambers sensitive to any charged particles at the very outer surface of OPAL. They can measure the position and direction of tracks and cover about 94% of 4π, the gaps being necessary for support structures and cabling for the inner detectors and magnet.

Most hadrons are absorbed in the calorimeters: only about 0.1% of hadrons reach the muon detectors without interacting. Other backgrounds come from secondary interactions of hadrons and decays to muons. In these cases tracking can help to reject muons not originating at the interaction point, *e.g.* by comparing the position and direction in the Central Detector with that measured in the Muon Chambers, allowing for multiple scattering in the calorimeter and bending in the magnetic field. Thus rejection of many of the non-muon charged tracks is achieved while at the same time maintaining a very high efficiency for genuine muons. Essentially all muons with an initial energy higher than that necessary to pass through the hadron calorimeter (about 3 GeV) are observed by the muon detector, if they fall in its geometrical acceptance.

The detector is divided again into barrel and endcap, with the barrel covering up to $|\cos\theta| = 0.69$ and the endcap covering the remaining solid angle right up to $|\cos\theta| = 0.98$.

Muon Barrel (MB)

This consists of up to four layers of drift chambers forming a cylindrical casing around the Hadron Calorimeter Barrel. Each unit is 1.2 m wide and 90 mm thick and up to 10.4 m long, some being shorter due to geometrical restrictions of support structures. Each unit consists of two chambers side by side each with one sense wire in the centre, so the drift distance in the r-ϕ plane is up to 30 cm. The drift time is used to measure this coordinate to an accuracy of 1.5 mm. The z coordinate is found using a new system combining charge division with readout from diamond shaped cathode pads which also gives a resolution of 1.5 mm.

Muon Barrel (ME)

The muon endcap consists of four layers of chambers allowing charged particles to be tracked through the ends of OPAL. It extends the muon detector coverage up to $\cos\theta = 0.98$ and consists of large vertical 'walls' of streamer chambers. Signals are read out by charge induction onto strips perpendicular and parallel to the sense wires. It is described in more detail in the next chapter.

2.3.8 The Forward Detector

The main purpose of the forward detector (FD) is to give a precise luminosity measurement using small angle Bhabha scattering. This luminosity is necessary for many of the analyses performed at LEP. It can also be used to tag two photon events. It consists of a complex combination of calorimeters and tracking chambers which surround the beampipe on both sides of the interaction point at various points along its length, the greater part being between 2-3 m from the centre.

The detector covers a polar angle range from 40 to 220 mrad, but the cleanest acceptance lies between 47 and 120 mrad. In this region there is a high cross section for Bhabha scattering, and this cross section can be calculated precisely from theory. The acceptance is limited to an accurately calibrated and well understood region of detector in order to reduce systematic errors on the measurement of the absolute luminosity.

The major part used for luminosity calculation in 1990 was the calorimeter, a lead-scintillator sandwich with 35 layers adding up to 24 radiation lengths, within which lie three layers of proportional chambers giving an accurate position measurement. In 1989, using the redundancy of just these detectors gave an accuracy of 2.2% in the absolute luminosity. In 1990, the luminosity measurement was improved by better calibration of the calorimeter and proportional chambers and helped by the inclusion of data from other parts of the forward detector, such as the drift chambers and fine luminosity monitors, positioned in front of the calorimeter. From careful cross-checking of measurements, the systematic error on the luminosity was reduced below 1%.

2.3.9 The OPAL Trigger

LEP provides e^+e^- bunch crossings at a rate of about 45 kHz, corresponding to a delay between bunch crossings of 22 μs. With this time delay it is possible to form a single level trigger decision between two crossings. If the event is of no interest then the sub-detectors are sent a signal to reset to be ready for the next crossing. Alternatively, if the trigger indicates a potential physics event, the whole detector is read out. This inhibits triggering on any more events until all detectors are ready again. Since the process of digitising all the signals in OPAL in 1990 took on average about 20 ms, it was necessary to keep the trigger rate at a reasonably low level. Typically in 1990 it was 2-3 Hz, meaning that barring other problems, the detector was only inactive for about 5% of the beam time.

The OPAL trigger [17] is designed to give a very high efficiency for all useful physics events. In fact for most interesting channels it is practically 100% efficient. However, in order to keep the trigger rate at acceptable levels, the trigger logic must be sophisticated enough to reject common backgrounds such as beam-gas or beam-wall interactions and activity caused by cosmic rays. This is done by having a complex software programmable central logic combining trigger information from

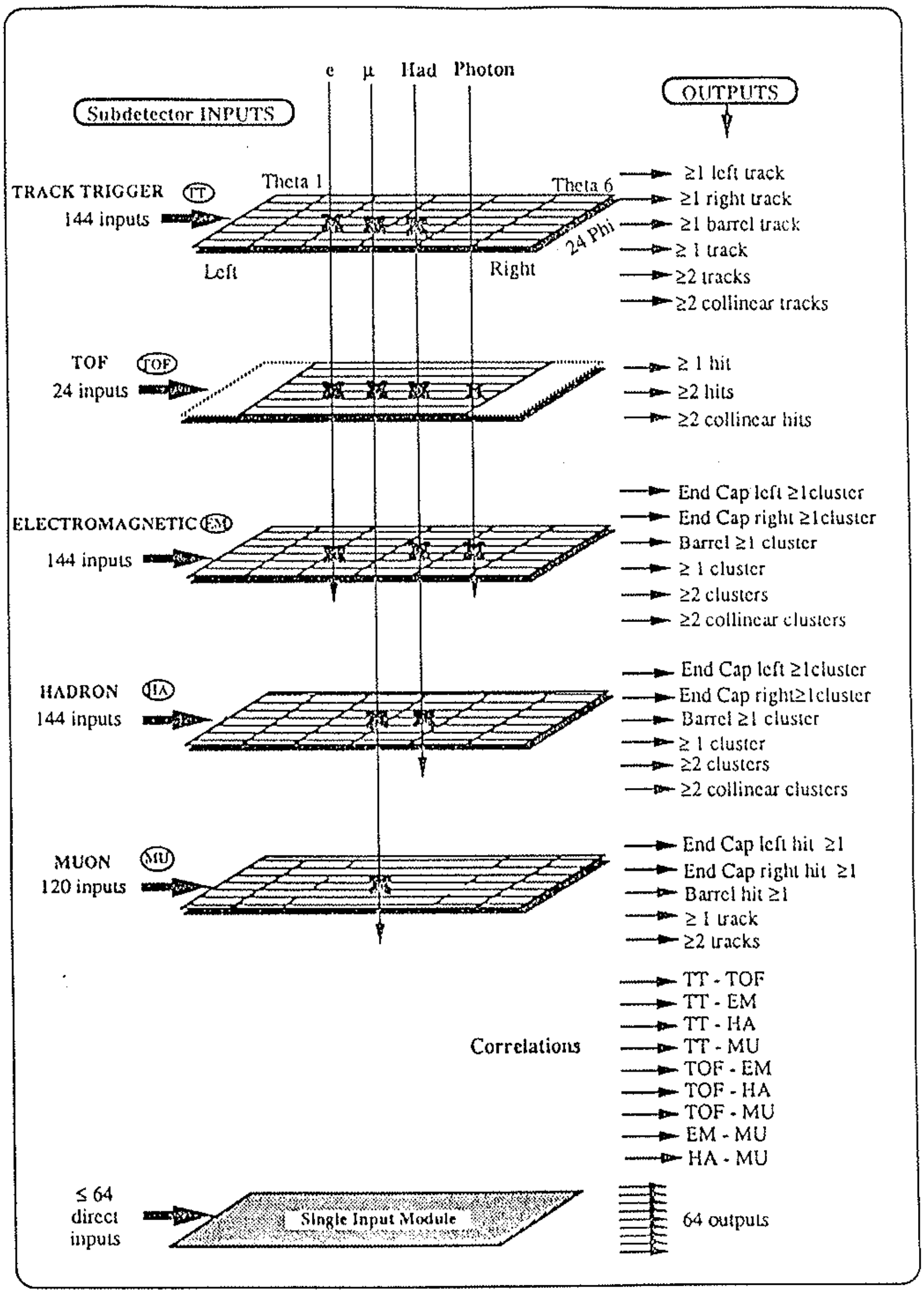

Figure 2.4: Overview of trigger formation by the theta-phi matrix.

most of the OPAL subdetectors.

The OPAL central trigger demands two kinds of input from the subdetectors. Firstly, there are the Single Inputs (SIM) which generally provide a global trigger for the whole of a subdetector, *e.g.* greater than a fixed threshold of energy seen in the whole of the electromagnetic barrel region. These are often quite simple but have high thresholds to reduce background. Some are used as a 'stand-alone' trigger, *i.e.* they are sufficient on their own to justify full readout of OPAL. These can provide a high efficiency by themselves for certain events despite the high threshold. Secondly, there are the theta-phi inputs to the theta-phi matrix (TPM) of the central trigger. These consist of lower threshold inputs which are more restricted in location by segmenting the angular range into 6 θ and 24 ϕ bins. Although often the rates of these are too high to be considered as a direct input to the trigger, they can be used in coincidence with signals from other sub-detectors. The scheme is illustrated in figure 2.4.

The theta-phi matrix provides several outputs corresponding to certain correlations between detectors. These are used along with the Single Input signals in a final software programmable logic unit where the various individual signals are combined in a quite flexible way to form the overall trigger decision.

The power of the final trigger signal formation is due to the number of layers of detectors contributing to the trigger. The central detector provides a signal on charged tracks, the time of flight indicates charged particles passing in a precise time interval consistent with particles originating from an e^+e^- annihilation, the calorimeters signal showers of various types and the muon chambers provide redundancy on muons which otherwise have less redundancy of detection, especially in regions of poor coverage by other detectors. There are many different ways in which an event of any type can cause the trigger to be set both by single input signals from one detector and by angular correlations between detectors. This ensures high and easily measured efficiencies while maintaining low backgrounds.

2.3.10 Data Flow in OPAL

During normal data taking at OPAL, all the information coming from each sub-detector is formed by a chain of electronics and processors controlled by a single processor (the FIC, built around the Motorola 68020 or 68030 processor) in a VME crate called the Local System Crate (LSC). When a trigger is sent to digitise an event, the hardware is read out and an event number sent from the central trigger logic is attached to the data. The raw signals are processed in order to, for example, reduce data size and convert the information into a standard format.

This processing is generally performed by parallel tasks running in the same, or parallel processors, and each stage of the processing is well buffered to ensure that the dead-time of the sub-detector is due purely to readout time, and not due to processing bottlenecks.

When each detector has the final formatted data ready, it is transferred across to another VME crate called the Event Builder (EVB), and this event builder combines the data into one raw data structure for the whole event, checking that the data from each sub-detector has the same event number. From over 150,000 original analogue signals, the data from the most active type of event, the multi-hadron, is generally reduced to less than 100 kbyte of data. This is before a data compression package run by the next processor, the Filter.

Other than this data compression, the Filter (FI) also monitors all the events so that information about the data is immediately available online, and at the same time rejects the more obviously useless events. It uses simple algorithms which can be easily run in real-time in order both to flag interesting events, try to classify them and also to identify which events need not be considered further — as such it forms a sort of second level trigger. This helps to reduce both the workload at later stages of data processing and also the storage requirements. From here the full event is written to tape or some other permanent recording medium.

The final stage of processing is the OPAL reconstruction package called `ROPE`. In 1991 for the first time this was actually run online in real time, although it is not critical to do so since the raw data is permanently recorded anyway. Also generally the reconstruction has to be run again at a later stage when better calibrations are known. It is this reconstruction that uses the raw data to extract information about particles seen in an event. The results are summarised and stored onto various recording media (*e.g.* tape, optical disk) for easy access in later analysis.

Chapter 3

The Muon Endcap Detector

The Muon Detector for OPAL is designed to surround the rest of the detector elements over as large a solid angle as possible with typically four layers of active regions, capable of detecting any charged track passing out of the detector. Muons that emerge at angles greater than $|\cos\theta| = 0.7$ are detected by the muon endcap, which consists of two large walls, approximately 12 m by 12 m of chambers, covering each end of OPAL. The design of these streamer chambers is based on a popular design used in many experiments (see [18]), although many components had to be altered for the specific needs of OPAL. Details of their construction can be found elsewhere [19]. This chapter briefly describes the detector hardware and electronics and discusses its performance in data taking at LEP.

3.1 Muon Endcap Detector Hardware

3.1.1 Detector Geometry

For ease of construction, the chambers are subdivided at each end into six rectangular units as shown in Figure 3.1, the four larger regions being named Quadrants, and the two smaller ones Patches. These overlap slightly to give continuous coverage. This construction provides a good acceptance in the endcap region while leaving gaps in the necessary places for the beampipe, cables and magnet power supplies to reach the detector.

The Quadrants and Patches all contain four layers of streamer chambers, each

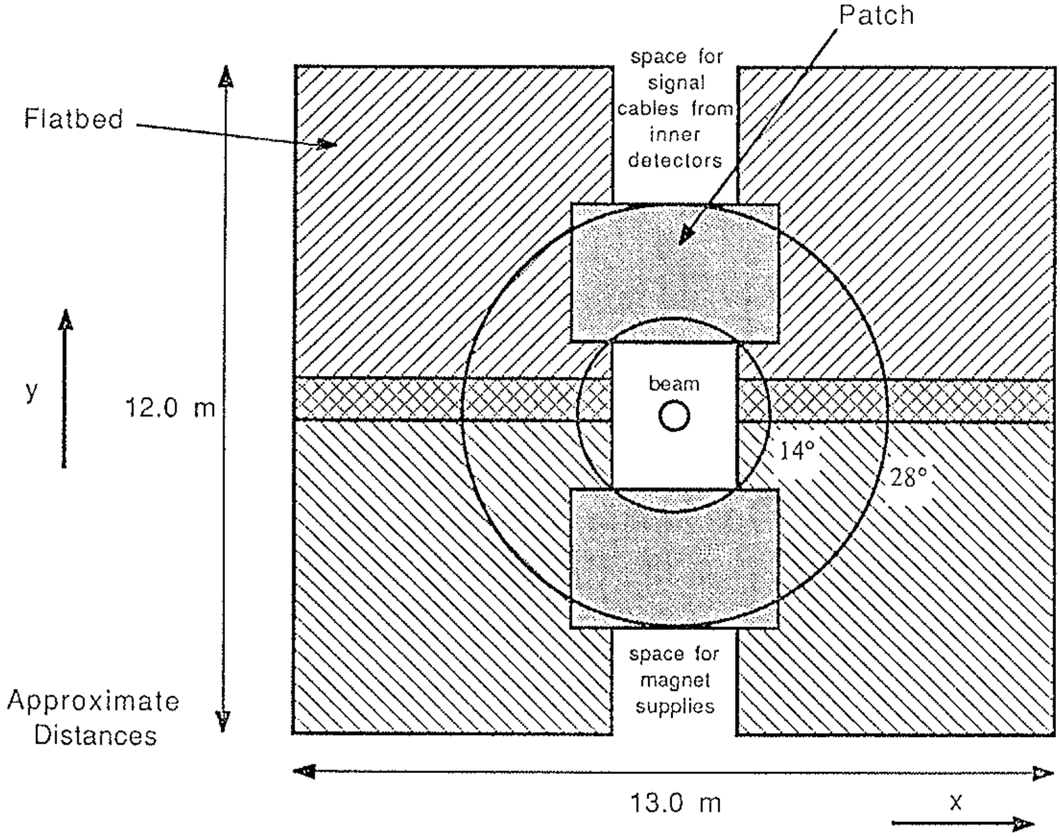

Figure 3.1: End on view of the OPAL Muon Endcap.

of which measures a pair of co-ordinates within the plane of the chambers. These co-ordinates correspond approximately to the OPAL x and y definitions. Therefore the position of any particle passing through an active region of the chambers is determined at up to four separate points, or more where two regions overlap. The spacing of the chambers in the z coordinate is such that there are two double planes of chambers separated by about 65 cm (see Figure 3.2). This separation gives a reasonable lever arm for extrapolation of the tracks back towards the inner detectors and the collision point.

3.1.2 Streamer Chamber Construction

The active part of the detector consists of anode wires held at high voltage surrounded by a suitable gas mixture. Each wire is supported under tension in the centre of one of the 'open' squares which make up the extruded plastic comb shaped profile shown in Figure 3.3. The whole detector is made from a plastic called Noryl — a novel plastic for this sort of construction, used because of the greater fire hazards of the more commonly used PVC (which produces dangerous

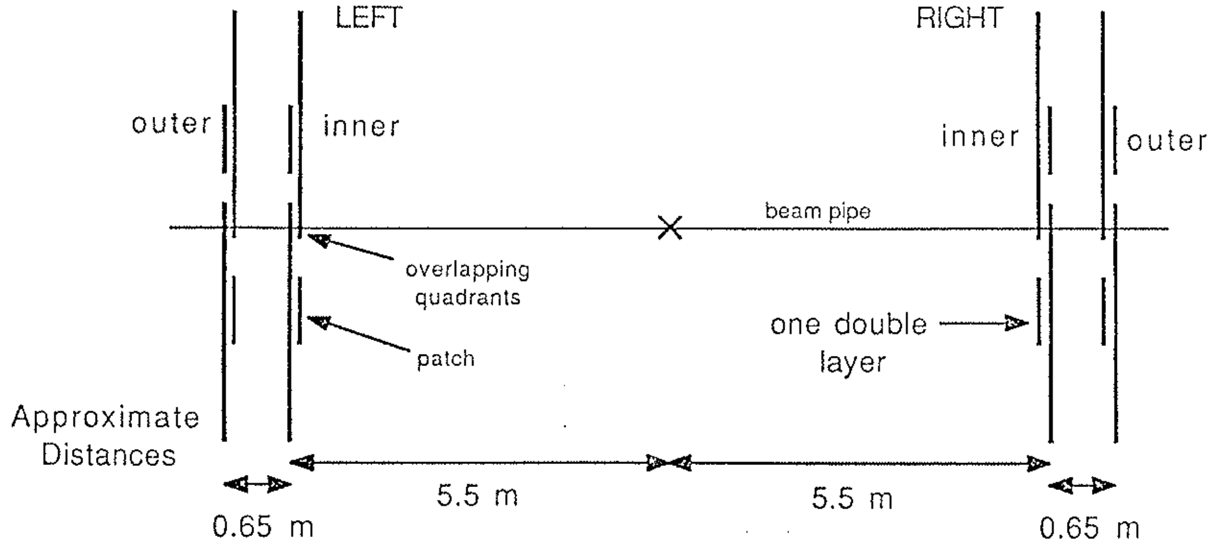

Figure 3.2: Schematic side view of detector layout.

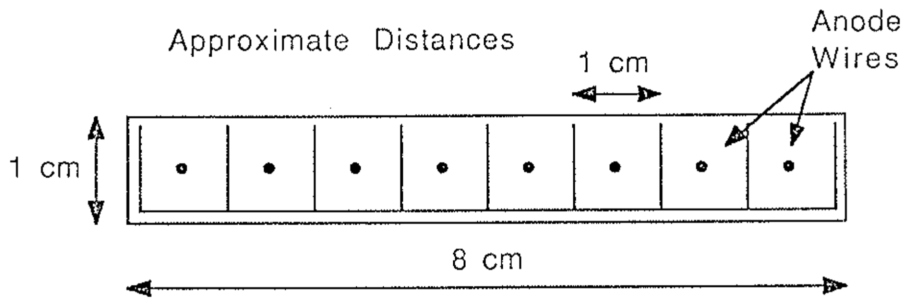

Figure 3.3: Cross section of unit profile.

fumes).

The inside of the profile is painted with a graphite emulsion giving a resistive coating to act as a cathode. The profiles are surrounded by a gas jacket in which a mixture of 75% isobutane and 25% argon is circulated. The profile and gas jacket together form a unit, which is about 8 cm by 1 cm in cross section and stretches from one edge of a quadrant or patch to the other, making a length ranging between about 2.5 m to 6.5 m.

The detector consists of 2656 of these units mounted on long plastic boards. Most of the boards are approximately 64 cm wide and so support eight units laid side by side. The board and eight units are collectively known as a module. These boards are prepared beforehand with conducting strips for readout purposes as described later. Up to nine of these modules are laid out on a flat steel support structure (referred to as a flatbed) to make up one layer of a quadrant or patch.

Another layer of chambers, with wires running orthogonally to the first, is mounted on top of the first, sandwiching two readout planes. The readout planes are described in more detail in Section 3.2. This whole arrangement then constitutes one double layer of active chambers, and is shown schematically in figure 3.4.

3.1.3 Operation of the Streamer Chambers

The streamer chambers are operated in the so-called limited streamer mode. This method of operation has undergone many investigations and the response of the chambers has been carefully monitored, although the actual physical processes involved are still subject to debate. Similar chambers are used extensively within OPAL and on other LEP experiments. The reason for using this mode is that for any charged particle crossing the active area, a very large avalanche of ionisation occurs near the anode wire and this signal is easy to detect. Although it contains no information for particle identification, since the streamer size is not proportional to the original ionisation, the positional information is very accurate.

A streamer forms in the chambers [20] after ionisation is initiated by a charged particle passing through the gas mixture. The ions drift towards the anode, where the electric field is very high, and they then accelerate and undergo collisions with the gas in the tubes. This produces secondary ionisation and leads to a large 'gas amplification' of the charge producing an avalanche of charge — this is the streamer. The development of this streamer is critically dependent on the gas composition. The amplification requires there to be a vehicular gas (Argon in this case) to multiply the initial ionisation. The gas mixture also must contain a quencher gas (the Isobutane) which absorbs some of the photons produced in the avalanche. This then limits the extent of the ionisation along the wire. The streamer is also limited in spread towards the cathode so that no spark breakdown occurs which would be the case in spark chambers.

The muon endcap detector is successfully run at 4.3 kV in the OPAL pit, which is lower than in tests at the Rutherford Appleton Laboratory (4.5 kV), but this is thought to be reasonable due to the lower air pressure at the pit which is 100 m underground. As has been confirmed by the usefulness of the data found in the

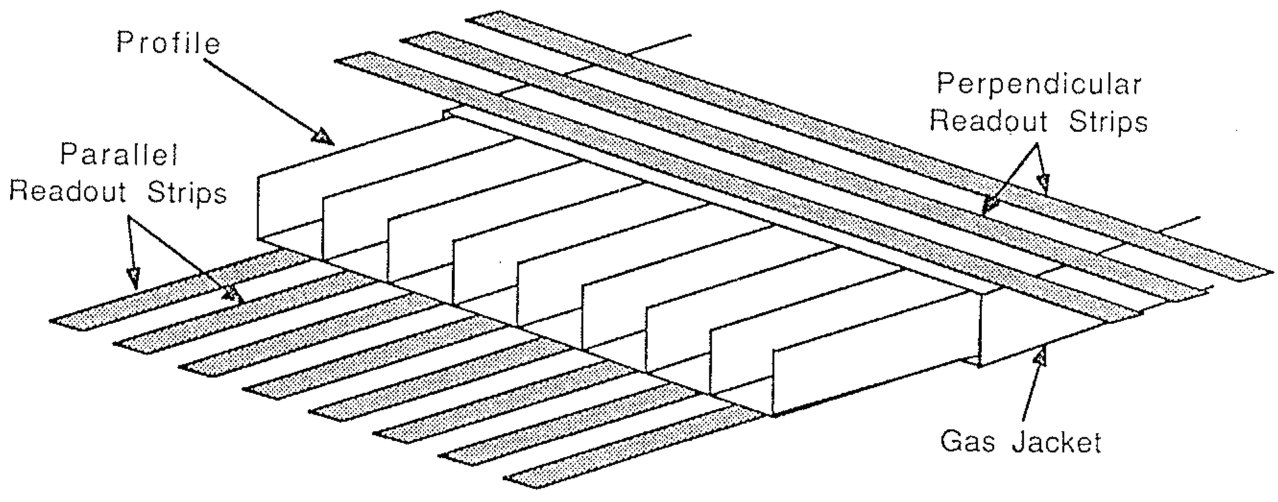

Figure 3.4: View showing position of readout strips.

muon endcap, the chambers are performing well, giving clear and large signals at a high efficiency. It is also important to note that after two years of operation, there is no sign of the chambers beginning to break down - in fact they appear to have become more stable with time, drawing very little current (~10 nA per module). Only about 1% of the chambers are disabled due to known problems such as gas leaks, high voltage breakdown or faulty electronics.

3.2 Muon Endcap Detector Electronics

3.2.1 Readout Strips

Each plane of chambers is sandwiched between two planes of plastic instrumented with readout strips. On the inside face of the plastic, nearer the active region, are laid ~8 mm wide strips of aluminium tape. The outer face of the plastic is covered with a single earthed conducting plane of foil which insulates the system from external charges. On the underside of the unit profile the strips run parallel to the sense wires, with one strip per wire. On the open side the strips run perpendicular, as shown in Figure 3.4.

When a streamer occurs, it induces charge on the readout strips both above and below, and each charge will be propagated along the conductor where it can be read off at one end. This end is called the readout edge. The position of a signal can then be determined by looking for a peak in the charges induced on adjacent strips and taking a weighted mean of the nearby signals. The location of this signal along the two readout edges gives the two coordinates of the streamer position in the plane. Knowledge of the absolute chamber position in the OPAL coordinate system (found from survey measurements) gives the exact position of the particle.

The resolution achievable with this system was found from tests to be about 1 mm for perpendicular strips, and 3 mm for parallel [19]. This is approximately equal to or, in some cases, better than the best information on the absolute position of each flatbed so is not in general the limiting factor for accuracy.

3.2.2 Front End Electronics

The amplification of charge in the streamers is large enough that the electronics needed to detect the signals can be fairly simple and cheap. This is fortunate because of the large number of channels — over 40,000 in the whole of the detector. In order to simplify the cabling and cope with many channels a highly multiplexed system was required [21].

At the most basic level, the readout consists of front-end electronics cards. These are plugged on to 32 adjacent readout strips. Each card contains four integrating hybrids [22] which store the induced charge on each of eight strips. The charge is integrated over a period of 5 μs and stored in capacitors on the readout card. Each of these capacitors can be discharged in turn into the one signal cable of the card. Thus 32 strips are read out via one cable. The charges are discharged into ADCs, each of which can digitise the signal from up to 9 front-end cards. The ADCs are mounted in the detector frame itself, next to the front-end electronics to reduce cabling.

Eight ADCs are contained in an electronics crate known as a Branch Controller Crate (BCC), which is therefore capable of digitising 2304 strips, usually all 4 layers of readout along one edge of a Quadrant. This crate takes care of the scheduling of the readout and the multiplexing.

The ADC has a 12 bit range and before starting to take data the behaviour of each channel is investigated by feeding in a test charge to the system. This is done to set the so called hardware pedestals. These are offsets to put the ADC digitising range in the right region for each strip, as the exact behaviour of each strip and the connected electronics can vary considerably. The hardware pedestals are stored in the BCC and are used during digitisation. When the pedestals are set, the resulting ADC value should be fairly constant at a value of about 200 for no signal. This value is called the software pedestal and is monitored during data taking. When looking for signals in data processing, and when the data is packed, the software pedestal is regarded as a zero offset and is subtracted.

3.2.3 Raw Trigger Signal Formation

The BCC crate also forms the basic trigger signals for the muon endcap. These basic trigger signals are formed from the summed charges stored in front-end capacitors similar to those storing the signals for each strip. However, in this case a whole card is discharged to form the signal for the trigger. In fact the whole card signal is further summed for 2 to 4 adjacent cards and the level of activity compared to a preset threshold. A single logical flag is set for each region above threshold and these are further processed as described later. If the event is subsequently read out, these logical flags is also recorded with the data, which is useful for tests on the trigger.

The threshold used for most of LEP running so far corresponds to a summed charge over a trigger region of about 1.7 pC. The threshold behaviour can be seen from plotting the summed ADC counts for channels that triggered and channels that failed to trigger as shown in Figure 3.5. The signals reconstructed in this way will correspond closely, but not exactly, with that seen by the trigger electronics. The histograms indicate a good efficiency for charges above about 300 counts, corresponding to about 2 pC[1]. As will be seen below, streamers generally produce an integrated charge far larger than this. However, the size of the charge does spread right down to zero, so a finite number will always be lost.

The histogram of counts for channels that do not trigger shows a standard deviation due to noise of about 50 counts. It in fact varies between channels

[1]An approximate conversion from ADC counts to charge is that the full ADC range, 4000 counts, is about 30 pC.

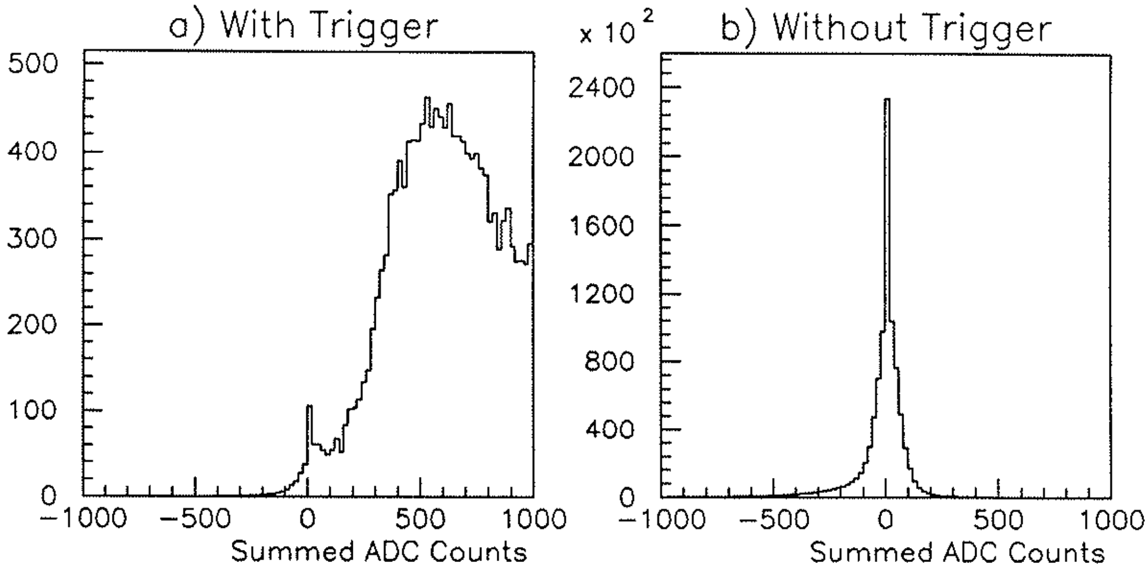

Figure 3.5: Summed ADC counts for trigger channels in the cases a) they triggered and b) they did not trigger.

since some have more strips and consequently a larger noise level. However, the threshold is still well above this noise.

3.3 Muon Endcap Data Acquisition

The Data Acquisition chain from digitised signals to formatted raw data is a complex multi-level and multi-processor system. The complexity is due in part to the large number of channels read and also the need to have a large safety net of buffering at various stages. An account of the hardware used to perform this is presented in detail in Appendix A; only the processing of the data is described here.

Information comes from the digitisers as 12-bit words which generally take their pedestal value of around 200. The sequence of the words is mixed up due to the multiplexing, and so firstly the data is re-ordered such that its sequence follows that of the strips along an edge. Once this is done, it is relatively easy to search for active regions by looking for jumps in the pedestal subtracted signals all along each edge. The method used to do this is not a simple threshold triggered algorithm. The reason for this is that often background fluctuations are observed which either raise or lower *all* the observed values by a fixed number. A threshold technique would not be effective in distinguishing real signals from this type of background. Instead, the algorithm processes the values sequentially along each edge looking for a sudden rise between two adjacent strips closely followed by a fall. This is then indicated as an active cluster.

Areas of high activity found in this way are extracted and stored in a new data format. In this the pedestal subtracted signal is attached to a code indicating where on the detector the signal was found. All such active areas are collected in one data structure, and the event number is also included along with internal trigger information. The data is then ready to be sent to the event builder.

3.4 Performance of the Muon Endcap Detector

The muon endcap has operated continuously from the first physics run in 1989, during which it operated well with only fairly minor problems. As for many other sub-detectors, the experience of the 1989 run led to a greater understanding of the behaviour of the detector and the development of monitoring tools to identify faults. Since then the detector has performed very well and run in a stable manner with few, and small, problems. The rest of this chapter describes the main features of the raw data obtained from the muon endcap and the next chapter shows how it has been put to use in various analyses.

3.4.1 Data Quality

From the very first day of running the data acquisition worked very well and the chambers themselves produced very clear streamer signals. It only remained to identify and repair problems. The online hit-finding algorithm managed to identify active regions precisely and also rejected a lot of the background noise. Initially all the information was reduced to a final size of 2 kbyte of packed data, and since then greater confidence in the performance of the system has led to further reductions in the data written to tape. Now the 40,000 or so channels are packed

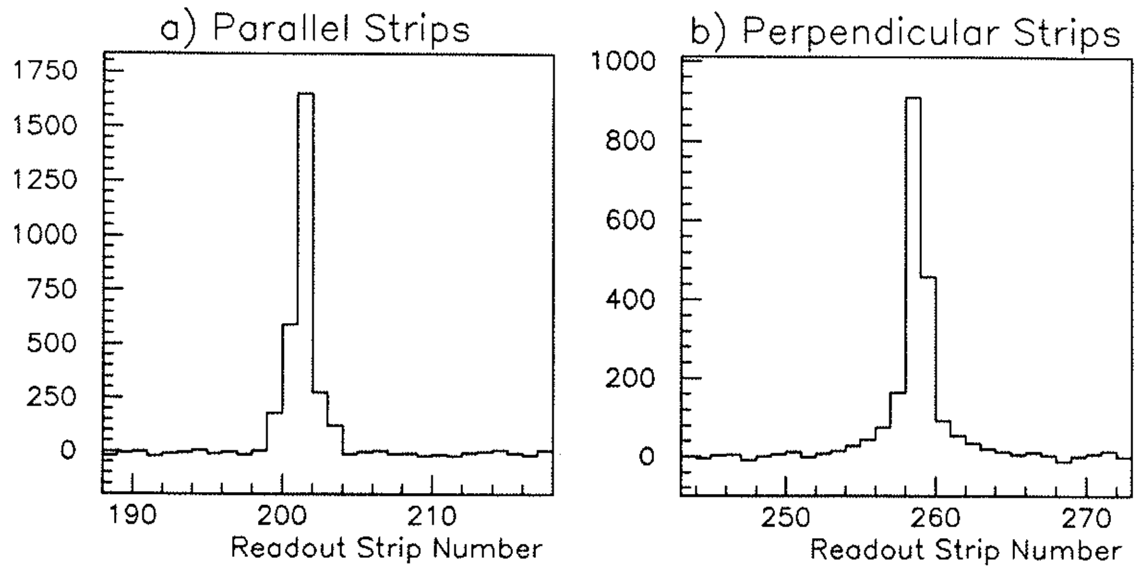

Figure 3.6: One streamer as seen by a) Parallel and b) Perpendicular readout strips.

down to less than 0.3 kbyte on a typical event.

Typical signals for a streamer are seen in Figure 3.6. The cluster seen in the perpendicular strips is a very tight peak with broader tails on either side. The spread of the cluster is used to identify the position of the streamer in this coordinate to about 1 mm accuracy. The parallel cluster is slightly broader with no tail; presumably charge induction loses influence more quickly going through the profile rather than along it. However the resolution is still about 3 mm in this coordinate.

The parallel clusters are generally larger in pulse height than the equivalent cluster seen by the perpendicular strips. This can be illustrated easily by looking at the maximum and integrated ADC charge for the two types, as seen in figure 3.7. The correlation of signal size in the two readout planes of one detector plane can be used to try to reduce problems of 'ghosting' of tracks if more than one streamer occurs in the same plane of chambers. This is only a problem of course within the same Quadrant or Patch where the two streamers occur in one set of X and Y readout strips. Note that the parallel maximum has an artificial peak at about 3800 counts, since this is the top end of the ADC range. The integrated counts

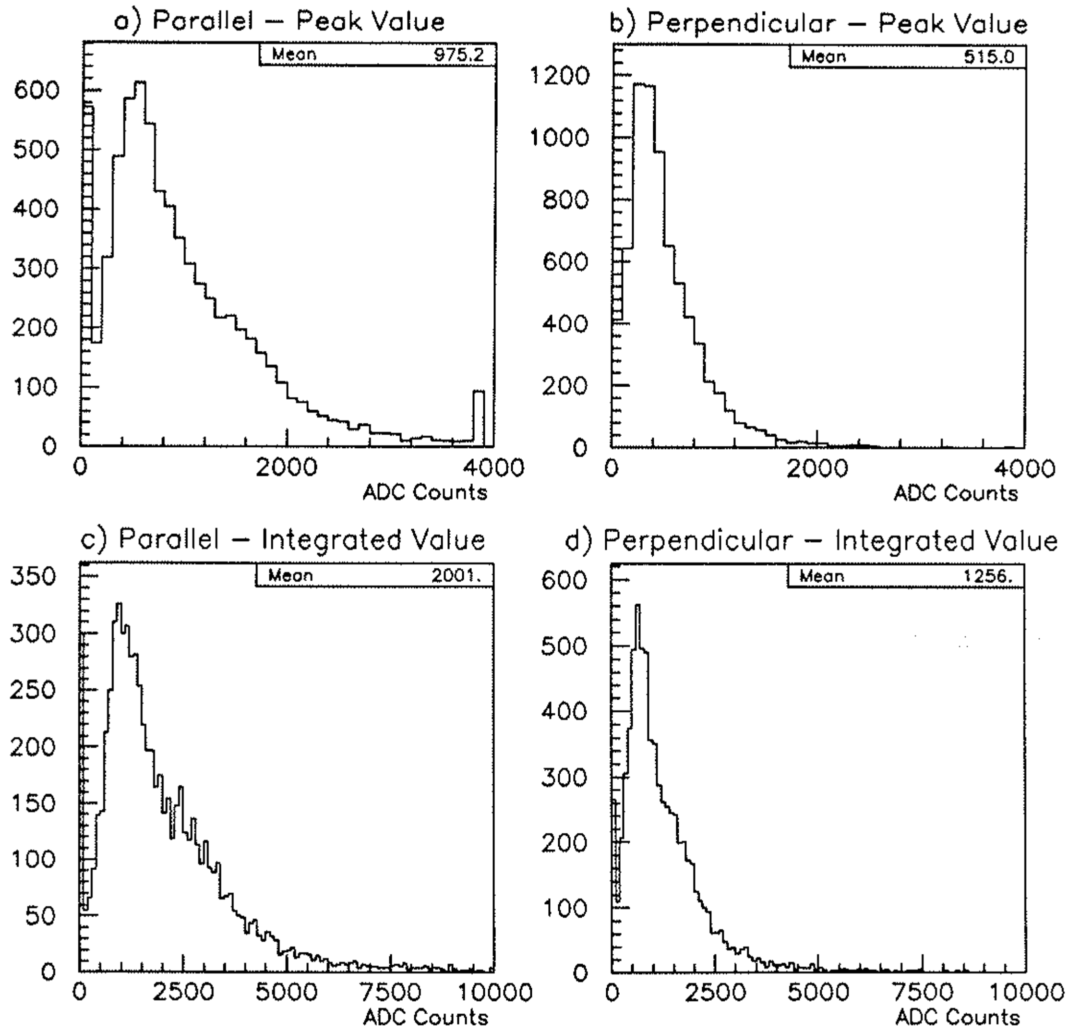

Figure 3.7: Histograms of maximum and integrated ADC counts for streamers observed in raw data both in parallel and perpendicular readout.

are generally well above the trigger threshold of about 300 counts. These points illustrate that the size of the streamers is easily large enough to be useful both for triggering and track reconstruction.

3.4.2 Chamber Efficiency

Although from the first the muon endcap detector was operating fairly successfully, as seen by the very large identified signals, it wasn't until various monitoring packages had been developed that its performance could be assessed quantitatively. In particular one monitoring task was designed to try to check all aspects of the detector as the data was taken. It is described in detail in Appendix B. One of the quantities it attempts to measure is the efficiency of the chambers and the signal readout.

It was found that the dominant inefficiency in the detector is that due to failure of a charged particle passing through the detector to form a streamer — this is assumed from the fact that the readout on neither edge of the chambers found a signal when one was expected. It is concluded that this is mostly due to charged particles passing through the plastic walls or perhaps only crossing a small region of the active detector. This result is confirmed by Monte Carlo simulation of the detector response and by investigations of the development system at the Rutherford Laboratory. From the online calculations described in Appendix B, this inefficiency is found to be at about the level of 5% per streamer tube plane. The subsequent calculations of the efficiency of the data acquisition to locate activity show that almost no significant activity in the chambers escapes detection.

When the full geometry of the detector is considered with two sets of double layers, the possibility of a charged track being missed by all four layers is very small. However, to form a muon track, at least one hit must be observed in both the inner and outer layers, so there is a finite chance of failing to reconstruct a track. This possibility is increased in regions where the detector has faulty units, but since these problems are at a low level, the overall efficiency remains very high (at least 98%).

The final offline efficiency for a signal in each plane is $90.4 \pm 1.3\%$ [23], which is less than the online layer efficiencies suggest. This is partly due to more stringent requirements in the current offline cluster finding algorithm causing a loss of efficiency in the observation of streamers. However, redundancy of layers means that the efficiency for reconstructing tracks is still very high.

3.4.3 Raw Trigger Signal Efficiency

The same efficiency monitoring program as provides the online chamber efficiency is also used to derive an efficiency for the raw trigger signals, as also described in Appendix B. Once the location of a cluster in the readout is found, it is easy to check whether the relevant trigger bit was actually set. In the real data it was found that where a significant signal is seen, about 94% of events have the relevant trigger bit set. Of course, when the geometrical inefficiency for the formation of a trigger is considered (*i.e.* the 5% loss described in the previous section) this implies that for a charged particle passing through a layer of chambers, there is a 89% efficiency for a trigger signal to be set.

Also a good indication of the overall trigger efficiency can be obtained from these measurements. If the average efficiency for one trigger bit is e, then the chance of one track going through four planes satisfying the standard trigger requirement of two out of four hits is approximately given by

$$\text{Single Track Efficiency} = (e^4 + 4e^3(1-e) + 4e^2(1-e)^2)^2.$$

This is approximate since it does not account for the correlation between streamer sizes as seen in the X and Y trigger channels, but the full equation does not predict vastly different results. This formula can be understood when the mechanics of the trigger processing is understood — this is described in the next chapter. With $e = 0.89$, this formula gives an overall single track efficiency for the trigger of more than 95%. As will be seen in the next chapter, this efficiency can also be checked by analysis of the processed data offline, using a clean sample of muon pair events. Analysis of this sort confirms the high efficiency suggested by this calculation.

Chapter 4

The Detection of $e^+e^- \to \mu^+\mu^-$ Events in the Muon Endcap

When investigating low multiplicity Z^0 events in OPAL, such as leptonic final states, it is essential to have a great deal of redundancy in the detection and selection of the decay products. This is to facilitate accurate estimations of efficiencies and backgrounds by the use of independent analysis methods using different parts of the detector to identify the events. In particular, for the reaction $e^+e^- \to \mu^+\mu^-$, the muons must have distinct signals in at least two, preferably three, different sub-detectors which would allow the event to be both triggered and selected for analysis with high efficiency and redundancy. This then allows a very precise measurement of the branching ratio and related quantities to be made in order to perform a detailed comparison with the standard model.

This chapter describes the part the Muon Endcap detector plays in the triggering and selection of events with muons which allow the efficiency of other sub-detectors to be determined. Also, investigations are presented on the performance of the Muon Endcap detector in deriving the track direction for $e^+e^- \to \mu^+\mu^-$ events from the measurement of the position in the endcap.

4.1 Selection of Muons in the Endcap Region

In OPAL all sub-detectors provide data for a given event, but only a limited set provide a trigger and so only these can contribute at all stages of the event selection chain. So for $e^+e^- \to \mu^+\mu^-$ events, with muons produced at high energies, the position of the tracks can be measured by many of the layers right out to the Muon Detectors. However, only the Central Detector (via the Track Trigger), the Time of Flight counters, and the Muon Chambers currently produce useful trigger signals for such events. The electromagnetic calorimeter cannot trigger reliably on muons since they are minimum ionising particles depositing little energy which is comparable or less than the trigger threshold (set at about 1 GeV). Since the Time of Flight detector only covers the barrel region, the contribution of the Muon Endcap becomes essential, both as a trigger for $e^+e^- \to \mu^+\mu^-$, and as a means of identifying events for investigation of the inner detectors' efficiencies.

An independent trigger is provided by the stand alone signal MELR, triggering on two approximately back-to-back tracks in the $|\cos\theta| > 0.6$ region, when inside the Muon Endcap acceptance. Raw data is then passed to the Filter, which rejects triggers which show little evidence of being true Z^0 decays. Only the more obviously useless events can be dismissed here, of which cosmic rays triggering MELR form a large part. Events are then reconstructed and candidate 'physics events' are selected and it is only these events that are generally considered in most analyses. This physics selection has more information available than the filter and can therefore more accurately select, for example, muons coming from the interaction point over stray muons from cosmic rays. It is important that both of these stages have a good efficiency in order to retain all Z^0 physics data for further analysis, but also, for the purpose of reduction of data size, they should manage to reject a large amount of the cosmic ray background.

4.1.1 The Muon Endcap Trigger for Muon Pairs

The formation of raw trigger signals has been described earlier (Section 3.2.3). This section shows how the trigger integrates with the rest of OPAL and provides an independent set of $e^+e^- \to \mu^+\mu^-$ events.

	OPAL definition	Muon Endcap definition
θ_1	$-0.98 < \cos\theta < -0.60$	$-0.98 < \cos\theta < -0.82$
θ_2	$-0.82 < \cos\theta < -0.21$	$-0.82 < \cos\theta < -0.21$
θ_3	$-0.60 < \cos\theta < +0.21$	not covered
θ_4	$-0.21 < \cos\theta < +0.60$	not covered
θ_5	$+0.21 < \cos\theta < +0.82$	$+0.21 < \cos\theta < +0.82$
θ_6	$+0.60 < \cos\theta < +0.98$	$+0.82 < \cos\theta < +0.98$

Table 4.1: Comparison of OPAL θ bins with Muon Endcap.

	OPAL definition	Muon Endcap definition
Number of Bins	24	24
Size of Overlapped Bins	30°	15°
Numbering Direction	1-24 as ϕ 0°-360°	1-24 as ϕ 0°-360°
Centre of Bin ϕ_1	0°	7.5°

Table 4.2: Comparison of OPAL ϕ bins with Muon Endcap.

OPAL Trigger Requirements

As described in section 2.3.9, sub-detectors have to provide two types of trigger signal, the stand alone (SIM) and θ-ϕ (TPM) inputs. The Muon Endcap provides 96 θ-ϕ signals — 24 ϕ signals by 4 θ, and also three SIM signals, namely:

- **MEL** — Muon Endcap Left
- **MER** — Muon Endcap Right
- **MELR** — Muon Endcap Left and Right

The definitions of the θ-ϕ bins for the Muon Endcap signals are actually slightly different from the standard OPAL ones, which are associated directly with the Track Trigger definitions. The theta bins are summarised in Table 4.1. Note that the endcaps in fact cover only the region $0.986 < |\cos\theta| < 0.60$. The decision not to overlap bins was made partly to retain the intrinsic resolution, and partly since the conversion of the raw cartesian type trigger signals to polar form requires some overlapping anyway. The ϕ segmentation is defined in Table 4.2. The differences in OPAL and muon endcap definitions are not a problem in associating θ-ϕ bins as the overlapping in the signal formation implies that at least one of the bins will correlate with other layers of the θ-ϕ matrix.

Bins in left endcap fired		Bins in right endcap required	
θ bin	ϕ bins	θ bin	ϕ bins
1	1-6,19-24	6	7-18
1	7-18	6	1-6,19-24
2	1-6,19-24	5	7-18
2	7-18	5	1-6,19-24

Table 4.3: Definition of 'collinear' form of MELR.

The three SIM inputs require little explanation beyond their names. The MEL and MER signals are purely an **OR** of all the θ-ϕ signals in the left and right endcaps[1] . MELR was originally intended to be simply a logical **AND** of these two signals, thus forming a stand-alone trigger for events such as $e^+e^- \rightarrow \mu^+\mu^-$ with the muons going into the forward region. However it was found, when the trigger was working efficiently, that this still picked up a high background from cosmic ray muons. Since there were few redundant OPAL triggers in the same region, it was impossible to require coincidence with another trigger without the danger of losing good physics events. Instead MELR was modified so it can be switched easily between two possible settings; the original simple definition and one that requires some degree of collinearity, as shown in Table 4.3. This is sometimes referred to as Muon Endcap left right collinear, although the hits are often only very loosely collinear.

Formation of Raw Trigger Signals

Each readout edge of the chambers in both X and Y directions is divided into six areas called trigger channels. These are areas formed by a cluster of 64, 96 or 128 readout strips, and so, for a quadrant, a triggering region will be about 6 m long by around 1 m wide. These regions form the coarse segmentation used for trigger signals. The number of strips is limited to being a multiple of 32, the number of strips in one card, the fundamental unit of readout electronics. The width of a triggering region is generally chosen to be smaller near the beampipe to give better resolution in the low θ region where the θ-ϕ bins are more crowded. A typical quadrant segmentation for an outer plane with the θ-ϕ bins overlaid is

[1]Left is defined as $-z$ in OPAL coordinates, and so includes all the θ_1 and θ_2 signals. Right therefore has the θ_5 and θ_6 signals.

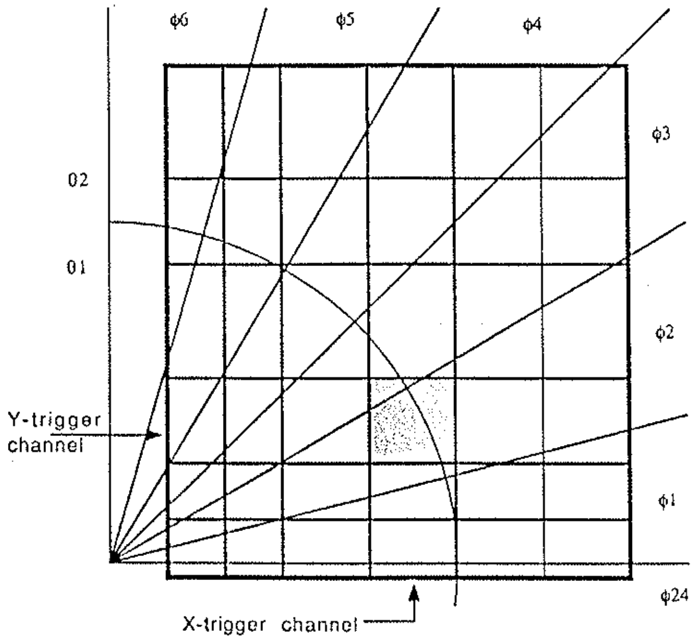

Figure 4.1: One quadrant showing trigger channels with θ-ϕ bins overlaid.

shown in Figure 4.1. A single bit is set if the signal integrated over all the readout strips of the trigger region exceeds the threshold value. The raw trigger signals consist of a set of such bits corresponding to each of the trigger regions. The choice of strips included in each trigger channel, which is different for inner and outer planes, and the way in which the signals are combined together in coincidence provide scope for sophisticated assessment of each event.

Pointing requirement

Firstly, to help reduce backgrounds from cosmic rays passing through the detector, there is a limited requirement for tracks to point to the vertex position. This is done in both the X and Y projections using the 65 cm lever arm between the inner and outer chambers of the Muon Endcap detector. Remembering that there are two inner and two outer planes of streamer chambers, it can be demanded, for example, that there be activity in at least one of the inner planes, and at least one of the outer. In fact the exact requirements can be adjusted quite flexibly, demanding more activity if there are large backgrounds, but the example given above is always used as a basic minimum. Coincidences between trigger regions in the inner and outer layers are set up to select tracks from the vertex — this corresponds to the signal being in the same trigger channel in each layer.

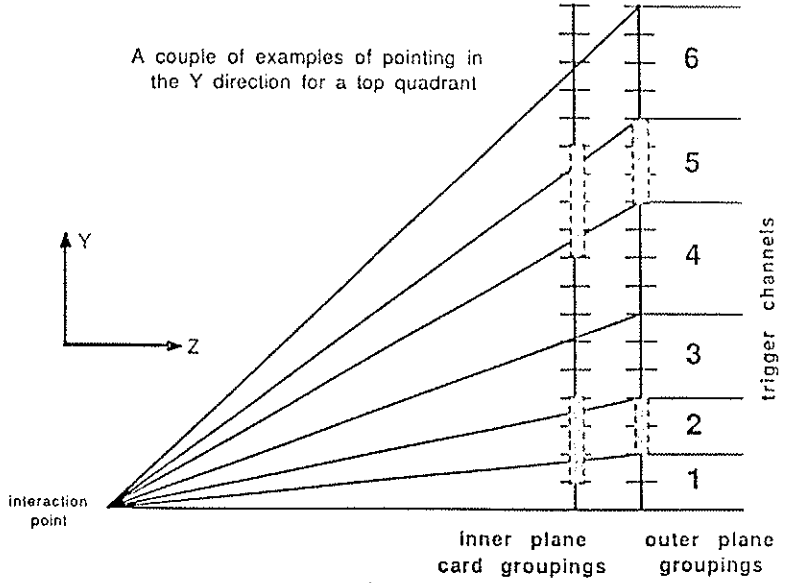

Figure 4.2: Example of card groupings in one readout edge.

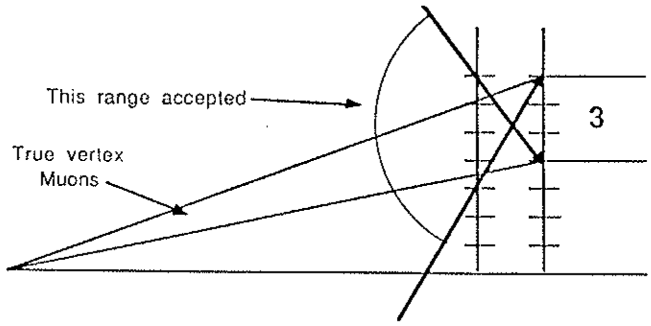

Figure 4.3: The power of rejection in one coordinate.

This implies a slight complication in the choice of strips to be included in each trigger channel, since particles originating at the interaction point will be travelling at an angle to the plane of the chambers. So a different grouping of strips is needed in the inner and outer readout planes. The outer plane can be considered as the reference plane, and the groupings here, as shown in Figure 4.1, contain no strips in common. The inner plane channel groupings are then defined by including in them any readout card which can possibly contain the signal of a particle travelling from the interaction point to the corresponding channel in the outer plane grouping. An illustration of the choice of channels to ensure pointing towards the vertex is shown in Figure 4.2. This method can reject some of cosmic ray muons as shown in Figure 4.3 and when the combined effect of rejection in both X and Y trigger signals is considered, the background is reduced by a factor of around six.

It is important to note that at this level of pointing, multiple coulomb scattering is negligible, especially for high energy muons as produced in the reaction

$e^+e^- \rightarrow \mu^+\mu^-$. A typical deflection for a 45 GeV muon would be about 2 mm at the plane of the muon endcap, which is less than the readout strip spacing. This displacement is also negligible for the more precise projection of the tracks to the vertex described later in the chapter, although in this case for lower energy muons produced in quark decays the scattering does become significant, *e.g.* about 2 cm for a 5 GeV muon.

Grading of Coincidences

The raw signals are processed to use the coincidence between the various layers of streamer chambers in such a way that a potential track in a combination of trigger channels is graded into one of four categories — no hit, weak, medium or strong. The four signals corresponding to one channel in the four planes are assigned a value according to the definitions described in Table 4.4.

Grading	Bit Pattern		Description
	Second	First	
Strong	1	1	All 4 planes triggered
Medium	1	0	3 out of 4 planes triggered
Weak	0	1	2 out of 4 planes triggered (one outer, one inner)
No Hit	0	0	Any other combination

Table 4.4: Grading of coincidence hits in one trigger channel.

For example, if a muon passes through all four layers of the muon endcap in a line pointing to the vertex, but one of the signals produced was too low to exceed the trigger threshold, the three trigger signals seen will imply a medium grade coincidence. However, a cosmic ray muon may produce four good signals, two near each other in the outer layers, and two in the inner. There will be two associated signals in the same channel for inner planes, and similar for the outer planes. However, since the cosmic ray may be travelling at a large angle to the expected trajectory of Z^0 decay particles, the outer plane signals are likely be observed in different trigger regions, and consequently the trigger logic will not associate them with in signals in the inner planes. The grading system will give no trigger from the associated two hits in one channel as two individual signals only form a trigger if they occur one in the inner and one in the outer layer. The cosmic ray muon is rejected as hoped.

Suppose the information is known about which of the X and Y regions have significant activity. To produce the θ-ϕ information, the intersection of the active channels must be identified and the θ-ϕ bins corresponding to that region will be signalled as active. To add more flexibility to the system the necessary combination of channels can be adjusted according to the following *minimum* requirements:

1. Weak hit in both X and Y projections.
2. Weak hit in one projection, medium in the other.
3. Weak hit in one projection, strong in the other.
4. Medium hit in both projection.
5. Medium hit in one projection, strong in the other.
6. Strong hit in both projection.

In practice, only the 'weak' grading has been used. It reduced background sufficiently to give an acceptable trigger rate while providing an efficient trigger. However, if a different strategy were needed, the threshold and grading logic are easily changed in software and the trigger regions themselves can be redefined by replacement of several simple connectors at the front end.

The SIM signals are finally formed from the θ-ϕ signals as described above. An indication of the background (mostly from cosmic rays) can be seen from the rates of these SIM triggers. The individual left or right triggers fire at a rate of about 30 Hz in a typical run, and the collinear coincidence MELR is about 0.2 Hz, which are obviously far higher than the physics rate (typically less than 0.1 Hz for Z^0 formation and decay). Many of the events triggered by MELR have no other triggers set and this shows the need to reject a lot of the MELR events at the filter and later stages.

OPAL trigger for $e^+e^- \to \mu^+\mu^-$

In the barrel region, with three redundant trigger systems (Time of Flight, Track Trigger and Muon Barrel) which allow for many combinations and correlations of triggers to trigger OPAL overall, then the triggering efficiency is almost 100%. However in the endcap region the combinations are reduced as the Time of Flight only surrounds the barrel. Since it is still important to analyse $e^+e^- \to \mu^+\mu^-$ to as large $|\cos\theta|$ as possible, it is crucial to understand the trigger efficiency in this region. Only the Muon Endcap and the Track Trigger are useful for muons at $|\cos\theta| > 0.8$, and although the Muon Endcap efficiency should be almost constant within its acceptance, this is not necessarily true for the Track Trigger.

For a typical back-to-back muon pair in the high $|\cos\theta|$ region there are four main ways for the event to be triggered:

1. The SIM input MELR as described above — this is the only way which is independent of the track trigger.

2. A pair of collinear tracks in the central detector — this is independent of the muon endcap.

3. A θ-ϕ correlated track in the track trigger and muon endcap — this triggers on just one muon obviously providing even more redundancy.

4. A trigger in the muon endcap with a track trigger signal at the *opposite* end.

To estimate the efficiency, data, triggered on each detector independently, are required. When the efficiencies of each are known, then the overall efficiency can be found.

Estimating Efficiencies for the Trigger

Using the standard OPAL muon-pair selection for data collected in 1990 (as described in [24]) which extends to $|\cos\theta| = 0.95$, and selecting events which were triggered and selected independently of the detector under investigation, an unbiased estimate of the efficiencies at all values of θ can be found. So for example, using events triggered off the Track Trigger collinear tracks, and selected by track

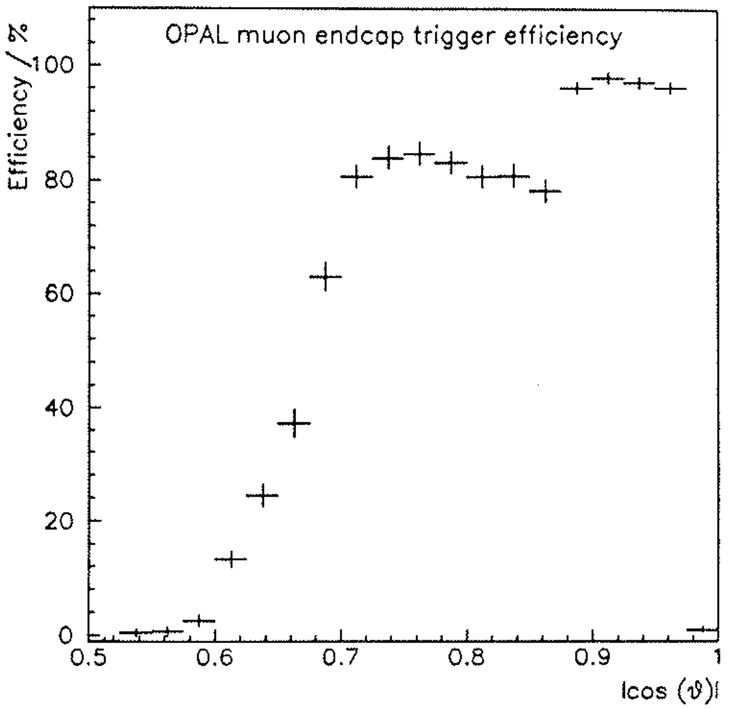

Figure 4.4: Muon Endcap efficiency for single muon.

quality, the fraction of events triggered by the Muon Detector can be found and vice versa for the Track Trigger. Because of the geometry of the Muon Endcap, its efficiency is strongly dependent on ϕ as well as θ. Fortunately the same is not true of the Track Trigger, so only variations in efficiency with θ need be considered when calculating the combined efficiency with both detectors.

The efficiency of the Muon Endcap to form a trigger on one muon as a function of $|\cos\theta|$ is shown in figure 4.4. The overall shape of the efficiency is due to the vertical gap between the larger chambers. The patch chambers in the region $0.88 < |\cos\theta| < 0.97$ fill this gap, giving complete coverage where the efficiency is determined by the intrinsic efficiency of the chambers. It is equivalent to the efficiency averaged over the geometrical acceptance of the endcap which is measured to be $97.1 \pm 0.3\%$. This agrees well with the internal measurements described in the previous chapter. So for a back-to-back muon pair, with both muons in the acceptance, the efficiency for the MELR trigger is about 94%.

More importantly, when combined with the Track Trigger efficiency in this region (as shown in figure 4.5(a)), and with the contributions from other detectors,

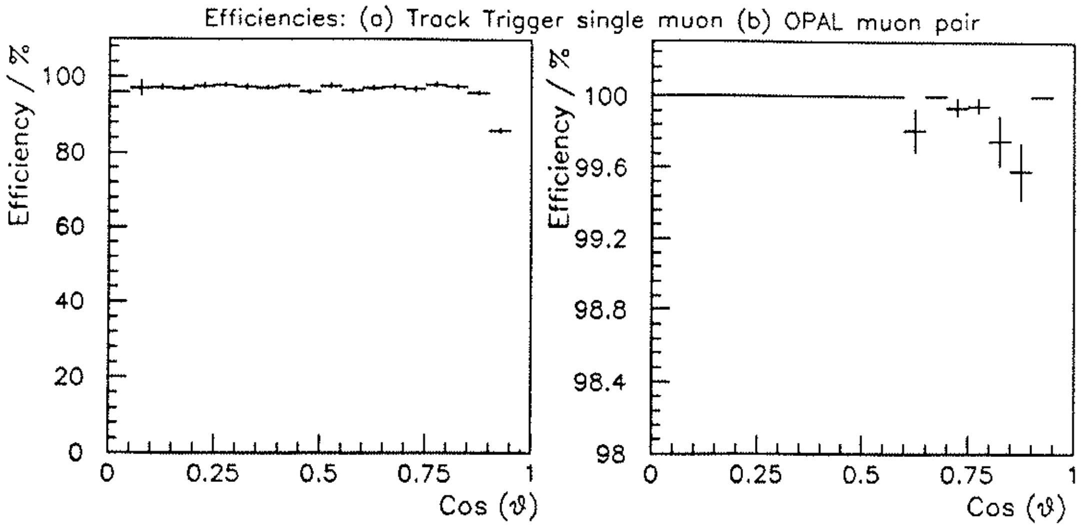

Figure 4.5: Efficiencies for a) Track Trigger for a single muon track to be observed and b) the firing of the combined OPAL trigger for muon pairs as a function of $|\cos\theta|$.

the overall efficiency for $e^+e^- \to \mu^+\mu^-$ as a function of angle comes out as shown in figure 4.5(b). Note the scale on this figure. The small dips in the efficiency correspond to the poorer regions of OPAL coverage when all sub-detectors are included. The trigger efficiency is finally quoted (conservatively) as $99.9 \pm 0.1\%$ for all events. Thus the trigger forms a negligible contribution to the systematic error in measuring the cross section of the $e^+e^- \to \mu^+\mu^-$ reaction, and nearly all the useful acceptance is utilised with the current angular cutoff of $|\cos\theta| = 0.95$.

4.1.2 The Filter Algorithm for Endcap Muons

The OPAL Filter takes raw data from the detector in real time and has to make a decision as to the usefulness of the data in each event triggered. It then decides on this evidence whether the event should be recorded to permanent storage for subsequent reconstruction and analysis. In 1991 its purpose was also to make the data more compact for storage. The overall point is to make the data more manageable by decreasing the amount recorded but with the important proviso that useful data should not be lost since it is irretrievable after being rejected by the Filter.

The relevance for the Muon Endcap is that a high percentage of events triggered by the stand-alone signal MELR are not the result of genuine e^+e^- interactions, and so would provide an additional burden on computer storage and processing if not rejected at an early stage. So the motivation of a filter algorithm to choose good MELR events is that it should lose a minimal quantity of muon pair events but be good enough to distinguish them from muons of cosmic ray origin. The routine in fact should identify muons from any Z^0 decay, but in most cases other than $e^+e^- \rightarrow \mu^+\mu^-$, there are plenty of other distinguishing features that the Filter should see in the raw data. For very forward muon pair events, one of the other major contributions, as for the trigger, is from the Central Detector for which the Filter runs a fast pattern recognition program to find tracks originating from the vertex.

Pointing Endcap Muons

The filter algorithm is actually very simple, and this simplicity derives from the quality and ease of interpretation of the Muon Endcap data and lends great rejection power to the algorithm.

Firstly, active clusters of strips are identified. This is particularly easy since only the areas of interest found by the online cluster finding algorithm (DSP) are included in the endcap data seen by the filter and recorded to tape. The centre of the signal is just taken to be the strip with the highest ADC count, as long as it is above a small minimum value of 50 counts. The cut on the minimum size causes little problems in efficiency since about 98% of the true signals will achieve this. Using just the central strip to define the cluster position gains a lot in speed and loses little in resolution at the level required, as demonstrated later.

Once the clusters have been identified, the X and Y hits in inner layers and outer layers of each part of the detector are correlated. Every time a cluster in both X and Y occurs in the same active plane, *i.e.* a signal in both readout planes of one layer of chambers, then this is counted as a hit and the coordinate of the point is calculated from nominal chamber positions, which are good enough for the purposes of this algorithm. Then, for *every* pair of points separated by the lever

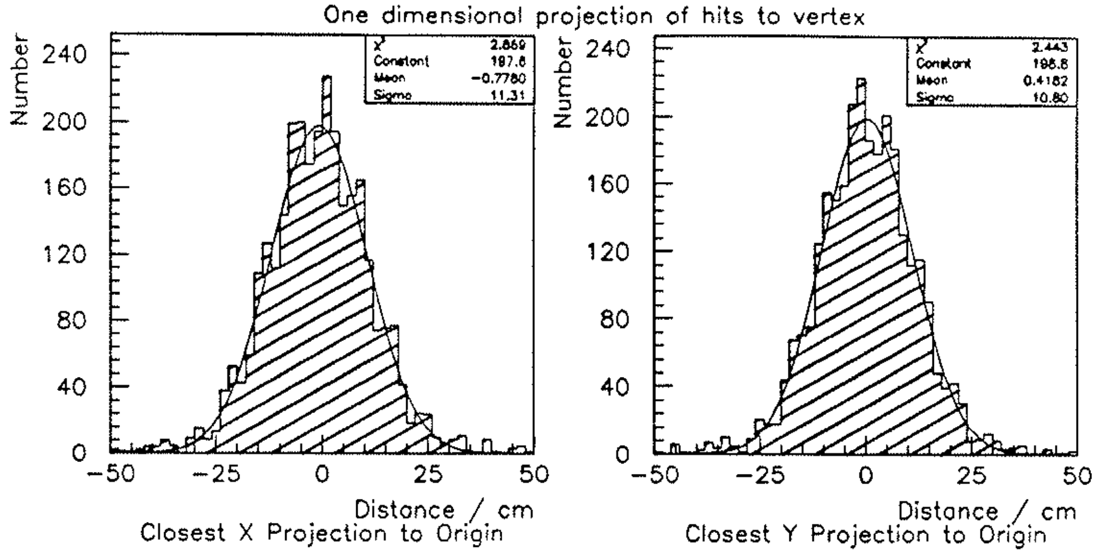

Figure 4.6: Fits of the x and y hit projections at the origin.

arm between the inner and outer chambers, the line of the two points is projected back to the plane $z = 0$ and the distance between the intersection and the origin is calculated. This distance, for high energy muons originating at the interaction point, undergoing little deflection in the magnetic field and intervening material, should be almost zero.

To demonstrate the accuracy achieved by this method, it is easiest to look at the resolution in 1 dimension (x or y coordinate) first. For selected dimuons with tracks in the endcaps, the track should project back to approximately zero *i.e.* towards the vertex. This was checked for a sample of 1990 muon pairs and the nearest projection to the expected zero was plotted for each of the x and y coordinates (figure 4.6). Both projections show small offsets from zero probably due to differences between nominal and actual chamber positions.

The resolution is seen to be about 11 cm, which agrees with expectations. Since the lever arm between hits is 65 cm, and the distance to the $z = 0$ plane is about 6 m, it implies a joint resolution of about 1.1 cm on the position of the two hits projected, or about 0.7 cm on each hit. This is reasonable although about a factor of two larger than possible with ideal calibrations. The basic accuracy of the hit finding method is 'plus or minus one strip', with the strips separated by

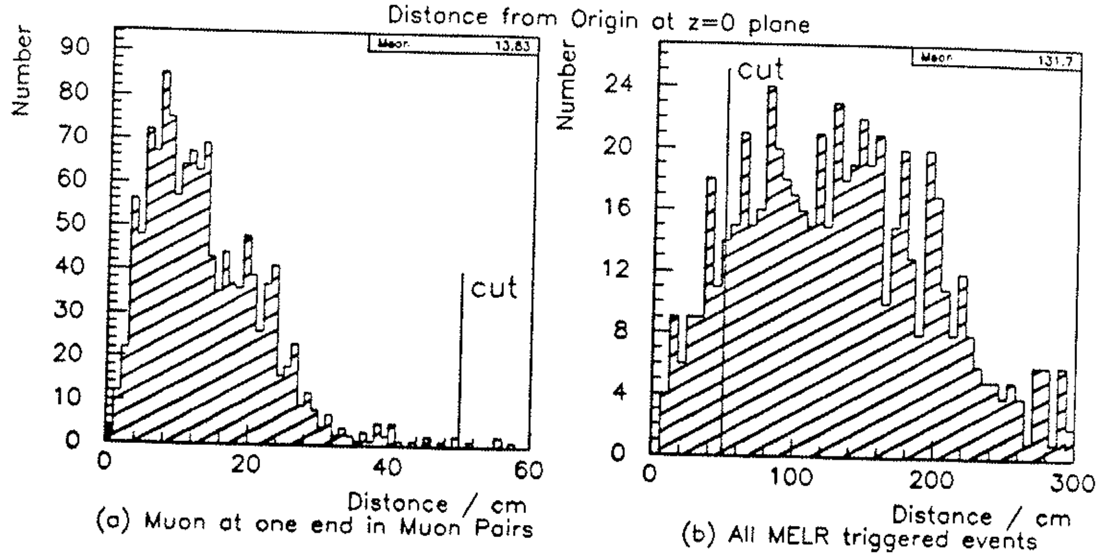

Figure 4.7: Filter cut parameter for muon pairs and all Muon Endcap events.

1 cm giving a r.m.s. value of about 0.3 cm.

The cut made on the distance from the origin in 2 dimensions to define a good pointing 'muon' track is that is must be less than 50 cm. This is shown to be safe, and manages to reject many cosmic rays where the distance can be very large. Also the algorithm requires only that one of the many projected tracks satisfies the minimum distance cut. For a well measured charged track traversing all four layers of the endcap, there will be four reconstructed coordinates — two in the inner layers and two in the outer. There will therefore be four combinations projected back to the origin, the best of which must pass the cut. Note also that for a muon pair with both muons in the endcap acceptance, only one will need to have a good projection. The distance from the origin of the best projection for just the signal of a muon in *one* end of the detector is plotted for a set of typical muon pair events in figure 4.7(a). Figure 4.7(b) shows a similar plot for any event triggered by the muon endcap, *i.e.* mostly cosmics.

The only problem with the algorithm is when there are many hits in the endcap, perhaps due to a cosmic shower or showering around a track from an event. In these cases (about 14% of MELR events), when there are more than ten hits in one quadrant, and projecting all the combinations would be too time consuming, the algorithm just selects the event for safety since it cannot decide if the event was good.

Efficiency of the Filter Algorithm

As pointed out above, the algorithm requires only *one* muon in either endcap to pass the selection cut. By using test samples of endcap $e^+e^- \rightarrow \mu^+\mu^-$ events selected by other detectors, it can be shown that for a single muon in the acceptance, the efficiency is $98.8 \pm 0.2\%$, essentially limited by the chamber efficiency itself. So for a muon pair with both muons in the acceptance, the chance that both will be missed is almost zero. This ensures that with the Central Detector pattern recognition, the filter efficiency is 100%.

The other important feature is the rejection power of the selection. The distinction between $e^+e^- \rightarrow \mu^+\mu^-$ and cosmic events is clear in figure 4.7. However, in a typical OPAL data-taking period, the number passing due to having too much activity is similar to the number that satisfy the pointing cut. Running the algorithm on data with filter rejection switched off, the fraction of MELR events normally rejected can be found. The break down is:

- 73% — rejected as cosmic
- 13% — selected as good pointing tracks
- 14% — selected due to large activity

4.1.3 Physics selection of Endcap Muons

All data selected by the Filter is automatically processed by ROPE, the reconstruction program for OPAL events. A further physics selection is made on these events based on the results of the reconstruction, and it is only these data that are easily available for analysis. It is therefore still important that there are independent methods of selection for all events.

The emphasis is slightly different here, since the most important part of the physics selection is made on useful tracks in the central detector. In the case of $e^+e^- \rightarrow \mu^+\mu^-$ events, if an event fails physics selection because no useful charged tracks are found due to inefficiencies and acceptance of the central detector, then there is little point in including that event in a muon pair selection. This is particularly true in the very forward region ($|\cos\theta| > 0.9$) where there are few hits in the central detector and measurements can be unreliable. So although events retained by an independent selection from the endcap cannot be counted as good muon pair events (since they will have no tracking information), they are still important as an independent selection used to understand and measure these tracking inefficiencies.

This objective of using endcap selected events as a check on the performance of the tracking means that the efficiency of the muon endcap selection is not the most important consideration, *i.e.* it need not be very high. Instead it is important to ensure that the selection does not introduce very many extra useless events that will take up valuable storage space.

Pointing Muon Endcap Segments

The selection algorithm is essentially the same as the filter selection, with a slightly different emphasis. The tracks used are now the track segments found by the Muon Endcap ROPE processor. These have the advantage of using the true surveyed chamber positions to obtain the best position and direction of tracks. Also the fitted segment combines all the hits in the four layers of chambers instead of just using two hits.

The only difference is that the cut on the distance from the origin at the $z = 0$ plane is reduced to 20 cm corresponding to the superior resolution and the need for better cosmic rejection. Also, to reduce background, when an event has more than five segments at one end, these segments are all disregarded; this decision is opposite to the filter algorithm's, where complicated events are automatically selected. However, like the filter algorithm, just one good muon track at one end can still satisfy the selection, so muon pairs, with hits at both ends, have the redundancy of needing only one segment at one end to pass the cut on the projected track.

The distribution of these extrapolated muon segments from the origin is shown

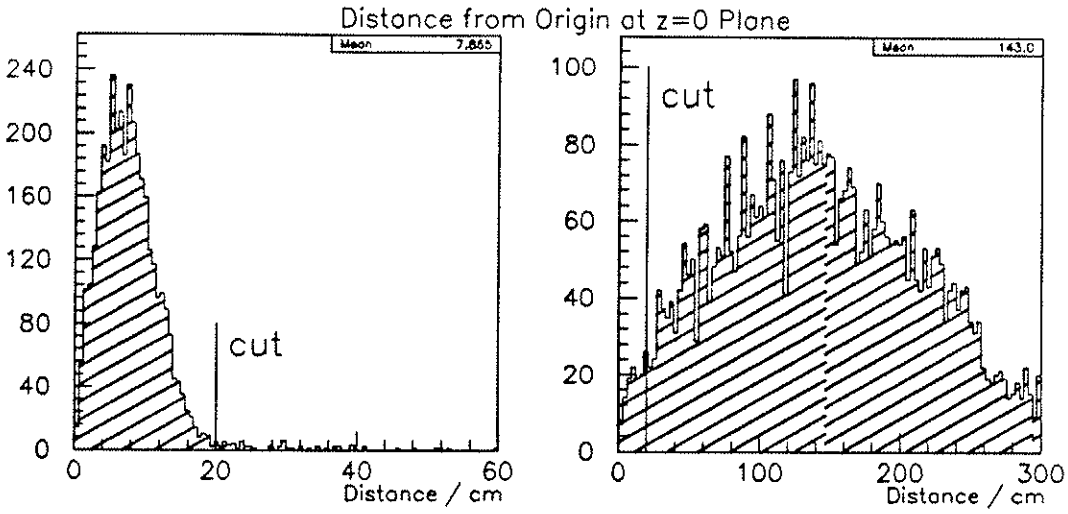

(a) Cut Parameter for muon at one end (b) Cut Parameter for all MELR events

Figure 4.8: Event selection parameter for muon pair and all events triggered by the Muon Endcap.

in figures 4.8(a) and (b) for typical muon pair events and general MELR triggered events respectively. The best value of the parameter at each end is plotted. If one of the muons of a good $e^+e^- \rightarrow \mu^+\mu^-$ event fails this cut, there is still a good chance the muon at the other end passed the cut. When compared with the equivalent plots for the filter selection, the average value is smaller, illustrating the greater resolution of segments found by the actual Muon Endcap reconstruction code.

Effectiveness of the algorithm

Looking at the $e^+e^- \rightarrow \mu^+\mu^-$ events again, the efficiency can be investigated by looking at the number of times a muon from a Z^0 decay is flagged by the algorithm when the event obviously passed through the endcap. It is found that in genuine muon pair events where a endcap segment is identified in the correct region, only 13% of these segments are rejected by the algorithm. Given that the reconstruction efficiency for formation of this segment in the muon endcap acceptance is about 96%, this means that a high energy muon in the acceptance at one end will pass the selection in 83% of cases. With the redundancy of two possible muons to identify in muon pair events, this gives an efficiency for selection of these events of approximately 97%, which, remembering that efficiency is not one of the major

Selection	Efficiency(%) for:		Percentage of
	Single Muon	Muon Pairs	OPAL Data
MELR Trigger	97*	94	14
Filter Pointing Hits	99	100	4
Pointing Segment	83	97	0.4

* Efficiency for MEL or MER

Table 4.5: Approximate details of selection effectiveness.

objectives, is very high.

The important feature for data storage is how many extra events this new selection gives. Firstly it can be seen that a good job of rejecting junk is achieved by the fact that over 90% of the events selected by the filter algorithm are now rejected. That is well over a thirty-fold reduction from the number of events which trigger MELR. For a typical run, the selection bit is set for about 1.4% of the events selected for storage. However, of these only 0.8% have no other selection bits set, and so only these add to the data load for OPAL. Since they must have little but muon endcap hits, these events will also be quite small, so are not a big problem. Combined with other physics selections, essentially no good $e^+e^- \rightarrow \mu^+\mu^-$ candidates are lost.

4.1.4 Summary

The efficiencies and amount of data selected at each stage of the data processing in OPAL is summarised in table 4.5 for the three muon endcap selection techniques. The figures given for the content of muon endcap selected data in the data as a whole is from a typical 1990 run, but the figures can vary a great deal between runs due to different background conditions and beam luminosities.

The success of the muon endcap as an independent detector did much to help the early analysis of $e^+e^- \rightarrow \mu^+\mu^-$ events in allowing a study with low systematic errors to be performed right down to $\cos\theta = 0.95$, far beyond the scope of most early analyses in different decay channels performed at OPAL due to the problems with understanding detector response in this difficult region.

4.2 The Measurement of Track Direction by the Muon Endcap

In the precise measurement of the $e^+e^- \to \mu^+\mu^-$ cross section, it is essential to know accurately the angular cut-off in the high $|\cos\theta|$ region. It is not possible to measure the complete angular range, and so the theoretical cross-section for the range measured must be estimated. With the level of statistics available, and the precise nature of the theory, it is necessary to know the angle to the level of a few mrad in theta. In the very forward region, the θ resolution of the tracking chambers is worse than in the barrel region. During initial analysis in the 1990 run, it became clear that this resolution could contribute significantly to the errors. Investigations made at the time into obtaining a reliable theta measurement for muon pair events in the cut-off region are presented below. The understanding of θ from all detectors has been improved since that time.

4.2.1 Comparison between the Central Tracking Chambers and the Muon Endcap

There are two methods of obtaining a measurement for the angle of a track in the tracking chambers within the endcap region. The standard measurement is that of the fitted angle of the hits in the chambers. Alternatively, it is possible to estimate the direction by the end-point method. In this case, only two points on the track are known, but these are known quite accurately. The two points are the interaction point and the point at which the charged particle exited the active area of the chambers, as derived from the last wire hit in the detector. The measurement of theta is found by simply connecting the two points. This algorithm is very simple, but since the intrinsic resolution in z of the jet chamber is poor, it can produce better results for θ determination.

The muon endcap also produces two different measurements of theta. The direction is measured by fitting the points measured within the chambers, and, in a similar way to the end-point method, the direction of a line joining the interaction point and the position of the track can be determined. This procedure is reasonable only when considering high momentum muons, as in $e^+e^- \rightarrow \mu^+\mu^-$ events, which deviate very little from a straight line. The intrinsic resolution in the measurement of track direction is about 10 mrad as derived from detector performance and geometry. It also suffers from deflections in track direction from scattering in the outer layers of OPAL. The θ determination from track position in the muon chambers suffers less from deviations, and the resolution from detector considerations should be about 1 mrad. It is this latter measurement which can be useful for comparison with other detectors.

Using muon pair events, it is generally easy to compare the results from different detectors, since there is no problem with mismatching multiple tracks. If for some reason a detector has more than one measurement associated to the muon, then the best match can be taken. In the case of the muon endcap, it is possible to take the best match in direction with the central detector track in order to avoid biasing the result. All the results shown are for good muon pairs in the endcap region of the detector, where a muon endcap track segment has been found.

An initial comparison of the central detector track direction derived from the reconstruction program and the equivalent muon endcap track revealed that the two were not very close, as shown in figure 4.9(a). This figure shows the difference in theta as measured in the two different ways. The joint resolution is about 30 mrad, which is poor enough to contribute significantly to errors in muon pair analysis.

By using the θ derived from the end-point calculation, the situation immediately becomes much better. Figure 4.9(b) shows the difference in theta now, where the joint resolution has been improved to about 8 mrad. However, the histogram shows a suspicious double peaked structure. On investigating, it was found that this was due to the fact that the differences from both ends of the detector are shown on the same histogram. If the same results are plotted separately for the left ($\cos\theta < 0$) and right ($\cos\theta > 0$) ends of the detector, then this distribution neatly splits into two — see figure 4.9(c). This illustrates the fact that the end-point measurement at *both* ends is consistently slightly nearer to the beampipe than the muon endcap measurement. The two distributions can be fitted with a

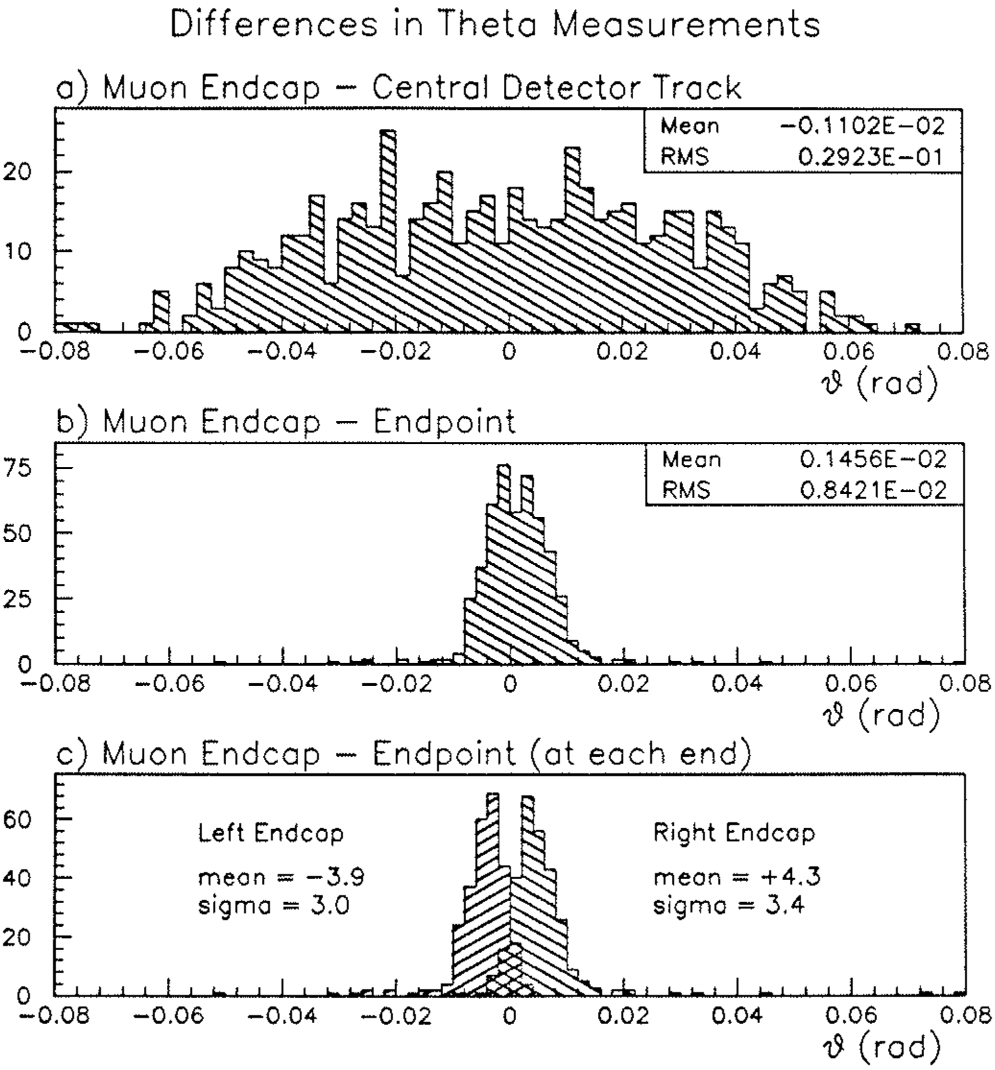

Figure 4.9: Difference in theta measurement between central detector and muon endcap for a single muon.

simple gaussian to estimate the resolution and mean. The joint resolution at both ends is now of the order of 3 mrad, but there is a systematic shift between the two data sets of the order of 4 mrad.

The fact that the joint resolution is now about 3 mrad shows that both methods must have a smaller resolution than this, but the systematic shift is now more of a problem. It is impossible to tell which of the two detectors is closer to the actual track direction, since both could easily produce the systematic behaviour observed. The end-point technique is likely to pull track measurements towards the beampipe if the last wire is missed, and a mismeasurement of the z-coordinate of the muon endcaps would also cause a shift of this sort. The only way to verify the measurement is by comparison with further detectors. A good candidate for this is the electromagnetic presampler.

4.2.2 Comparison between the Electromagnetic Presamplers and the Muon Endcap

A muon passing through the electromagnetic presamplers should leave a signal with a well defined position which can be associated to the central detector track. The presamplers have little depth, so can only make a measurement of the position of the muon, but this can be used, as with the muon endcap track position, to determine the muon direction from a knowledge of the vertex position.

Comparisons were made using the direction derived from hits in the presamplers with the direction from muon endcap information. The difference in theta for each measurement is shown in figure 4.10, this time as a scatter plot of the difference in theta against $\cos\theta$ at one end. The gap in data around $\cos\theta = 0.8$ corresponds to the gap in coverage between the presampler endcap and presampler barrel. The results can be analysed as with the central detector for joint resolution and systematic shifts, remembering to divide the data into left and right endcap in case of different systematics in the two regions. The full results are presented in the next section, but it can be seen from this figure that the agreement between the detectors is very good. Also it can be seen that the presampler barrel has a smaller spread than the endcap.

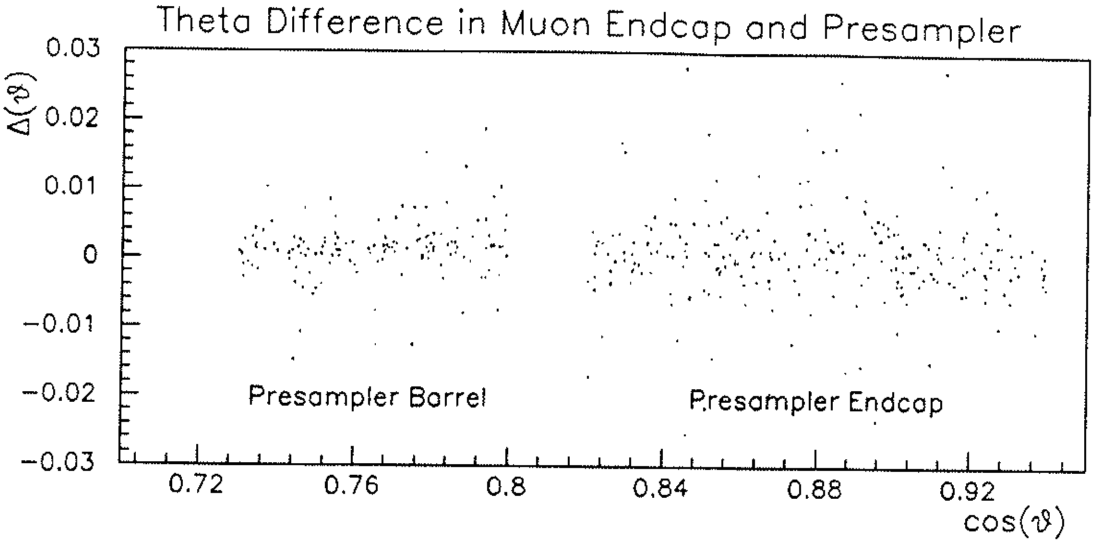

Figure 4.10: Difference in theta measurement between presamplers and muon endcap for a single muon (as a function of $\cos\theta$).

Direction Comparison	Endcap	Joint Resolution (mrad)	Systematic Shift (mrad)
ME - EP	Left	3.0	-3.9
ME - EP	Right	3.4	4.3
ME - PE	Left	2.9	0.0
ME - PE	Right	2.4	0.6
ME - PB	Left	1.7	-0.2
ME - PB	Right	1.4	1.1

ME — Muon Endcap EP — End-point
PE — Presampler Endcap PB — Presampler Barrel

Table 4.6: Results for comparison of θ measurements in muon pair events.

4.2.3 Conclusions

The result of comparing the various theta values in the two endcap regions of the detector are summarised in table 4.6. It is clear that the muon endcap and presampler barrel have the best joint resolution, which is consistent with both detectors each having a resolution of about 1 mrad. The figures also confirm that the systematic shifts are most serious for the end-point determination, and the other detectors, although not in perfect agreement, have more consistent data.

For the purposes of analysis of muon pairs, a good resolution was required in the region $\cos\theta = 0.95$. Clearly the presampler endcap resolution is not as good as the muon endcap, and it also had the disadvantage of being less efficient.

The results are consistent with the muon endcap having an intrinsic resolution of about 1 mrad, and a systematic shift of not more than the same figure. This was sufficiently accurate for the muon pair cross section measurement, and so, when available for an event, the muon endcap theta measurement was used. This was assumed to have a resolution of about 1 mrad, which is good enough that the error on this measurement is insignificant compared to others.

Chapter 5

A Measurement of $\tau \rightarrow \mu\overline{\nu}_{\mu}\nu_{\tau}$ Branching Ratio

With the large cross section for e^+e^- annihilation around the Z^0 resonance, LEP provides high statistics for standard e^+e^- physics giving the opportunity to measure many quantities other than those associated with the Z^0 resonance. For example, the reaction $e^+e^- \rightarrow Z^0 \rightarrow \tau^+\tau^-$ provides the possibility of studying the decay properties of the tau lepton.

The τ particle decays weakly (lifetime $\sim 3 \times 10^{-13}$ s), by emitting a virtual W boson, to either of the lighter leptons, *e.g.* $\tau \rightarrow \mu\overline{\nu}_{\mu}\nu_{\tau}$, or to one or more hadrons, *e.g.* $\tau \rightarrow \pi\nu_{\tau}$. The mass of the τ is about 1.78 GeV so that only decays to the lightest quark doublet are allowed. Remembering the quark colour degeneracy, this would suggest that the fraction of taus decaying to either e or μ should be about 20% in each case. These fractions, called the branching ratios, can be measured by studying the properties of the τ decay particles. Using only the data recorded in 1990, corresponding to a luminosity of 8.7 pb^{-1}, the reaction $e^+e^- \rightarrow \tau^+\tau^-$ allows precise measurements of these branching ratios comparable to or better than those performed at lower energy experiments. Further, an analysis of the momentum spectra of the decay particles to find the τ polarisation after the interaction can be used to determine the vector and axial couplings of leptons, as described in chapter 7.

In 1990, the OPAL collaboration presented results on the branching ratios $B(\tau \rightarrow e\overline{\nu}_{e}\nu_{\tau})$, $B(\tau \rightarrow \mu\overline{\nu}_{\mu}\nu_{\tau})$ and $B(\tau \rightarrow \pi\nu_{\tau})$ [25]. These were determined in a consistent way using only the barrel region of the detector (angular cut-off $|\cos\theta| = 0.68$), thus limiting statistics by only using 3,308 candidate $e^+e^- \to \tau^+\tau^-$ events. This cut was made since the analysis of the electron and pion channels becomes more difficult just outside this region due to showering in the pressure bell which contains the gas for the central detector, the situation improving again further out past the 'overlap' region. However this problem does not exclude the use of the endcap region for the μ decay mode. This chapter describes an extension of the standard OPAL analysis of $B(\tau \to \mu\overline{\nu}_\mu\nu_\tau)$ to a larger angular range.

5.1 Selection of $e^+e^- \to \tau^+\tau^-$ Events

5.1.1 General Selection Principles

The selection used is based on the OPAL line shape analysis [4] and the branching ratio analysis [26]. The original cosmic rejection using the Time of Flight counters restricts the angular range so must be loosened. Also, this selection is designed to be less biased between different decay modes, which is even more important than an understanding of the overall efficiency when attempting to measure the branching ratios.

There are two stages to the selection. Firstly events with low track multiplicity are separated from all the data taken by OPAL. This separates out lepton pair events which typically have a small number of good charged tracks and electromagnetic clusters. The identification of good tracks and clusters uses the standard definitions used in most OPAL analyses and they are described below.

Secondly, $e^+e^- \to \tau^+\tau^-$ events are distinguished from the other low multiplicity events, (*e.g.* Z^0 decays to other lepton pairs and two-photon reactions). An illustration of the general principle involved in this second stage is shown in figure 5.1 where the sum of good electromagnetic clusters is plotted against the sum of the momenta of good charged tracks in the Central Detector in the whole event, *i.e.* including both tau decays in an $e^+e^- \to \tau^+\tau^-$ event. There are four clearly distinguishable features in this scatter plot:

- electron pair events clustering around centre of mass energy in both variables;
- muon pair events near centre of mass energy in charged tracks, but depositing little energy in the calorimeters;
- tau pair events with both taus decaying to muons which populate the line with about 1 GeV in the calorimeter, but with a wide range of track momenta;
- general tau pair events which are distributed widely over the plot as the taus decay to various final states.

Also included at this stage will be the two photon events (*e.g.* $e^+e^- \rightarrow \mu^+\mu^-e^+e^-$ where most of the energy is taken away by the scattered electron and positron) which populate the area of low energy in both detectors, and thus mix with the tau pair events, implying a different method is needed to reduce the background from these events.

5.1.2 Detailed Selection Cuts

Firstly good tracks and electromagnetic clusters are defined:

- a good charged track must satisfy:

$$\begin{aligned}
\text{number of jet chamber wires hit} — N^{\text{CJ}}_{\text{Hits}} &\geq 20 \\
\text{momentum of tracks perpendicular to the } z \text{ axis} — p_{\perp} &\geq 100 \text{ MeV} \\
\text{impact parameter (see section 2.3.2)} — |d_0| &\leq 2.0 \text{ cm} \\
z \text{ at closest point (see section 2.3.2)} — |z_0| &\leq 50 \text{ cm} \\
\text{radius of innermost wire in jet chamber} — R^{\text{wire}}_{\text{min}} &\leq 75 \text{ cm}
\end{aligned}$$

- a good electromagnetic cluster must satisfy:

$$\begin{aligned}
\text{Barrel: uncorrected electromagnetic energy} — E_{\text{Raw}} &\geq 100 \text{ MeV} \\
\text{Endcap: uncorrected electromagnetic energy} — E_{\text{Raw}} &\geq 200 \text{ MeV} \\
\text{number of blocks in cluster} — N_{\text{Blocks}} &\geq 2 \\
\text{largest fraction of energy in one block} — E^{\text{Fract}}_{\text{Max}} &\leq 0.99
\end{aligned}$$

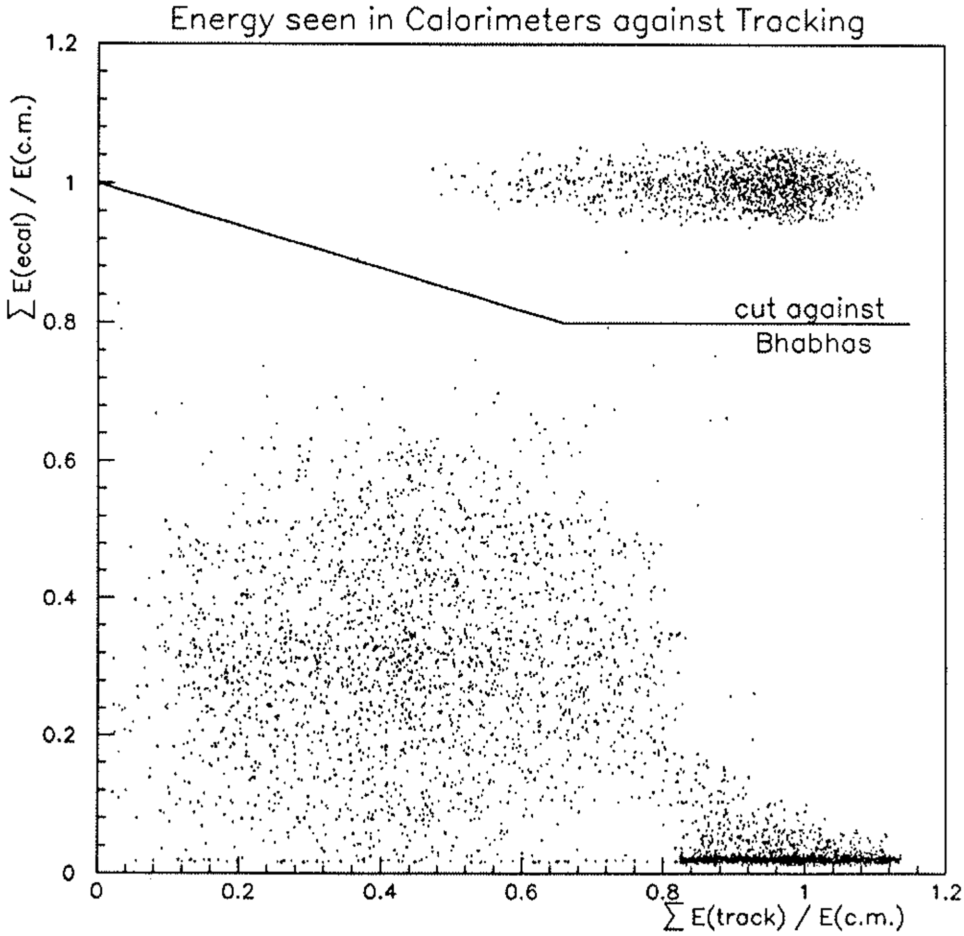

Figure 5.1: Comparision of energy deposited in the electromagnetic calorimeters with summed momentum of charged tracks.

Next, tau pairs are selected by imposing cuts on the characteristics of the events. These cuts are:

1. The number of good charged tracks must satisfy

$$2 \leq N_{\mathrm{Chrg}}^{\mathrm{Tot}} \leq 6$$

2. The number of good electromagnetic clusters must satisfy

$$N_{\mathrm{Clust}}^{\mathrm{Tot}} \leq 10$$

3. There must be exactly two 'jets' in the events. A jet in this case is defined by a cone finding algorithm which associates charged tracks and clusters within a cone of half-angle 35°. The number of these jets needed to include all the tracks and clusters will be two in most real tau events, one for each tau decay. Jets with less than 1% of beam energy are not counted.

4. For rejection of two photon events, the two jets must satisfy

$$\text{Acollinearity} < 15^{\circ},$$

where the acollinearity is the angle between the two jet directions in three dimensions. This cut relies on the fact that two photon events are generally boosted along the beam axis, whereas most tau events will be back-to-back.

5. A cut on the angular range is applied to the average $\cos\theta$ of the jet directions found from vector addition of the momenta of the component tracks *and* clusters.

$$|\cos\theta_{\mathrm{ave}}| < 0.90$$

6. Electron pairs are removed by cuts on summed track and cluster energies. An event is rejected if both

$$\sum E_{\mathrm{ecal}} > 0.8\, E_{\mathrm{CM}} \qquad \textbf{AND} \qquad \sum E_{\mathrm{ecal}} + 0.3 \sum E_{\mathrm{trk}} > E_{\mathrm{CM}}.$$

This cut corresponds to the line shown in figure 5.1.

7. Muon pairs are rejected if they are identified by the standard OPAL selection [27]. This selects on two good high momentum tracks with signals typical of a minimum ionising particle in the calorimeters or muon chambers which line up with the extrapolated tracks.

8. Remaining two-photon background is reduced by cutting out events with low visible energy, where visible energy is the sum for the two jets of the maximum of charged track and electromagnetic energy for each jet. If the total visible energy is less than 3% of $E_{\rm CM}$ or if the total visible energy is less than 20% of $E_{\rm CM}$ and the momentum transverse to the beam is less than 2 GeV, then the event is rejected.

5.1.3 Selected Tau Pair Events

Using these cuts on good data taken in the 1990 run, 4,691 candidate $e^+e^- \rightarrow \tau^+\tau^-$ events are found. The efficiency was estimated from 50,000 KORALZ [28] tau pair events and found to be $76.5 \pm 0.2(stat) \pm 1.4(sys)\%$, where the systematic error quoted is estimated from varying cut parameters [29]. Some indication that the Monte Carlo is imitating the data is that the efficiency reduction with larger $|\cos\theta|$ is similar to that seen in real data (see figure 5.2).

The odd distribution in the region of $|\cos\theta| = 0.7$ is due to a well known effect in the data whereby the Jet Chamber tracks tend to have a systematic shift to higher $\cos\theta$, but some are brought back inwards to their correct z value by matching with z-chamber hits. This means a sharp fall occurs at the limit of the z-chambers.

It is important to understand the background from other Z^0 decay modes. These have been be estimated by Monte Carlo and are shown in table 5.1.

Also the relative efficiency of the cuts for the selection of different decay modes must be accounted for when calculating the branching ratio. This is to counteract the possibility that there is a bias in the selection of tau pairs against certain decay modes, which would tend to reduce the observed branching ratio. The relative efficiency for $\tau \rightarrow \mu\bar{\nu}_\mu\nu_\tau$ events has been found from the 50,000 Monte Carlo events to be 0.980 ± 0.006. This means that this selection of $e^+e^- \rightarrow \tau^+\tau^-$

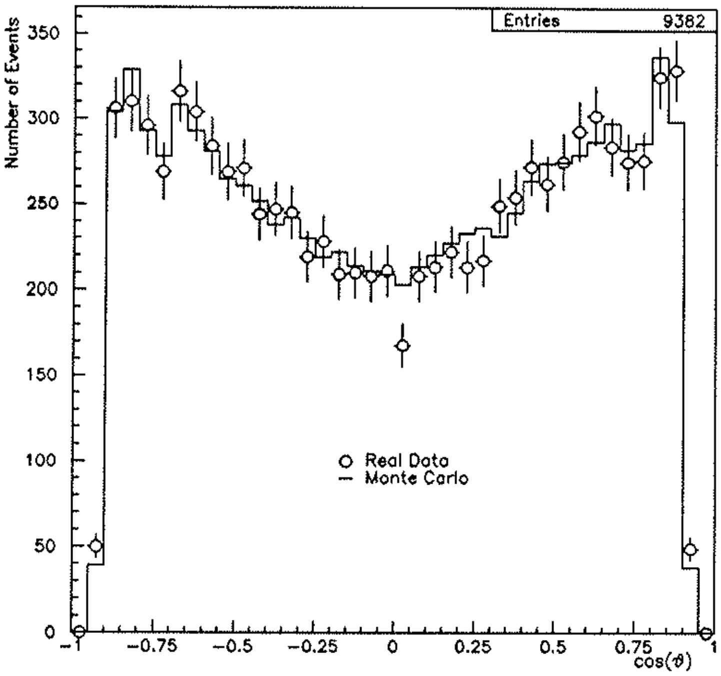

Figure 5.2: Selected tau pair events $\cos\theta$ distribution for Monte Carlo and real data.

Background	Contamination(%)
$e^+e^- \to e^+e^-$	0.3 ± 0.3
$e^+e^- \to \mu^+\mu^-$	1.1 ± 0.9
$e^+e^- \to q\overline{q}$	0.7 ± 0.3
$e^+e^- \to e^+e^-X$	0.2 ± 0.2
Total	2.3 ± 1.1

Table 5.1: Estimates of backgrounds to $e^+e^- \to \tau^+\tau^-$ events.

slightly favours other tau decay modes over the decay to a muon, so the final ratio is divided by this figure to allow for this factor. The value of this bias is only investigated for the relative *selection* efficiency whereas to be accurate it also ought to include any bias introduced by the trigger and filter. However, the efficiency for these is practically 100% for those events which pass the selection, no matter what decay modes are involved.

5.2 Selection of $\tau \to \mu\overline{\nu}_\mu\nu_\tau$ Candidates

As stated above, this analysis provides an attempt to extend the angular range of the standard OPAL B($\tau \to \mu\overline{\nu}_\mu\nu_\tau$) analysis. The cuts detailed below are based very heavily on those used in the barrel region for published papers (see [30]).

The original selection cuts were hoped to be useful at all angles. However on investigation of the region beyond $|\cos\theta| = 0.68$, it was found that some of the cuts were inappropriate and also that the Monte Carlo was not modelling the response of various detectors sufficiently well, so additional smearing had to be applied to the Monte Carlo data. These changes are justified in section 5.2.2, but first the selection used for this analysis is described below.

5.2.1 Details of Selection Cuts

The two 'jets', as described in the previous section, are now treated separately and each is subjected to the same cuts to identify decays to a muon. These cuts are:

1. The number of charged tracks in the jet cone must be one.

2. Hadronic decays are reduced by rejecting events with a significant activity in the Hadron Calorimeter typical of a hadron — *i.e.* rejecting events with:

   $$N^{\mathrm{HCAL}}_{\mathrm{hits/layer}} \geq 3 \qquad \text{with} \qquad N^{\mathrm{HCAL}}_{\mathrm{layers}} \geq 3$$

   where $N^{\mathrm{HCAL}}_{\mathrm{hits/layer}}$ is the average number of hits per layer hit, and $N^{\mathrm{HCAL}}_{\mathrm{layers}}$ is the number of layers hit, all within the jet cone, the cone being defined as earlier.

3. Further rejection of hadronic events with an associated π^0 is achieved by a cut on the invariant mass calculated by combining the track momentum (assuming pion mass) and the residual electromagnetic cluster after subtracting 0.5 GeV as the energy deposited by a minimum ionising particle. The assumption is that the tau decayed into hadrons including a charged pion and one or more neutral pions. An event is rejected if:

$$M_{\text{inv}} > 0.3 \text{ GeV}$$

This should reject decays such as $\tau \rightarrow \rho\nu_\tau$ but not $\tau \rightarrow \mu\overline{\nu}_\mu\nu_\tau$ decays with collinear final state radiation.

4. The track has to pass at least *two* out of three muon identification criteria in the three relevant detectors. These are:

   - Muon detector — **MU**

   $$N_{\text{hits}}^{\text{MU}} \geq 2 \qquad \textit{or} \qquad \text{track not in acceptance}$$

   Where $N_{\text{hits}}^{\text{MU}}$ is the number of layers of Muon Detector (barrel or endcap) hit in the jet cone.

   - Hadron calorimeter — **HCAL**

   $$N_{\text{layers}}^{\text{HCAL}} \geq 4 \qquad \text{with} \qquad N_{\text{hits/layer}}^{\text{HCAL}} < 3$$

   which is typical of a non-hadronic interaction in the Hadron Calorimeter.

   - Electromagnetic calorimeter — **ECAL**

   $$E_{\text{cls}} < 2 \text{ GeV}$$

   E_{cls} is the total electromagnetic cluster energy in the jet cone.

5. It is important to remove residual $e^+e^- \rightarrow \mu^+\mu^-$ events from this selection as they would produce a large background of false $\tau \rightarrow \mu\overline{\nu}_\mu\nu_\tau$ events. To do this, a jet is rejected if the *opposite* jet satisfies the following looser muon identification cuts:

- One charged track in cone.
- Track satisfies at least one of the three muon identification criteria.
- $$x_\mu \equiv \frac{p_{\rm trk} + E_{\rm cls} - 0.5\ \rm GeV}{E_{\rm beam}} \geq 0.8$$

The final cut on the x_μ, the energy of the decay product as a fraction of beam energy, is to ensure that events with low energy muons — far likelier to be from tau decay than simple $e^+e^- \rightarrow \mu^+\mu^-$ events — are retained.

6. To ensure that the track momenta are well measured, a candidate is rejected if it approaches the Jet Chamber anode-wire plane to within 0.3°. In the version of the reconstruction code used for this analysis, momentum resolution in these regions was poor.

7. To remove the less well understood low muon momentum range (below about 5 GeV where the muon is less likely to reach the outer detectors), a cut is placed on the momentum as a fraction of beam energy (x_μ):

$$x_\mu \equiv \frac{p_{\rm trk} + E_{\rm cls} - 0.5\ \rm GeV}{E_{\rm beam}} > 0.05$$

This quantity is defined in this way to include energy deposited in the electromagnetic calorimeter in radiative events, the subtraction of 0.5 GeV being to compensate for the double counting of the energy deposited by the muon itself.

To give some confidence that these cuts are useful and modelled well by Monte Carlo, figure 5.3 shows the distributions of some of the quantities used. The figures show both the real data $\tau \rightarrow \mu\bar{\nu}_\mu\nu_\tau$ candidates and the Monte Carlo $\tau \rightarrow \mu\bar{\nu}_\mu\nu_\tau$ events selected along with the additional events from the various backgrounds, both from other tau decays and completely different reactions. The distributions of the variables are shown before the relevant cuts are made on them.

5.2.2 Adaptations Required for Endcap Analysis

The differences between the cuts used for the original barrel analysis and the modified analysis to study τ decays to $|\cos\theta| = 0.9$ are described below.

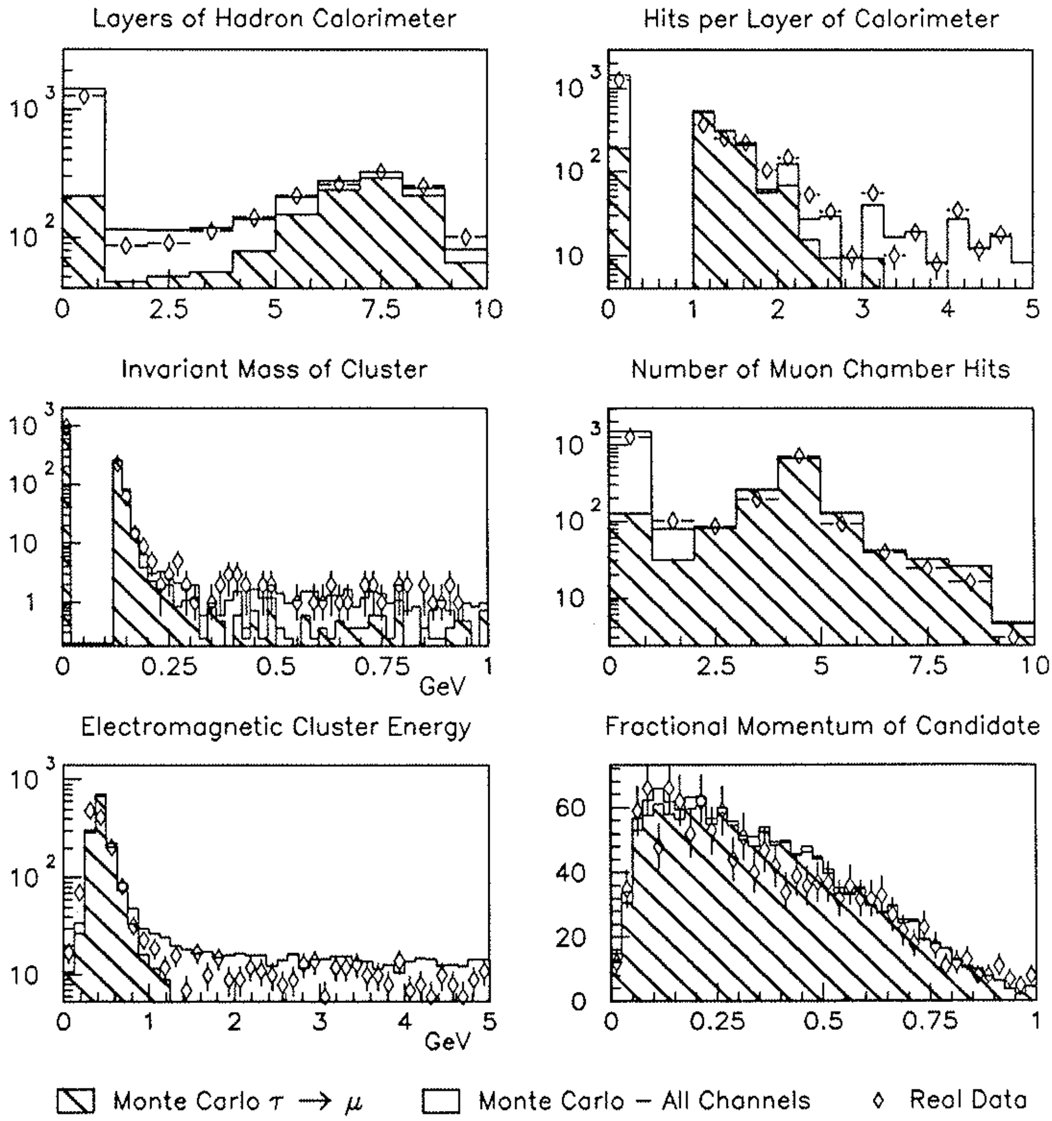

Figure 5.3: Distribution of cut variables for $\tau \rightarrow \mu\overline{\nu}_\mu\nu_\tau$ analysis with all other cuts applied.

The most obvious differences in the analysis need little explanation. Originally the angular range was restricted to $|\cos\theta| = 0.68$ and so it was possible to use a cosmic veto dependent on the Time of Flight detector. This veto has to be dropped for events outside the acceptance of the Time of Flight. Also originally it was required that each candidate track had more than 100 central detector hits — this requirement was dropped due to the fact that less hits are possible for tracks entering the endcap region of the jet chamber. The other changes require more discussion.

Muon Identification and Efficiency

The most problematical area is the muon identification in the endcap region. It is fairly simple in the barrel since there are three independent detectors, all with good coverage. The identification can therefore require two out of three detectors to have signals typical of a muon. In the endcap, the geometry is much more complicated, with large gaps in coverage of the Hadron and Muon Chambers. Since these gaps are often in the same angular range, identification by two detectors is impossible and so this cuts out a lot of potential events.

For this reason the muon identification cut is loosened compared to the original analysis. A candidate is now counted as identified by the Muon Chambers either if it has two or more hits in the usual way, *or* if it is not in the acceptance. Then only identification by *one* of the Electromagnetic or Hadron Calorimeter is required to accept the event. Since the Hadron Endcap has a fairly small angular acceptance, it follows that the identification then mostly depends on the Electromagnetic Calorimeter. Fortunately this has a fairly even acceptance with good efficiency in this region. The consequence is that there is more background (about 4% compared with 3% before), mostly from $\tau \to \pi\nu_\tau$ events in the endcap region, but the efficiency is more equal over all angular ranges.

There is also a related problem that, since the coverage is less uniform, the estimation of angular acceptance and efficiency by the Monte Carlo is more sensitive to the exact position of the edges and so more prone to error. In the barrel region the efficiency is very high and modelled well by Monte Carlo, as can be checked

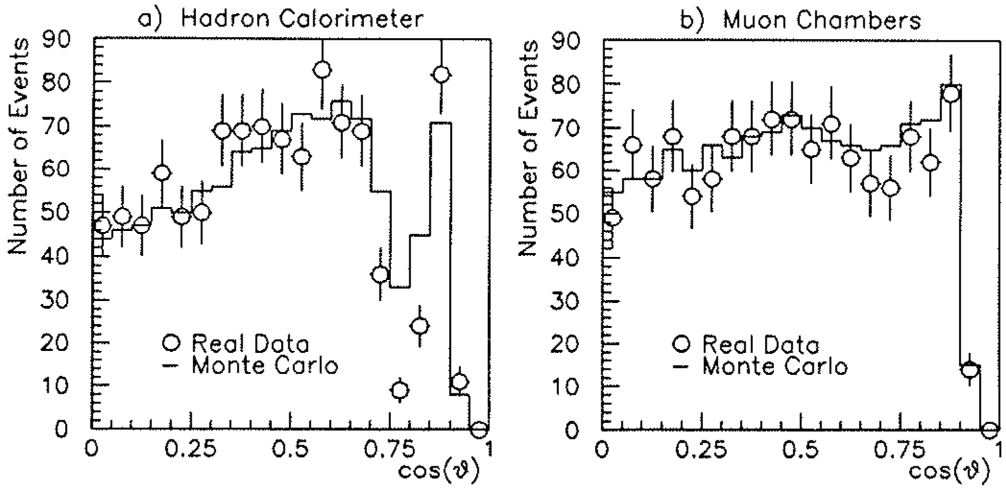

Figure 5.4: Angular distribution of $\tau \rightarrow \mu\overline{\nu}_\mu\nu_\tau$ events identified by a) Hadron Calorimeter and b) Muon Chambers before correction to the Monte Carlo.

by comparison with muon pair data. However, it is obvious when looking at the $\tau \rightarrow \mu\overline{\nu}_\mu\nu_\tau$ candidates identified as muons by each detector that the Monte Carlo efficiency for the Hadron Calorimeter is too high in the endcap region. It is also a problem to a lesser extent for the Muon Chambers as can be seen in figure 5.4. In the region $0.7 < |\cos\theta| < 0.85$, there is a significant difference in the Hadron Calorimeter identification efficiency. It is not so obvious for the Muon Chambers, but there is a suggestion of a difference above $\cos\theta = 0.7$. This is only a very weak effect, but can be investigated easily at the same time and in a similar way to the Hadron Calorimeter problem.

The problem can also be seen by looking at the distributions of the number of hits in these detectors in the angular regions causing problems. These are shown for both real data and Monte Carlo in figures 5.5(a) and (b). The Hadron Calorimeter simulation is obviously too optimistic. For the Muon Chambers it is important to concentrate on the ratio of 3 to 4 hit events — a lot of the other bins are subject to other simulation problems associated with overlap regions, but this ratio is a very good indication of individual chamber efficiency. The real data shows more 3 hit events, meaning the efficiency of each layer is slightly less than predicted in Monte Carlo. Since the cuts for muon identification are made on these variables, it is important to improve the simulation of the distribution of

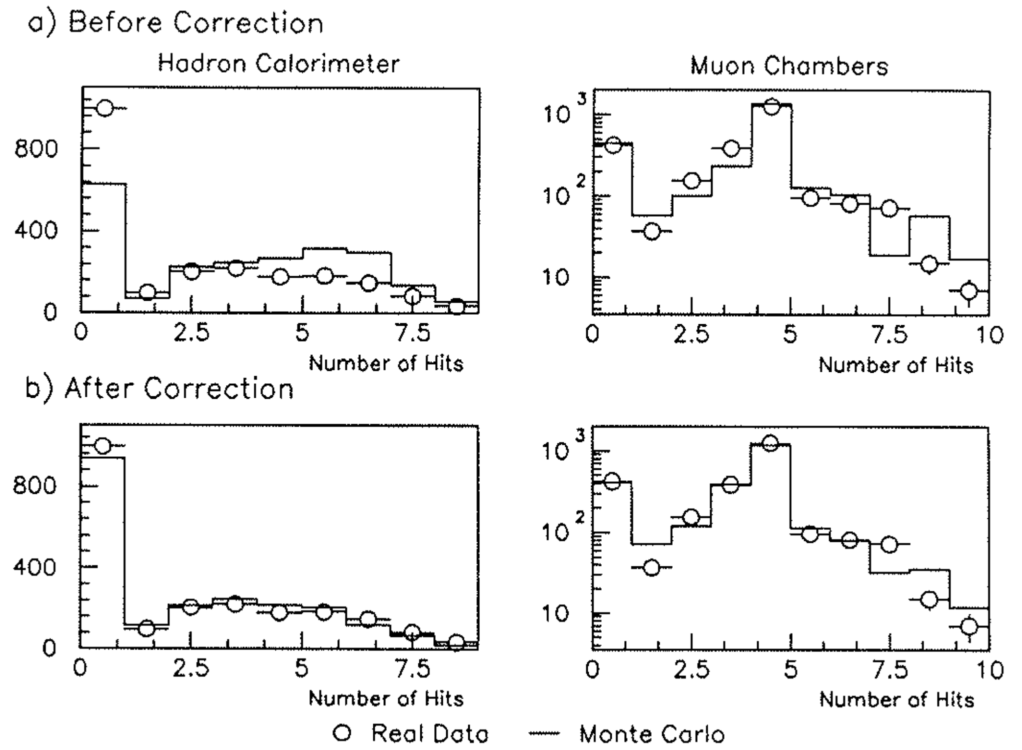

Figure 5.5: Number of hits in Hadron Calorimeter and Muon Chambers before and after correction to the Monte Carlo.

these variables.

To solve this problem, $e^+e^- \to \mu^+\mu^-$ data can be used to obtain the real identification efficiency by each detector. To try to fit the actual response of the detectors in a way which is appropriate to the detector, the Monte Carlo was modified so that hits in the chambers were eliminated randomly producing a fixed probability (different for muon chambers and hadron calorimeter) that any hit would actually be excluded from the analysis. Thus an extra inefficiency over that in the original GOPAL package was added for these regions. The distributions of hits found for each muon in muon pair data was then fitted against those found from Monte Carlo with various values of the extra inefficiency. The best fit was used for the final analysis.

When the best values were found to fit the muon pair data, it was found that identification efficiency of the Hadron Calorimeter, in the region $0.7 < |\cos\theta| < 0.85$, was reduced by about 11%. For the Muon Chambers, the extra loss in efficiency is only about 1% above $\cos\theta = 0.7$, emphasising that this is a very small

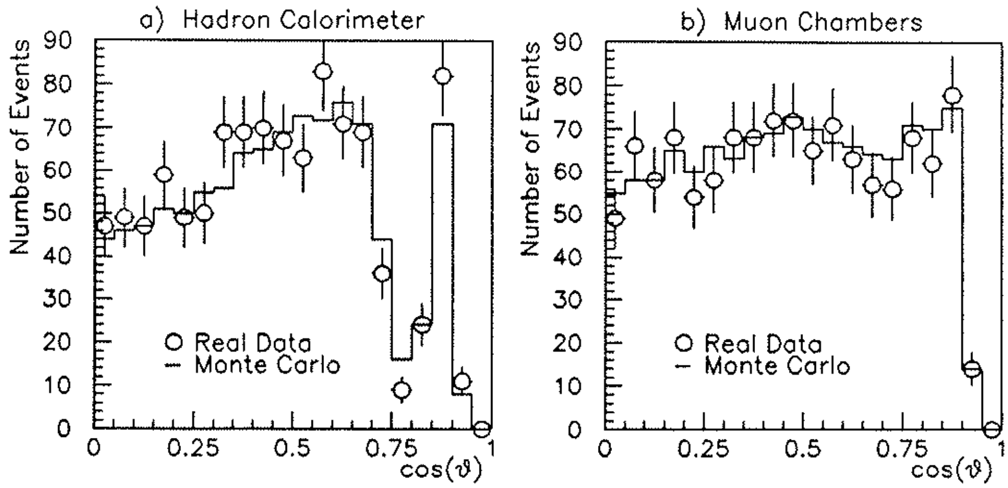

Figure 5.6: Angular distribution of $\tau \rightarrow \mu\overline{\nu}_{\mu}\nu_{\tau}$ events identified by a) Hadron Calorimeter and b) Muon Chambers after correction to the Monte Carlo.

effect. The fitted distribution of the number of hits can be seen in figure 5.5, both before and after this modification to the Monte Carlo. The improvement for the Hadron Calorimeter is obvious, but for the Muon Chamber hits it should be stressed that the only good indication is the three to four hit ratio, which shows better agreement. Also the new angular distribution of the identified $\tau \rightarrow \mu\overline{\nu}_{\mu}\nu_{\tau}$ decays from Monte Carlo tau pairs is shown in figure 5.6, along with the corresponding data to illustrate their similar shapes after the modification.

Invariant Mass

The final problem that was encountered when using the selection cuts was that the invariant mass veto cut out more events than expected in the endcap region. This can be seen in figure 5.7(c) where the distribution is flattened below the cut of 0.3 GeV compared to the shape of the equivalent distributions in the barrel and Monte Carlo. On investigation it was discovered that this was due to poorer track resolution in the central tracking chamber in this region. The increased misalignment between tracks and electromagnetic clusters due to poorer resolution meant that the calculated invariant mass was often too large. The effect was also partly aggravated by the fact that the Electromagnetic Endcap position calibration is based on electrons, which have a different shower shape to minimum ionising

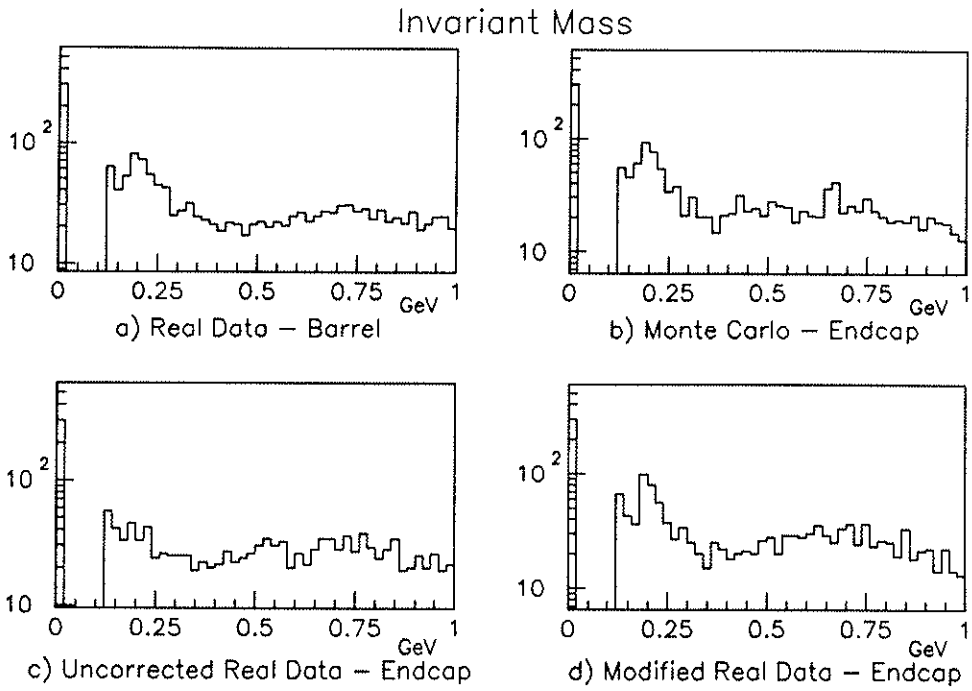

Figure 5.7: Invariant mass of jet calculated for various regions and data sets.

particles in the horizontal lead-glass blocks. This means that the cluster tends to be positioned about 1 mrad further from the beam axis in theta.

The problem was solved by using the track position as derived from the end-point extrapolation in the jet chamber. This is the value of θ obtained by using the interaction point and the point at which the particle left the jet chamber as two points on the track. Using this and by correcting the cluster position for events in the acceptance of the Electromagnetic Endcap, the invariant mass calculated becomes closer in distribution to that seen in the Monte Carlo and in the barrel region. These are shown in figure 5.7. Note that the majority of $\tau \rightarrow \mu\overline{\nu}_\mu\nu_\tau$ candidates lie in the zero bin since they have less than 0.5 GeV associated to the track. The region below the cut of 0.3 GeV is now not suppressed, unlike the uncorrected data.

As seen in the next section, after all these corrections, the data are quantitatively similar in the endcap to the barrel. This was not the case before these alterations were introduced.

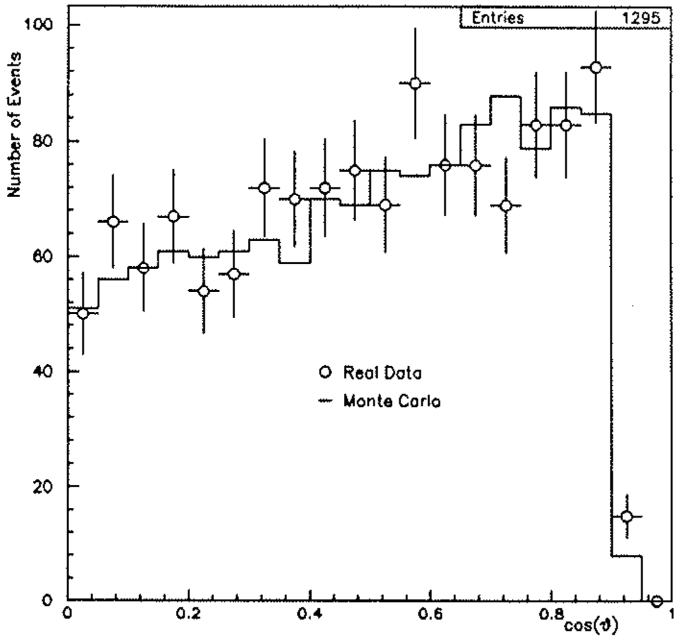

Figure 5.8: Angular distribution of $\tau \to \mu\overline{\nu}_\mu\nu_\tau$ candidates.

5.2.3 Selected $\tau \to \mu\overline{\nu}_\mu\nu_\tau$ Events

The final sample of $\tau \to \mu\overline{\nu}_\mu\nu_\tau$ candidates contains 1,295 jets out of the original tau pair sample containing 9,382 jets. The angular distribution of these events is shown in figure 5.8 with the Monte Carlo tau pair events scaled to the same number of selected tau pair events. The efficiency for selection of $\tau \to \mu\overline{\nu}_\mu\nu_\tau$ events (defined as number selected over number generated in Monte Carlo) is found from the 50,000 KORALZ events to be $80.8 \pm 0.5\%$, where the error quoted is purely statistical.

The background in the real data is estimated from the same tau pair Monte Carlo events and also Monte Carlo events for other Z^0 decays. The results of this background analysis are summarised in table 5.2, where the errors quoted are purely statistical. As can be seen, the major background is from $\tau \to \pi\nu_\tau$ events which are difficult to distinguish in the region of poor coverage by the muon detectors.

Background	Contamination
$\tau \to \pi\nu_\tau$	2.7 ± 0.4
$\tau \to$ other	0.8 ± 0.2
non-τ	0.5 ± 0.3
Total	4.0 ± 0.6

Table 5.2: Estimates of contamination in $\tau \to \mu\overline{\nu}_\mu\nu_\tau$ candidates.

5.3 Calculation of $\mathrm{B}(\tau \to \mu\overline{\nu}_\mu\nu_\tau)$

Using the above measurements, an estimation of the $\tau \to \mu\overline{\nu}_\mu\nu_\tau$ branching ratio can be made using the formula

$$\mathrm{B}(\tau \to \mu\overline{\nu}_\mu\nu_\tau) = \frac{N_{\mathrm{Cand}}^{\tau\to\mu}(1 - f_{\mathrm{Bkgd}}^{\mathrm{non}-(\tau\to\mu)})}{N_{\mathrm{Cand}}^{\tau}(1 - f_{\mathrm{Bkgd}}^{\mathrm{non}-\tau\tau})} \frac{1}{\epsilon_{\mathrm{eff}}^{\tau\to\mu}} \frac{1}{\epsilon_{\mathrm{rel}}^{\tau\to\mu}}.$$

The symbols, meanings and values are listed below.

- $N_{\mathrm{Cand}}^{\tau\to\mu}$ is the number of $\tau \to \mu\overline{\nu}_\mu\nu_\tau$ candidates (1295)
- N_{Cand}^{τ} is the number of τ jets analysed (9382)
- $f_{\mathrm{Bkgd}}^{\mathrm{non}-(\tau\to\mu)}$ is the background contamination from other τ decays and Z^0 decays ($4.0 \pm 0.6\%$)
- $f_{\mathrm{Bkgd}}^{\mathrm{non}-\tau\tau}$ is the background in the original $\mathrm{e}^+\mathrm{e}^- \to \tau^+\tau^-$ sample from other events ($2.3 \pm 1.1\%$)
- $\epsilon_{\mathrm{eff}}^{\tau\to\mu}$ is the efficiency for selecting taus decaying to a muon found from the Monte Carlo generated $\tau \to \mu\overline{\nu}_\mu\nu_\tau$ decays ($80.8 \pm 0.5\%$)
- $\epsilon_{\mathrm{rel}}^{\tau\to\mu}$ is the efficiency (described in section 5.1.3) for detecting $\tau \to \mu\overline{\nu}_\mu\nu_\tau$ decays relative to the other τ decay modes after the selection of tau pair events (0.980 ± 0.006)

The value of the branching ratio obtained from this calculation is
$\mathrm{B}(\tau \to \mu\overline{\nu}_\mu\nu_\tau) = 17.1 \pm 0.4$ (statistical errors).

To estimate the systematic error, the method of varying analysis parameters was used. The cuts were adjusted around the values used in the final selection, and the branching ratio calculated using the new cut values throughout the analysis

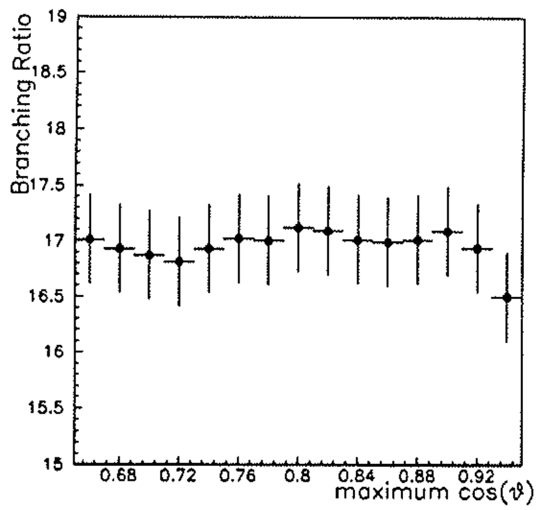

Figure 5.9: Value of branching ratio as a function of the $\cos\theta$ angular cut-off.

chain. The magnitude of the effect of these variations on the branching ratio was then used as an estimate of the errors. Also efficiencies were checked by comparison with real muon pair data selected by independent techniques. This was especially useful for the most critical area of errors from the muon identification algorithm in the region of poor muon detector coverage.

From these studies it was found that the value depended most severely on muon identification and angular cut-off, and these are assumed to be the most significant errors. The variation using slightly different muon identification techniques was approximately 0.4% in the branching ratio. Figure 5.9 shows the branching ratio calculated when using different values of $\cos\theta_{\mathrm{max}}$. The value of 0.9 used in the analysis hopefully avoids the onset of edge effects in the very forward direction. The systematic error is estimated as 0.2% from this. Most of the other factors had an effect at about the 0.1% level, although the cut on the distance from the anode was more significant at 0.2%. Adding the contributions in quadrature gives a final value of the systematic error of 0.5%.

5.4 Conclusions

The result of this analysis for the angular range $|\cos\theta| < 0.9$ is a value for the $\tau \rightarrow \mu\overline{\nu}_\mu\nu_\tau$ branching ratio of:

$$\mathrm{B}(\tau \rightarrow \mu\overline{\nu}_\mu\nu_\tau) = 17.1 \pm 0.4(stat) \pm 0.5(sys) \;\; \%$$

This is consistent with the barrel region result for the same data which was $16.8 \pm 0.5 \pm 0.5\%$. The barrel result is even nearer when using data from 1991, as presented in recent OPAL results [25] where it was quoted as $17.2 \pm 0.4 \pm 0.4\%$. The result is also in good agreement with recent results from other LEP experiments [31] and an average of all results including LEP which gives a value of 17.49 ± 0.24 (see [32]).

As described in section 6.3.1, the accurate measurement of the leptonic decays of the tau gives an insight into lepton universality. The easiest way to see this is from the standard model prediction for the tau lifetime (τ_τ) in terms of the muon lifetime (τ_μ).

$$\tau_\tau = \tau_\mu \left(\frac{\mathrm{G}_\mu}{\mathrm{G}_\tau}\right)^2 \left(\frac{\mathrm{m}_\mu}{\mathrm{m}_\tau}\right)^5 \times \mathrm{B}(\tau \rightarrow \mu\overline{\nu}_\mu\nu_\tau) \times \frac{1}{F_{\mathrm{ps}}}$$

The F_{ps} is a phase space factor due to the non-negligible mass of the muon. Firstly it can be noted that the slightly higher branching ratio for $\tau \rightarrow \mathrm{e}\overline{\nu}_\mathrm{e}\nu_\tau$ of $17.92 \pm 0.40\%$ from the Particle Data Group [33] is consistent with this phase space factor confirming lepton universality for electrons and muons. Then using measured values for the masses and lifetimes of the leptons, a value for the ratio of the Fermi Coupling Constants, $\mathrm{G}_\tau/\mathrm{G}_{\mathrm{e},\mu}$, can be derived. Using recent values for all these quantities (see [32]), the ratio can be calculated to be 0.958 ± 0.030. The deviation from unity, although not yet significant, could indicate some new phenomena. However it could also be due to systematic errors in difficult measurements such as the tau lifetime.

Chapter 6

Theoretical Aspects of Tau Physics at LEP

The derivation of real physical predictions from the Standard Model, *e.g.* the calculation of a cross section, is in general a complex procedure, especially if higher order terms and renormalisation are involved. The determination of measurable quantities at LEP to the precision necessary for comparison with data lies mostly in the realm of the theorist. However, it is still important to know the basic structure of the standard model in order to understand the consequences of the theory in at least a qualitative way.

This chapter is an attempt to summarise the theory behind the analysis described in this thesis. Equations are quoted only at the simplest level with no allowance for higher order effects. These are often accounted for in analyses by the use of Monte Carlo event generators which include higher order corrections. This is usually true of QED radiative corrections. In the case of higher order electroweak correction, for the purposes of most calculations it is possible to absorb their effect into the lowest order equations by a simple replacement of the observable parameters by an effective value. For example, the weak mixing angle, $\sin^2\theta_W$, when observed in experiments becomes $\sin^2\overline{\theta}_W$, although the value of this effective weak mixing angle is only slightly different from the fundamental value. The underlying processes are not affected qualitatively, but the observed value of such parameters is altered slightly requiring this distinction.

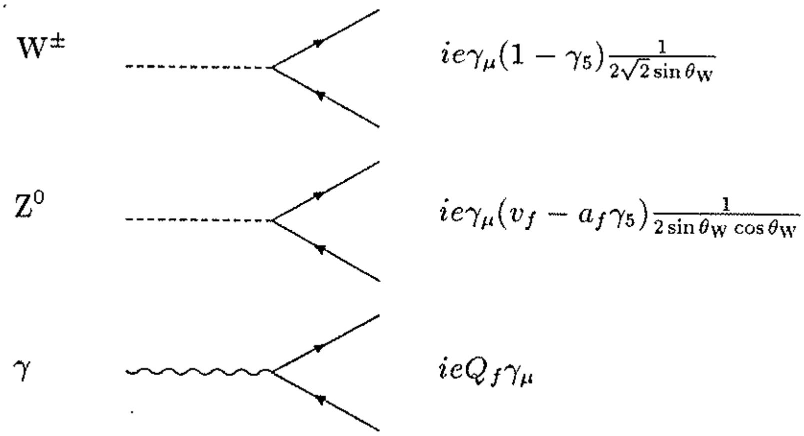

Figure 6.1: Coupling terms for electro-weak gauge bosons to fermions.

6.1 A Brief Summary of Boson Couplings in the Standard Model

The formalism of Quantum Field Theories is often not transparent when trying to interpret its predictions. In order to visualise the physical processes involved, the Feynman graph representation is used, associating various types of objects to the particle lines, and couplings to the vertices. It is by studying the form of the vertex couplings that some idea of the physical consequences can be formed, without having to work through the mathematics in detail.

The most important coupling terms in electro-weak theory are those of the four gauge bosons, γ, $W^{\pm}$ and Z^0, to the fermions. They are summarised in figure 6.1. The γ-matrices are those used in the Dirac equation formalism for relativistic particle mechanics and Q_f is the charge of the fermion. The $W^{\pm}$ coupling contains the term $(1-\gamma_5)$, which projects out the left-handed component of fermions (or right-handed for anti-fermions). It is this term that describes mathematically the 'V–A theory' of charged weak currents. That is the vector and axial couplings are of the same magnitude, but opposite sign. It produces the maximal parity violation observed in weak decays via the W boson by excluding any interaction with the right handed component of fermions. The photon coupling has no γ_5 term (it is said to be purely vector in nature) and so interacts equally with left-handed and right-handed fermions.

The Z^0 coupling has a more complex structure with both vector and axial coupling terms which depend on the value of θ_W. The standard model predicts the following relations:

$$v_f = I_3^f - 2Q_f \sin^2\theta_W, \qquad a_f = I_3^f$$

where I_3^f is the third component of weak isospin of the fermion, *i.e.* $\frac{1}{2}$ for neutrinos and u, c quarks and and $-\frac{1}{2}$ for charged leptons and d, s, b quarks. For charged leptons such as the tau, this means the vector coupling is far smaller than the axial coupling, since $\sin^2\theta_W$ is close to 0.25. Accurate measurement of this vector coupling can be used to determine $\sin^2\theta_W$ to high accuracy.

It is useful to re-express the Z^0 coupling in terms of couplings to left and right handed fermions. Ignoring constant factors,

$$\gamma_\mu(v_f - a_f\gamma_5) \equiv \frac{1}{2}(v_f - a_f)\gamma_\mu(1+\gamma_5) + \frac{1}{2}(v_f + a_f)\gamma_\mu(1-\gamma_5).$$

For a neutrino, $v_f - a_f$ becomes zero, predicting the expected non-interaction with right-handed neutrinos. However, the Z^0 does couple to both the right and left-handed components of a charged fermion. The couplings will be different, although the small value of v_f for charged leptons means that they are quantitatively similar. However, it does produce parity violating effects in Z^0 physics, such as the tau polarisation observed at LEP.

6.2 Tau Polarisation in $e^+e^- \to \tau^+\tau^-$ at LEP

The origin of polarisation in tau pair production at LEP is illustrated in figure 6.2. It is clear from the fact that the right-handed initial electron-positron pair have a coupling proportional to $v_e - a_e$ in this reaction that if the vector and axial coupling are of the same sign, these will couple less strongly to the Z^0. This means that the Z^0 itself has an average spin, depending on the electron couplings. Similar considerations in the decay to tau pairs mean that both the effect of the average Z^0 spin and the vector-axial couplings in the decay are observed in the helicities of the final products. By defining suitable quantities, the effect of the electron and tau couplings can be separated and measured independently.

In order to see this in detail it is necessary to look at the theory in detail. A summary of the relevant formulae is given below.

$$e^+e^- \to Z^0 \to \tau^+\tau^-$$

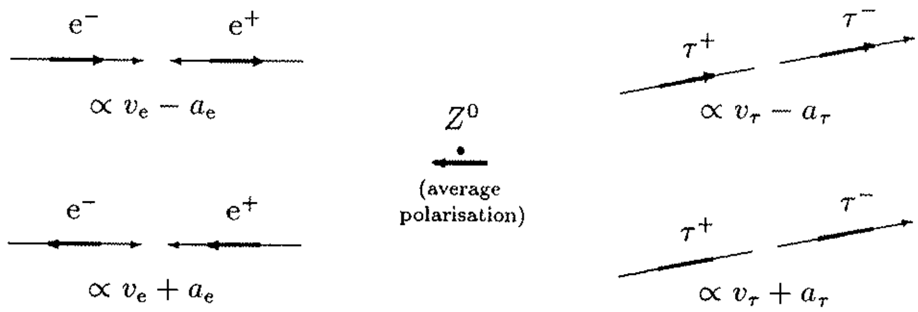

Figure 6.2: Illustration of $e^+e^- \to \tau^+\tau^-$ at LEP — thin lines represent momenta, thick lines particle spins.

6.2.1 Tau Pair Cross Section Formula

The full expression for the differential cross section of $e^+e^- \to \tau^+\tau^-$ as a function of the helicity (h, taking values ± 1) of the τ^- is as follows (see [8]):

$$\begin{aligned}\frac{d\sigma}{d\cos\theta}(s,\cos\theta;h) &= (1+\cos^2\theta)F_0(s) + 2\cos\theta F_1(s) \\ &- h\left[(1+\cos^2\theta)F_2(s) + 2\cos\theta F_3(s)\right].\end{aligned}$$

where s is the centre of mass energy squared. Theta in this case is the angle of the emerging τ^- relative to the initial direction of the incident electron. The four coefficients (F_0, F_1, F_2, F_3) are given by

$$\begin{aligned}F_0(s) &= \frac{\pi\alpha^2}{2s}\{1 + 2v_e v_\tau \mathrm{Re}\chi(s) + (v_e^2+a_e^2)(v_\tau^2+a_\tau^2)|\chi(s)|^2\}, \\ F_1(s) &= \frac{\pi\alpha^2}{2s}\{2a_e a_\tau \mathrm{Re}\chi(s) + 4v_e a_e v_\tau a_\tau|\chi(s)|^2\}, \\ F_2(s) &= \frac{\pi\alpha^2}{2s}\{2v_e a_\tau \mathrm{Re}\chi(s) + 2v_\tau a_\tau(v_e^2+a_e^2)|\chi(s)|^2\}, \\ F_3(s) &= \frac{\pi\alpha^2}{2s}\{2a_e v_\tau \mathrm{Re}\chi(s) + 2v_e a_e(v_\tau^2+a_\tau^2)|\chi(s)|^2\},\end{aligned}$$

with

$$\chi(s) = \frac{1}{4\sin^2\theta_W\cos^2\theta_W}\ \frac{s}{s - M_Z^2 + is\Gamma_Z/M_Z.}$$

The v_e, a_e, v_τ and a_τ are the vector and axial coupling constants for the electron and tau lepton.

6.2.2 Average Tau Polarisation

Addition of the above formulae over the two helicity states removes the F_2 and F_3 factors and recovers the normal Born cross section for the Z^0, from which the total cross section and charge forward-backward asymmetry can be derived. The average polarisation of the tau is found by integrating the two helicity states over $\cos\theta$ and averaging the totals weighted by the helicity, *i.e.*

$$< P_{\tau^-}(s) > = \frac{\sigma(h=1) - \sigma(h=-1)}{\sigma(h=1) + \sigma(h=-1)}.$$

If the angular cut-off is the same in the forward and backward direction, then the angular integration is simple. The F_1 and F_3 factors are odd in $\cos\theta$ and so these terms disappear. The other factors all have the same angular dependence, $(1+\cos^2\theta)$, and so integration over $\cos\theta$ yields a constant which cancels. Therefore the average polarisation becomes

$$\begin{aligned} < P_{\tau^-}(s) > &= \frac{(F_0(s) - F_2(s)) - (F_0(s) + F_2(s))}{(F_0(s) + F_2(s)) + (F_0(s) - F_2(s))} = -\frac{F_2(s)}{F_0(s)} \\ &= -\frac{2v_e a_\tau \mathrm{Re}\chi(s) + 2v_\tau a_\tau (v_e^2 + a_e^2)|\chi(s)|^2}{1 + 2v_e v_\tau \mathrm{Re}\chi(s) + (v_e^2 + a_e^2)(v_\tau^2 + a_\tau^2)|\chi(s)|^2}. \end{aligned}$$

Near the Z^0 energy, χ becomes very large with the imaginary component being dominant, and so the only $|\chi|^2$ terms are important. It is therefore possible to reduce the equation to

$$< P_{\tau^-} > \simeq -\frac{2v_\tau a_\tau}{(v_\tau^2 + a_\tau^2)}$$

and approximating again, using the fact that $v_\tau^2 \ll a_\tau^2$,

$$< P_{\tau^-} > \simeq -\frac{2v_\tau}{a_\tau}.$$

So a measurement of the average polarisation over any symmetrical angular range (*i.e.* same in forwards and backwards region) can be used to determine the ratio of vector and axial couplings of the tau lepton.

The fact that the final measurement is linear in the individual couplings contrasts with the standard forward-backward charge asymmetry measurement, which is quadratic in these terms. Thus the polarisation analysis can give the relative signs of the couplings, unlike the charge asymmetry measurement. Furthermore,

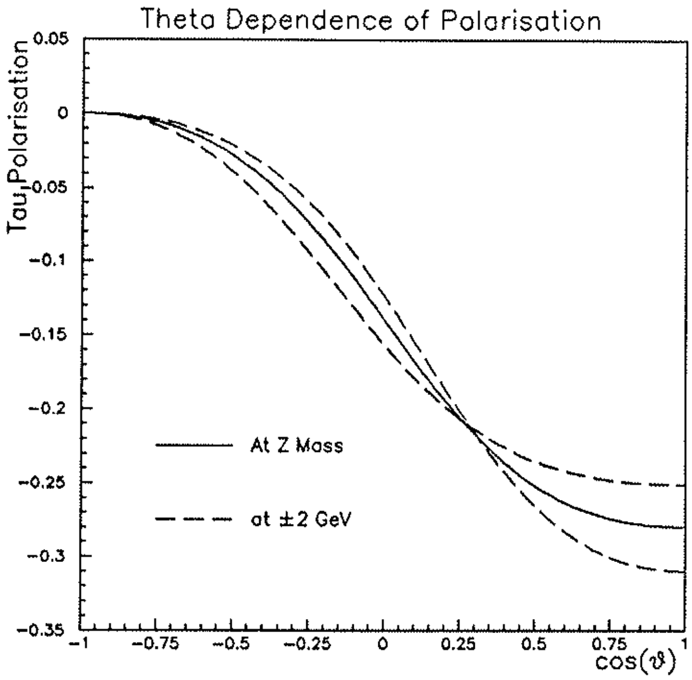

Figure 6.3: The polarisation of taus as a function of $\cos\theta$ shown at various centre of mass energies.

it is possible, using the expressions for the vector and axial couplings given in the previous section, to determine $\sin^2\theta_W$, since $\frac{v_f}{a_f}$ should be $1 - 4\sin^2\theta_W$, *i.e.*

$$<P_{\tau^-}> \simeq -2(1 - 4\sin^2\theta_W).$$

Of course measurements at LEP are taken over a range of centre of mass values around the Z^0 resonance. One of the attractive features of the tau polarisation measurement is that it is almost independent of the beam energy. This is shown in figure 6.3, where the theta dependence of the polarisation is plotted at three centre of mass energies. The fact that the polarisation is almost independent of beam energy suggest that it is also insensitive to initial state radiation. Note that at the Z^0 mass (solid line in figure), the dependence has rotational symmetry about the point corresponding to $\cos\theta = 0$, $P \sim -0.14$, *i.e.*

$$P(-\cos\theta) + 0.14 = -(\,P(\cos\theta) + 0.14\,).$$

This illustrates the fact that the average polarisation is independent of angular cut-off at the Z^0mass.

6.2.3 Forward-Backward Polarisation Asymmetry

The theta dependence of the polarisation shown in figure 6.3 motivates a measurement of this dependence. With the statistics currently available, the easiest way to do this is to split the angular range into two regions — forwards ($\cos\theta > 0$) and backwards ($\cos\theta < 0$). The average polarisation in these two ranges can be measured.

It helps to define the polarisation as a function of $\cos\theta$. That is the average polarisation of events with the τ^- produced at an angle θ, *i.e.*

$$\begin{aligned} P_{\tau^-}(\cos\theta) &= \frac{\frac{d\sigma}{d\cos\theta}(h=1) - \frac{d\sigma}{d\cos\theta}(h=-1)}{\frac{d\sigma}{d\cos\theta}(h=1) + \frac{d\sigma}{d\cos\theta}(h=-1)} \\ &= -\frac{(1+\cos^2\theta)F_2 + 2\cos\theta F_3}{(1+\cos^2\theta)F_0 + 2\cos\theta F_1}, \end{aligned}$$

from the differential cross section formulae. For brevity, it is useful to denote the denominator of this expression by $\frac{d\sigma_{\mathrm{Born}}}{d\cos\theta}$, since it corresponds to the standard Born differential cross section. Therefore it is possible to write

$$P_{\tau^-}(\cos\theta)\,\frac{d\sigma_{\mathrm{Born}}}{d\cos\theta} = -(1+\cos^2\theta)F_2 + 2\cos\theta F_3,$$

which is used later.

Unlike the average polarisation in the previous section, the forward backward polarisation asymmetry *does* depend on the angular cut-off applied. If this cut-off in the forward region corresponds to $\cos\theta = z_0$ (and $\cos\theta = -z_0$ in the backward region), then the average polarisations are defined by:

$$\begin{aligned} <P_{\tau^-}>_F &\equiv \frac{\int_0^{z_0} \mathrm{d}\cos\theta\, P_{\tau^-} \frac{d\sigma_{\mathrm{Born}}}{\mathrm{d}\cos\theta}}{\int_0^{z_0} \mathrm{d}\cos\theta\, \frac{d\sigma_{\mathrm{Born}}}{\mathrm{d}\cos\theta}} \\ <P_{\tau^-}>_B &\equiv \frac{\int_{-z_0}^{0} \mathrm{d}\cos\theta\, P_{\tau^-} \frac{d\sigma_{\mathrm{Born}}}{\mathrm{d}\cos\theta}}{\int_{-z_0}^{0} \mathrm{d}\cos\theta\, \frac{d\sigma_{\mathrm{Born}}}{\mathrm{d}\cos\theta}} \end{aligned}$$

The polarisation asymmetry is then defined as:

$$\begin{aligned} A_{\mathrm{FB}}^{\tau^-\mathrm{pol}} &\equiv \frac{\int_0^{z_0} \mathrm{d}\cos\theta\, P_{\tau^-} \frac{d\sigma_{\mathrm{Born}}}{\mathrm{d}\cos\theta} - \int_{-z_0}^{0} \mathrm{d}\cos\theta\, P_{\tau^-} \frac{d\sigma_{\mathrm{Born}}}{\mathrm{d}\cos\theta}}{\int_{-z_0}^{z_0} \mathrm{d}\cos\theta\, \frac{d\sigma_{\mathrm{Born}}}{\mathrm{d}\cos\theta}} \\ &= -\frac{\int_0^{z_0} \mathrm{d}\cos\theta[(1+\cos^2\theta)F_2 + 2\cos\theta F_3] - \int_{-z_0}^{0} \mathrm{d}\cos\theta[(1+\cos^2\theta)F_2 + 2\cos\theta F_3]}{\int_{-z_0}^{z_0} \mathrm{d}\cos\theta\,[(1+\cos^2\theta)F_0 + 2\cos\theta F_1]} \\ &= -\frac{\int_0^{z_0} \mathrm{d}\cos\theta\, 2\cos\theta\, F_3}{\int_0^{z_0} \mathrm{d}\cos\theta\,(1+\cos^2\theta)\,F_0} = -\frac{z_0}{1+\frac{z_0^2}{3}}\,\frac{F_3}{F_0}. \end{aligned}$$

The cancelation of terms before the integration stage in this calculation is possible because of the odd or even nature of the relevant functions. Using a similar approximation to that used when calculating the average polarisation (using the large value of $|\chi|^2$), this final expression becomes

$$A_{\mathrm{FB}}^{\tau^- \mathrm{pol}} \simeq -\frac{z_0}{1+\frac{z_0^2}{3}} \frac{2v_e a_e}{(v_e^2+a_e^2)}.$$

The factor introduced by the angular cut-off, z_0, has a maximum value of $\frac{3}{4}$ for full acceptance.

Experimentally the asymmetry is defined by:

$$A_{\mathrm{FB}}^{\tau^- \mathrm{pol}} = \frac{< P_{\tau^-} >_F .n_F \;-\; < P_{\tau^-} >_B .n_B}{n_F \;+\; n_B} \;,$$

where n_F and n_B are the number of events with the τ^- particle in the forward and backward hemispheres.

Thus the polarisation asymmetry can be used to relate the electron coupling constants in the same way that the average polarisation was used for the tau lepton. Another determination of $\sin^2\theta_{\mathrm{W}}$ is also possible, and if lepton universality is assumed, better accuracy is possible for both measurements.

6.3 Tau Decay

In order to obtain measurements of polarisation in $e^+e^- \rightarrow \tau^+\tau^-$ it is necessary to study the decay of the tau particles. Some of the predictions of the standard model relating to tau polarisation are presented below, but first a summary of the basic process is given as background to the branching ratio analysis of the previous chapter.

6.3.1 Decay Rate and Branching Ratios

One of the easiest weak interaction processes to model theoretically is the decay of the muon. It was one of the first reactions to be understood in terms of the V-A nature of charged weak currents. Tau decay is a fairly simple extension of the same reaction, the only difference being that the tau is heavier and therefore it has more possible final states. One consequence of this is that the tau can decay to quarks, whereas the muon decay is purely leptonic. Unfortunately, the hadronic decays necessitate the use of QCD in the full tau decay analysis, which is less precisely understood than the purely weak processes.

The purely leptonic process $\mu \rightarrow e\overline{\nu}_e\nu_\mu$ is predicted to have a decay rate given by

$$\Gamma = \frac{1}{\tau} = \frac{G_\mu^2 m_\mu^5}{192\pi^3},$$

where τ is the lifetime, G_μ is the Fermi coupling constant for the muon and m_μ is the mass of the muon. Now considering the process $\tau \rightarrow e\overline{\nu}_e\nu_\tau$, the partial decay rate for this decay of the tau should be given by the same formula with the replacement of the mass and Fermi coupling constant by those relevant to the tau. If universality is assumed (*i.e.* $G_\tau = G_\mu$), that means

$$\Gamma(\tau \rightarrow e\overline{\nu}_e\nu_\tau) = \Gamma(\mu \rightarrow e\overline{\nu}_e\nu_\mu) \times \left(\frac{m_\tau}{m_\mu}\right)^5.$$

The same formula can again be applied to the $\tau \rightarrow \mu\overline{\nu}_\mu\nu_\tau$ decay, except in this case the mass of the products are non-negligible, introducing a small phase space factor. Thus the decay rate of a tau to muons is slightly less that that to electrons. The other decays of the tau involve a coupling of the virtual W to a quark-antiquark pair of the lowest mass doublet. Colour degeneracy suggests that the rate for this process should be approximately three times that of the $\tau \rightarrow e\overline{\nu}_e\nu_\tau$ decay. However, as stated before, the QCD nature of these decays becomes important, and higher order QCD corrections are not negligible. In fact it turns out that

$$\Gamma(\tau \rightarrow \text{hadrons}) \simeq 3.5 \times \Gamma(\tau \rightarrow e\overline{\nu}_e\nu_\tau).$$

The branching ratio for a tau decay is defined as the ratio of its partial decay rate to that of the total tau decay rate, *i.e.*

$$\mathrm{B}(\tau \rightarrow \mu\overline{\nu}_\mu\nu_\tau) = \frac{\Gamma(\tau \rightarrow \mu\overline{\nu}_\mu\nu_\tau)}{\Gamma(\tau \rightarrow e\overline{\nu}_e\nu_\tau) + \Gamma(\tau \rightarrow \mu\overline{\nu}_\mu\nu_\tau) + \Gamma(\tau \rightarrow \text{hadrons})}.$$

Branching ratios can be measured precisely at LEP as can the tau lifetime, all of which can be used to test the above predictions.

Another aspect of branching ratio measurements is the determination of 'topological branching ratios'. This arises from the distinctive decay of the tau into one, three or five charged particles, which are observed as jets containing one, three or five tracks. This gives rise to the terms used to describe $e^+e^- \to \tau^+\tau^-$ events as having, for example, 1-1, 1-3 and 1-5 topologies, as, in these examples, one tau decays to one charged particle, and the other to one or more. Measurements of the ratios of these types of events leads to branching ratios for tau to each possibility for number of charged particles. These are called the topological branching ratios.

6.3.2 The Use of Tau Decays to Analyse Polarisation

The decay of the tau via the W boson, with the consequent maximal parity violation, means that the decay products still contain information about the spin of the tau before the decay. This is manifested in their momentum spectra, and it is these momentum spectra that can be analysed to measure the polarisation of the $e^+e^- \to \tau^+\tau^-$ events. Note that polarisation of the tau pairs is defined as the helicity of the τ^-.

Pion Momentum Spectrum in Tau Decays

The simplest example of this technique is the pion momentum spectrum in $\tau \to \pi\nu_\tau$ decays, since it is only a two body decay, and the pion has zero spin. Consider this decay mode for a decaying relativistic τ^- with positive helicity. In the relativistic limit, the spin component along the axis of travel is entirely quantised in the direction of travel. The mass of the tau (about 1.8 GeV) is small enough compared to LEP energies that it can in general be ignored. When the τ^- decays, in the centre of mass frame, the neutrino and pion must emerge back-to-back. The only decay product with spin is the neutrino, and so decay with neutrino spin aligned with tau spin will be favoured (see figure 6.4). Since the neutrino is left-handed, it will prefer to emerge with momentum opposite to the tau spin, and conversely the π^- will tend to emerge with momentum in the direction of the tau spin. Since this is also the direction of travel, when the system is boosted back to the experimental frame, the pion momentum will be hardened.

To quantify this, quantum mechanics predicts that the pion momentum in the

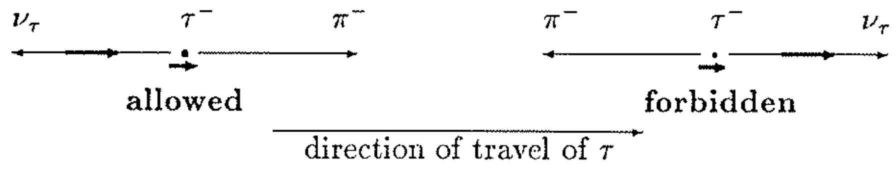

Momentum of ν_τ and π^- $= p$
Total energy of system $= m_\tau$
Energy of π^- $= m_\tau - p$

Figure 6.4: An illustration of $\tau \to \pi\nu_\tau$ decay in the centre of mass frame.

rest frame will have a distribution given by

$$\frac{1}{N}\frac{dN}{d\cos\theta} = \frac{1}{2}(1+\cos\theta),$$

where θ is the angle between the pion momentum and the spin axis of the tau — which is also the axis of the Lorentz boost.

The pion is emitted with a momentum, p, given by

$$(m_\tau - p)^2 = m_\pi^2 + p^2 \quad \Longrightarrow \quad p = \frac{m_\tau^2 - m_\pi^2}{2\,m_\tau},$$

where m_τ and m_π are the masses of the tau and pion respectively. In the experimental frame of reference, the tau particle is travelling with a Lorentz boost of $\gamma = E_{\text{beam}}/m_\tau$. Applying this boost to the pion decay product gives the equation

$$E_\pi = \gamma(m_\tau - p) + \beta\gamma\, p\cos\theta,$$

where E_π is the energy of the pion in the boosted frame of reference. Note that $\beta\gamma = 1/m_\tau\sqrt{E_{\text{beam}}^2 - m_\tau^2}$. The above equation can be rearranged to give the value of $\cos\theta$ as

$$\begin{aligned}\cos\theta &= \frac{2E_\pi m_\tau^2 - \gamma m_\tau(2m_\tau^2 - 2pm_\tau)}{2pm_\tau \quad m_\tau\beta\gamma} \\ &= \frac{2E_\pi m_\tau^2 - E_{\text{beam}}(m_\tau^2 + m_\pi^2)}{(m_\tau^2 - m_\pi^2)\sqrt{E_{\text{beam}}^2 - m_\tau^2}}\end{aligned}$$

and using $E_{\text{beam}}^2 \gg m_\tau^2$, $m_\tau^2 \gg m_\pi^2$, this reduces to

$$\cos\theta \simeq 2x_\pi - 1 \quad , \quad x_\pi = \frac{E_\pi}{E_{\text{beam}}}.$$

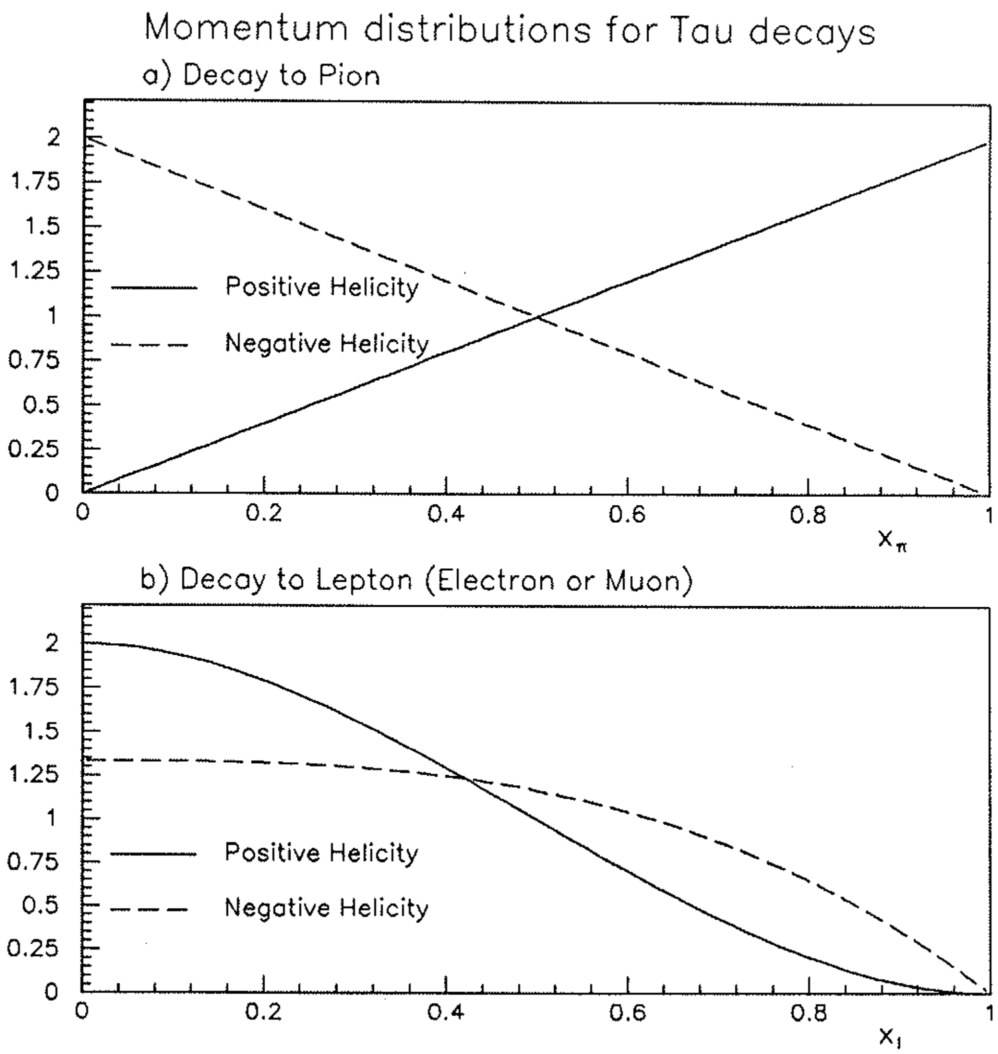

Figure 6.5: Momentum spectra for charged decay products of a boosted τ^- particle decaying to a) pion b) lepton.

Therefore, in the laboratory frame, we have a pion momentum spectrum given by:

$$\frac{1}{N}\frac{dN}{dx_\pi} = 2x_\pi.$$

It should be clear that a τ^+ with negative helicity decaying to a π^+ will have the same momentum distribution (consider a CP inversion). In fact this is exactly the case for $e^+e^- \to \tau^+\tau^-$ interactions when the τ^- has positive helicity as demanded above. The spin-1 assignment of the Z^0 means that the two tau particles must have opposite helicities. So if *both* of the tau particles decay by $\tau \to \pi\nu_\tau$, then the momentum spectra of the two pions will be the same.

Alternatively, the helicities of the two tau particles could *both* be reversed. Again the momentum spectra of the pions would be the same as each other, but different to that given above. The angular distribution in the rest frame is now proportional to $1 - \cos\theta$, meaning that the pion momentum spectrum is now proportional to $2(1 - x_\pi)$. The two momentum spectra are illustrated in figure 6.5(a). It is obvious that the $\tau \rightarrow \pi\nu_\tau$ is a very effective polarisation analyser since the two spectra are very different.

Leptonic Momentum Spectrum in Tau Decays

Very similar considerations apply to $\tau \rightarrow e\overline{\nu}_e\nu_\tau$ and $\tau \rightarrow \mu\overline{\nu}_\mu\nu_\tau$ decays. It is still true that if the two taus from an $e^+e^- \rightarrow \tau^+\tau^-$ interaction both decay this way, then the momentum spectra of the two charged leptons will be the same. However, the leptonic decays involve two neutrinos instead of the one in $\tau \rightarrow \pi\nu_\tau$ and all three decay products have spin. This means that although the spectra still contain some polarisation information, they are less sensitive to polarisation.

The decay mechanics in this case are far more complicated, so only the final result from the literature is shown here (see for example [8]). The momentum spectrum is described in terms x_l — the momentum of the lepton as a fraction of beam energy. The spectrum for the decay of a τ^- is

$$\frac{1}{N}\frac{dN}{dx_l} \simeq f(x_l) + h\,g(x_l),$$

the helicity, h, being ± 1. The functions $f(x)$ and $g(x)$ are defined by

$$\begin{aligned} f(x) &= \frac{1}{3}(5 - 9x^2 + 4x^3), \\ g(x) &= \frac{1}{3}(1 - 9x^2 + 8x^3). \end{aligned}$$

These momentum distributions can be more easily understood with reference to figure 6.5(b). The two distributions are not very different, which indicates that they have a fairly poor sensitivity to polarisation in comparison to tau decays to pions. However, larger statistics are available in both the $\tau \rightarrow e\overline{\nu}_e\nu_\tau$ and $\tau \rightarrow \mu\overline{\nu}_\mu\nu_\tau$ channels, and so investigations of polarisation in these events are still important.

Chapter 7

Tau Polarisation Studies

The reaction $e^+e^- \rightarrow \tau^+\tau^-$ is unique amongst the leptonic decays of the Z^0 seen at LEP in that the tau particles themselves decay within the confines of the detector. The lifetime and Lorentz boost of the muon mean that it would be very unlikely to observe a muon decay. Therefore in the case of the electron and muon, only the cross-section and angular distribution can be measured, but the decay of the tau (with a typical decay length of 50 μm at LEP energies) opens up new physics analysis possibilities. Not only can the branching ratios be measured, but also the decay products give information on the spin of the tau which can be used to determine the vector and axial coupling of leptons and as a further test of the standard model.

The average polarisation of taus is dependent on $\cos\theta$ and peaked in the forward direction (*i.e.* low θ), so it is useful to attempt to analyse events where possible in the high $\cos\theta$ range. This chapter presents the results of such an analysis performed on the sample of $\tau \rightarrow \mu\bar{\nu}_\mu\nu_\tau$ candidates described in chapter 5, and then a further analysis of correlation of polarisation between the τ^+ and τ^- particles in the reaction $e^+e^- \rightarrow \tau^+\tau^-$.

7.1 Tau Polarisation in $\tau \rightarrow \mu\bar{\nu}_\mu\nu_\tau$ Events

The decay of the tau to muon is a three body decay involving two massless neutrinos. Since the two neutrinos are not detected, only the muon can be used to give information on the tau polarisation. This is done by an analysis of the momentum spectrum of the muons, including, if statistics allow, a separation into different angular ranges in order to study the dependence on $\cos\theta$. The variable used to describe the momentum spectrum of a muon is the momentum as a fraction of beam energy x_μ as defined in section 5.2.1, *i.e.*

$$x_\mu = \frac{p_{\mathrm{trk}} + E_{\mathrm{cls}} - 0.5\ \mathrm{GeV}}{E_{\mathrm{beam}}}.$$

This is used in order to include energy from radiative photons in the region of the tau which simplifies the adjustments needed for radiative corrections.

7.1.1 Correction of the Momentum Spectrum

Before finding the polarisation, the momentum spectrum must be corrected for various detector and other effects. These are described below for the measurement of the average polarisation of all $\tau \to \mu\overline{\nu}_\mu\nu_\tau$ candidates.

Correction for Background

The original muon momentum spectrum obtained from the 1295 $\tau \to \mu\overline{\nu}_\mu\nu_\tau$ candidates of chapter 5 is shown in figure 7.1(a). The shaded region shows the scaled background estimated from Monte Carlo tau and non-tau events which forms about 4% of the candidate events. This background is simply subtracted from the data, with the errors on each bin being suitably adjusted.

Correction for Momentum Smearing

The events in the spectrum with a value above $x_\mu = 1$ come mostly from mismeasured high momentum muons where the track has been assigned a momentum higher than beam energy. The smearing of momenta by the central detector also occurs to a lesser extent at lower momenta, and would allow events to migrate between bins of the spectrum. To allow for this, the effect of mismeasurement was studied in the Monte Carlo simulation over the whole range of momenta. From this a migration matrix can be built up giving the probability of a track moving between bins due to this effect.

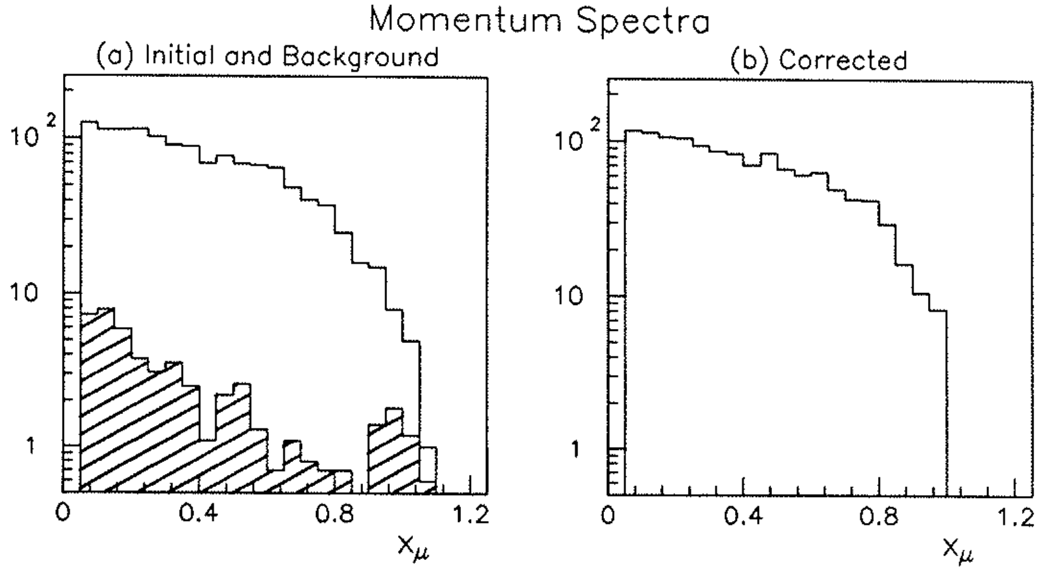

Figure 7.1: Momentum spectra for $\tau \rightarrow \mu\overline{\nu}_\mu\nu_\tau$ candidates (a) before corrections (b) after all corrections.

The calculation is performed by finding the probability that an event included (after reconstruction) in one bin, actually belongs to another. Then the momentum spectrum after background subtraction is simply multiplied by this correction matrix to produce the most likely original spectrum. The correction necessary for this effect is fairly small due to the good momentum resolution of the tracking chambers, but it at least removes the problem of events with $x_\mu > 1$.

Correction for Efficiency

The efficiency of the $\tau \rightarrow \mu\overline{\nu}_\mu\nu_\tau$ selection varies with momentum. There is an explicit lower limit of 0.05 on the value of the fractional momentum in the selection procedure, so the analysis can only go down to this value, and at the upper momentum range the efficiency decreases slightly, as the higher energy muons are more likely to be excluded by muon pair cuts. An estimation of the efficiency at different momentum ranges can be obtained from Monte Carlo events, and the results checked by comparison with both muon pair events and two photon $e^+e^- \rightarrow \mu^+\mu^-e^+e^-$ events. The momentum distribution is then corrected bin by bin for the variation in efficiency. The factor applied to each bin is shown in figure 7.2(a), where the normalisation of the correction factor is chosen to maintain

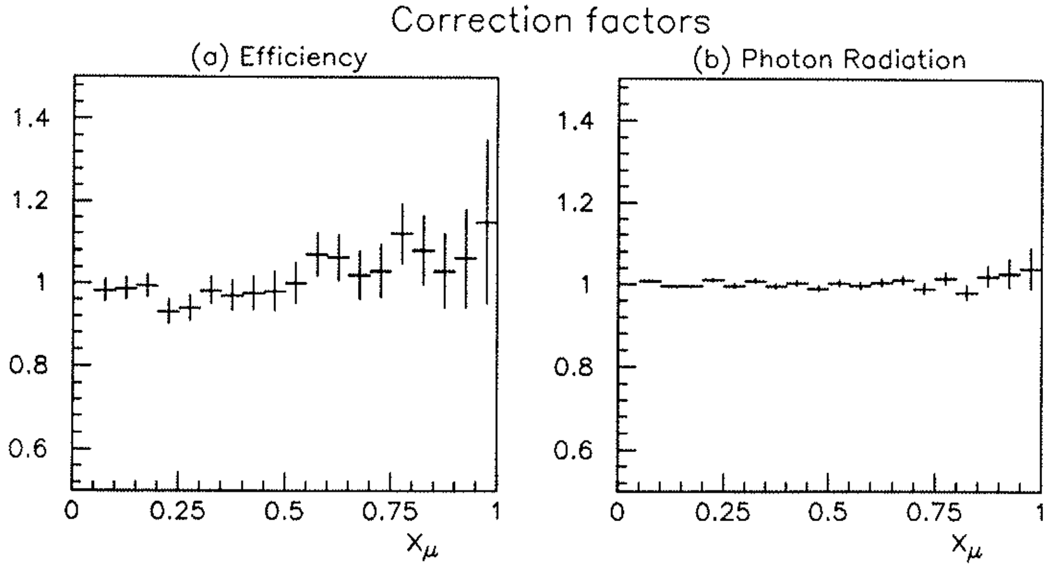

Figure 7.2: Bin by bin correction factors for the $\tau \rightarrow \mu\overline{\nu}_\mu\nu_\tau$ momentum spectrum — corrections for (a) efficiency (b) radiative effects.

the same number of events.

Correction for Radiative Effects

The effect of photon radiation on the measured spectrum is estimated from the Monte Carlo by a study of four-vectors. Initial and final state radiation as well as radiative corrections to the tau decay itself can distort the momentum distribution. Equal numbers of events are generated with and without these effects and the results compared. Since the momentum measured includes energy in a 35^o cone around the charged track, the momentum spectrum is in fact changed very little, since most radiative photons will be included. In fact, there is only a slight indication that the higher end of the spectrum is affected, as shown in figure 7.2(b), and even this is not statistically significant.

7.1.2 Measurement of Average Tau Polarisation

The corrected momentum spectrum, with errors added in quadrature for each bin, was fitted using a simple χ^2 minimisation to the distribution

$$\phi(x) = N\left[\frac{1}{3}(5 - 9x^2 + 4x^3) + <P_\tau> \times \frac{1}{3}(1 - 9x^2 + 8x^3)\right],$$

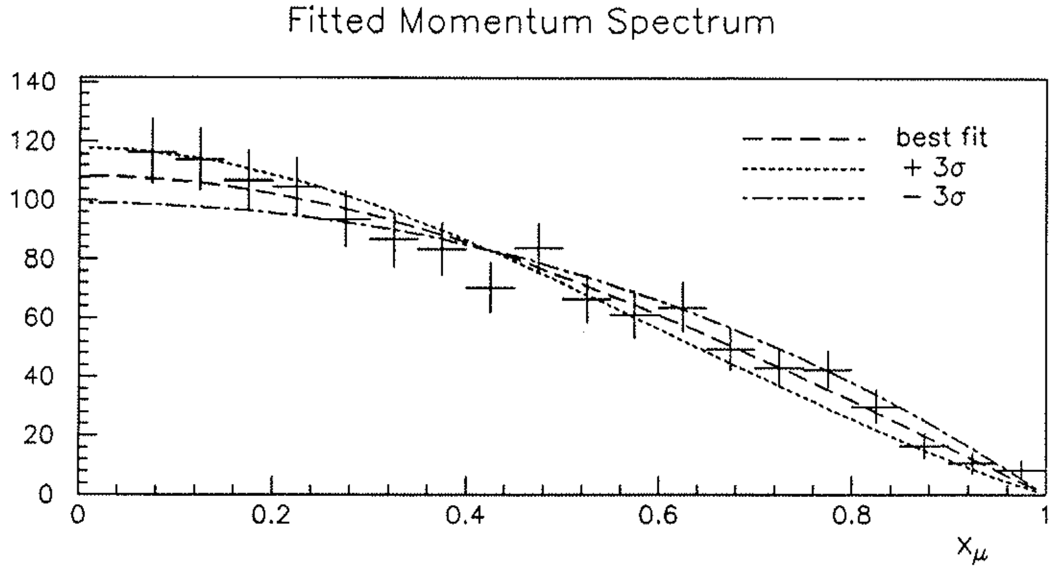

Figure 7.3: Momentum distribution after corrections with best fit curve and curves for $\pm 3\sigma$ on the polarisation.

which is derived from the functions in section 6.3.2. The parameters N, the normalisation, and $< P_\tau >$, the average tau polarisation, are left as free parameters.

This fit gives a value for $< P_\tau >$ of $-0.20 \pm 0.14(stat)$ with a χ^2 per degree of freedom of 0.82. The fitted distribution is shown in figure 7.3, with the equivalent momentum distributions using a polarisation at $\pm 3\sigma$ shown for comparison.

Systematic errors are calculated in a similar way to those of the branching ratio, *i.e.* by a study of the change in the fitted value on variation of the selection parameters. The result of this analysis is that the systematic errors are of the order ± 0.11. In this case however, there are also smaller systematic errors introduced by the spectrum correction process described above. These have been analysed elsewhere (see [34]), and the combined error for the polarisation measurement is a systematic error of ± 0.13.

7.1.3 Measurement of the Forward Backward Polarisation Asymmetry

For the purposes of forward-backward assignment of jets, the following scheme was used to define the charge of jets:

- the charge of each cone is the sum of the charges of the good tracks contained.
- if the two opposite jets are assigned the same charge in this way then:
    1. for 1–1 topologies, the sign of the lower momentum track is assumed to be correct.
    2. for 1–N topologies, the 1 prong decay is used.

This technique gives a very low probability of misassignment (less than 1% over the whole angular range) which forms a negligible contribution to the error.

The 1295 $\tau \to \mu\overline{\nu}_\mu\nu_\tau$ events divide into 665 forward (forward, as described in the previous chapter, τ^- at $\cos\theta > 0$, with standard θ definition) and 630 backward events. The momentum spectra in the forward and backward regions can be analysed for average polarisation using the same methods as for the whole sample. The same corrections and fitting techniques were applied to the two data sets, and the following results obtained:

$$\begin{aligned} <P_{\tau^-}>_{\mathrm{F}} &= -0.29 \pm 0.19(stat) \pm 0.14(sys) \\ <P_{\tau^-}>_{\mathrm{B}} &= -0.05 \pm 0.18(stat) \pm 0.14(sys) \end{aligned}$$

The systematic errors were again calculated by the variation of cut variables. The momentum spectra and the curves of best fit are shown in figure 7.4.

The forward-backward polarisation asymmetry as defined in the previous chapter can then be calculated.

$$\begin{aligned} A_{\mathrm{FB}}^{\tau^-\mathrm{pol}} &= \frac{<P_{\tau^-}>_{\mathrm{F}}.n_{\mathrm{F}} - <P_{\tau^-}>_{\mathrm{B}}.n_{\mathrm{B}}}{n_{\mathrm{F}} + n_{\mathrm{B}}} \\ &= -0.13 \pm 0.14(stat) \pm 0.11(sys) \end{aligned}$$

7.1.4 Calculation of Standard Model Parameters

Using the approximations presented in the previous chapter, the above results can be used to calculate values for $\sin^2\overline{\theta}_{\mathrm{W}}$ and the axial and vector couplings of the leptons involved. The average polarisation is given by

$$<P_{\tau^-}> \simeq -\frac{2v_\tau}{a_\tau} = -2(1 - 4\sin^2\overline{\theta}_{\mathrm{W}}).$$

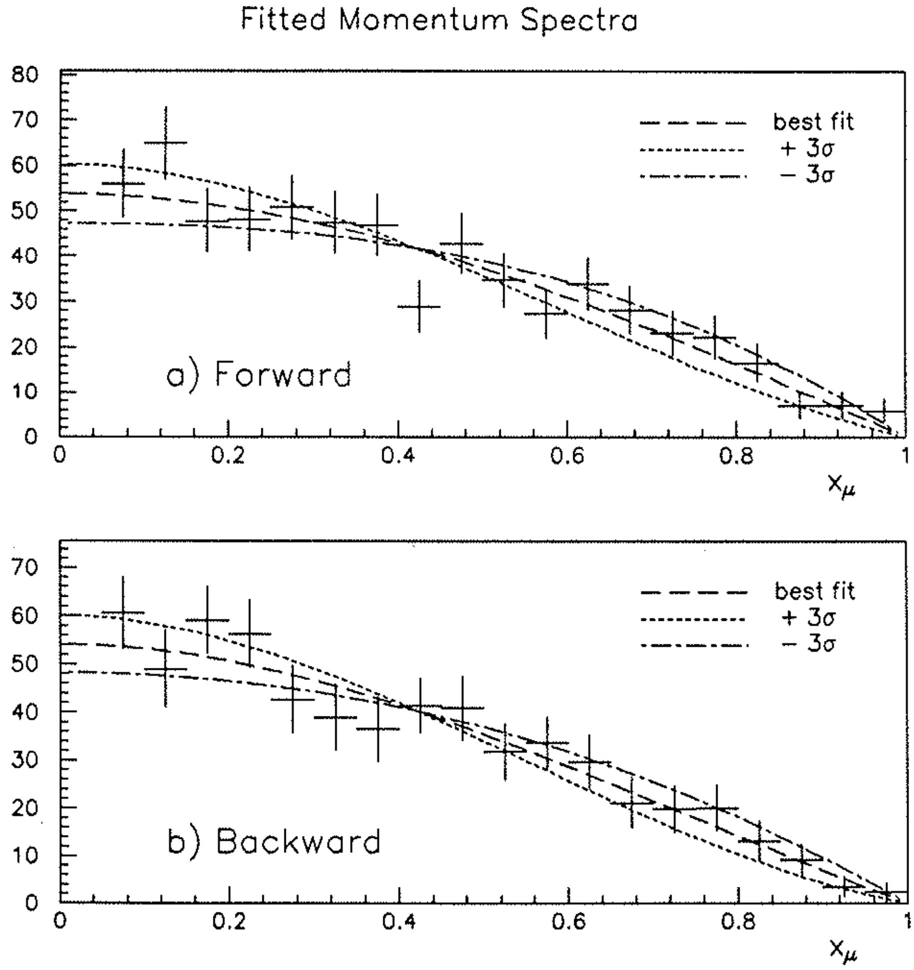

Figure 7.4: Momentum distribution with best fit and $\pm 3\sigma$ curves for (a) Forward and (b) Backward events.

Using the value found above,

$$< P_{\tau^-} > = -0.20 \pm 0.14(stat) \pm 0.13(sys),$$

the calculation leads to

$$\begin{aligned}\frac{v_\tau}{a_\tau} &= 0.10 \pm 0.07 \pm 0.06 \\ \sin^2\overline{\theta}_{\rm W} &= 0.22 \pm 0.02 \pm 0.02.\end{aligned}$$

The measurement of the forward-backward polarisation asymmetry isolates the vector and axial couplings of the electron, and their ratio can be used in a similar way to determine $\sin^2\overline{\theta}_{\rm W}$. In this case, the value for the asymmetry also depends on the angular cut off used in the analysis:

$$A_{\rm FB}^{\tau-\rm pol} \simeq -2F(z_0)\frac{v_{\rm e}}{a_{\rm e}} = -2F(z_0)(1 - 4\sin^2\overline{\theta}_{\rm W}),$$
$$\text{where} \qquad F(z_0) = \frac{z_0}{1 + \frac{z_0^2}{3}}$$

The parameter z_0 is the angular cutoff of the analysis in terms of $\cos\theta$ *i.e.* in this case $z_0 = 0.9$. Again, using the values found in the analysis, the results obtained are:

$$\begin{aligned}\frac{v_{\rm e}}{a_{\rm e}} &= 0.09 \pm 0.10 \pm 0.08 \\ \sin^2\overline{\theta}_{\rm W} &= 0.23 \pm 0.03 \pm 0.03.\end{aligned}$$

These results are consistent with the standard model and other measurements of the same quantities. However, with the statistics available they are not very significant. The $\sin^2\overline{\theta}_{\rm W}$ measurement is made far more accurately from Z^0 lineshape studies, and the ratio of vector and axial couplings can only be said to favour being positive, and does not exclude a negative or zero value.

In order to obtain results with more significance, it is possible to combine results from different decays of the tau particle. The $\tau \to \pi\nu_\tau$ decays are particularly sensitive to polarisation, and $\tau \to e\overline{\nu}_e\nu_\tau$ events are similar to $\tau \to \mu\overline{\nu}_\mu\nu_\tau$ in being common and easy to identify. In fact more complex decays of the tau can also be used but tend to have larger systematic errors. OPAL has published results combining the three channels mentioned above to obtain the following results [25]:

$$\begin{aligned}\frac{v}{a} &= 0.05 \pm 0.04 \\ \sin^2\overline{\theta}_W &= 0.238 \pm 0.009,\end{aligned}$$

assuming lepton universality, the errors being combined statistical and systematic. This then forms a determination of $\sin^2\overline{\theta}_W$ which is entirely independent from the lineshape studies, and confirms its value. Further statistics and refinements in the area of tau polarisation in the future will give a value for the weak mixing angle competitive with lineshape analyses — the OPAL value over a similar data taking period was $\sin^2\overline{\theta}_W = 0.2337 \pm 0.0021$ from the lineshape. Also better determinations of the lepton couplings including a further test of lepton universality will be possible.

7.2 Polarisation Correlations in Tau Decays

Another interesting aspect of the tau decay in the $e^+e^- \to \tau^+\tau^-$ reaction is that the polarisation of both taus can be investigated, and quantum mechanical predictions of the correlations of spins in the τ^- and τ^+ can be tested. In fact, with high statistics, it is possible to treat the emerging tau particles as a fundamental test of the interpretation of quantum mechanics by constructing observables which are sensitive to differences between probabilistic quantum mechanics and hidden variable theories (similar to Bell's Inequality — see [35]). This is not possible at the level of statistics currently available, but some basic correlations can still be observed.

7.2.1 A Simple Example of Polarisation Correlation

The polarisation correlation is most easily seen in events where both tau particles decay to a pion. From the decay of the Z^0 it is expected that the taus will be correlated in such a way that when the τ^- has positive (negative) helicity, the τ^+ will have negative (positive) helicity. That means that the decays are symmetric under CP inversion, and so the expected momentum spectrum of the two pions will be the same.

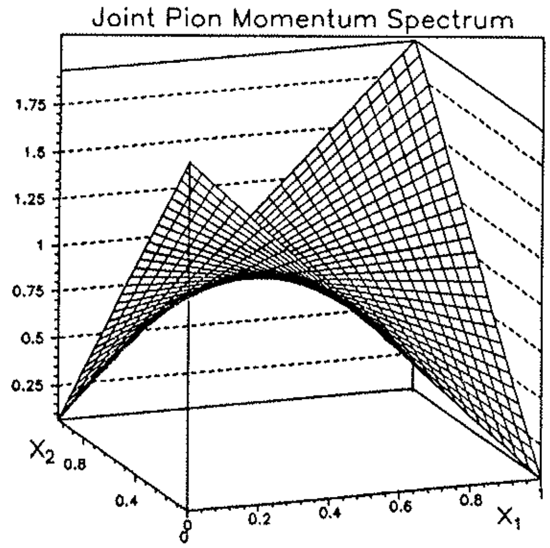

Figure 7.5: Joint pion momentum distribution in $e^+e^- \to \tau^+\tau^- \to \pi^+\overline{\nu}_\tau\pi^-\nu_\tau$ events assuming zero average polarisation.

Using momentum as a fraction of beam energy in all cases, if the π^- has momentum x_1 and the π^+ has momentum x_2, then the momentum spectra will be either

$$N(x_1) \propto 2x_1 \qquad \text{AND} \qquad N(x_2) \propto 2x_2$$

or

$$N(x_1) \propto 2(1-x_1) \qquad \text{AND} \qquad N(x_2) \propto 2(1-x_2).$$

Since there is predicted to be an average polarisation for the tau pairs, these two alternatives will not be observed equally, but for simplicity, assuming they are equally probable, the joint momentum spectrum for the two pions would be

$$\begin{aligned} N(x_1, x_2) &\propto \frac{1}{2}\left[2x_1 2x_2 + 2(1-x_1)2(1-x_2)\right] \\ &\propto 1 + (2x_1 - 1)(2x_2 - 1), \end{aligned}$$

which is shown in figure 7.5. If there were no correlation, this joint distribution would be flat.

Since the statistics available are too low to be able to fit to a double distribution, it is necessary to define a single variable to match to the data. The obvious candidate for this is the probability of an event to have occurred given that the tau particles had the predicted opposite helicities. So for an event with pions having momenta x_1, x_2, this probability will be

$$P(\text{same polarisation}) = x_1 x_2 + (1 - x_1)(1 - x_2).$$

Looking at the distribution of this variable over many events, it is seen that there is a clear difference between the cases when the helicities are opposite (as expected), the same or uncorrelated (see 7.6(a)). Uncorrelated spins give a distribution for the probability which is symmetrical about 0.5 (the dotted line in the graph). However, it is expected that if the taus had opposite helicities, the shape of the graph shifts upwards so the average is above 0.5 (the solid line). Similarly, if the taus are generated with the same helicity, the pion momenta would imply that the mean value of the distribution drops below 0.5. This change in the distribution would be easy to fit with perhaps a few tens of $e^+e^- \rightarrow \tau^+\tau^- \rightarrow \pi^+\overline{\nu}_\tau\pi^-\nu_\tau$ events.

7.2.2 Including other Decay Modes

The advantage of using the above method to determine correlation is that it is easy to include other decay modes with sensitivity to polarisation. The probability of any one decay coming from a τ^- of, say, positive helicity is just as easy to define for a leptonic decay as for a pion decay. Unfortunately, the leptonic decays are not so sensitive, as the probabilities themselves show. For a π^- of fractional momentum x, the probability of having been the decay product of a τ^- with positive helicity would be simply x. For a muon or electron, the probability is

$$\frac{3(1 - 3x^2 + 2x^3)}{5 - 9x^2 + 4x^3},$$

which only varies between 0 and 0.6, and the range where it is most sensitive to polarisation is at the higher end of the lepton spectrum where few events occur.

The advantage of using different modes is that statistics are very much increased. Because it is required that *both* taus decay to a product which can be used to give polarisation information, very few events qualify. For example, using only π decays, for which the branching ratio is about 10% and the OPAL selection efficiency is less than 50%, only 5% of tau decays can be used. With almost 5,000 $e^+e^- \rightarrow \tau^+\tau^-$ events this means that only 5000×0.05^2 events, or about 12

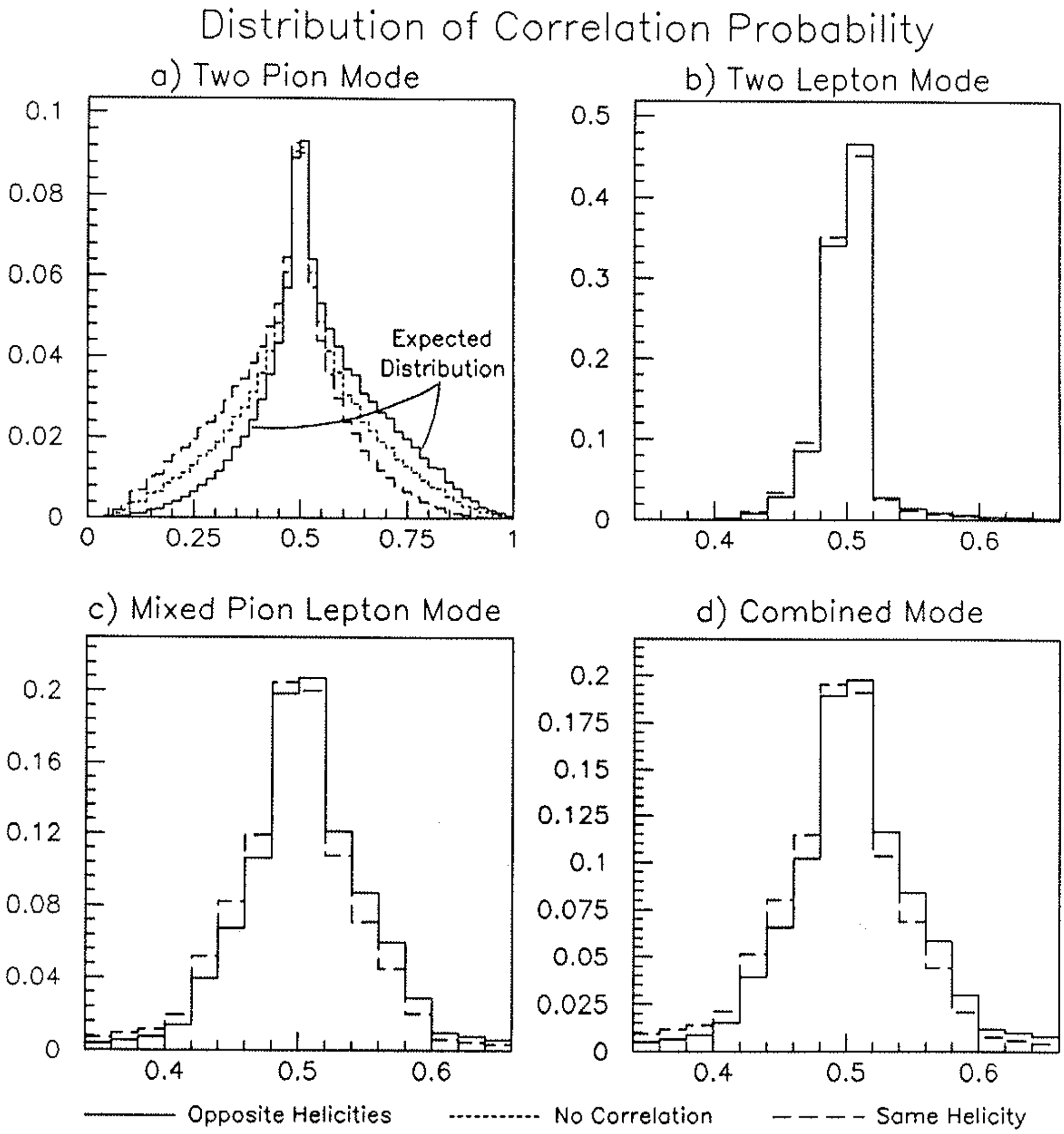

Figure 7.6: Various distributions of the correlation probability for different tau decay modes a) two pions b) two leptons c) one pion, one lepton d) combined modes with at least one pion — for final analysis.

useful events can be identified. However, if $\tau \rightarrow e\overline{\nu}_e\nu_\tau$ and $\tau \rightarrow \mu\overline{\nu}_\mu\nu_\tau$ events are included, more like 30% of decays can be used, increasing the number of useful events by a factor of about 40.

In order to determine the distribution of the correlation probability, it is now necessary to perform semi-analytic calculations. This was done for both the case where the two tau particles both decay to leptons and also when one decays to a lepton, and the other to a pion. The resulting distributions are shown in

Decay Mode	Efficiency	Background	Number
$\tau \to e\bar{\nu}_e\nu_\tau$	$79.9 \pm 1.3\%$	$5.7 \pm 1.3\%$	964
$\tau \to \mu\bar{\nu}_\mu\nu_\tau$	$82.2 \pm 1.7\%$	$3.0 \pm 0.6\%$	903
$\tau \to \pi\nu_\tau$	$37.7 \pm 1.3\%$	$6.0 \pm 1.6\%$	309

Table 7.1: Summary of selection statistics for tau decay modes.

figure 7.6(b) and (c). It is clear that the case where both taus decay to a lepton has very little power to distinguish between the two possibilities shown in the graph. It would require careful analysis and high statistics to provide a good result. However, the 'mixed' mode where one tau decays to a pion provides more separating power, so this has been included in the analysis.

7.2.3 Measurement of Polarisation Correlation

As shown above, it is possible to include data from $\tau \to \pi\nu_\tau$, $\tau \to e\bar{\nu}_e\nu_\tau$ and $\tau \to \mu\bar{\nu}_\mu\nu_\tau$ events in order to increase the accuracy of the investigation. Further decay modes could be used, but these are the easiest to analyse together, and OPAL has well established selection algorithms for them. However, the pion mode can only be well separated in the barrel region, and since it is important to have at least one pion decay in the events used, only the barrel region is used. The tau pair selection is the same as used in chapter 5, and the decay mode selections are those used for standard OPAL branching ratio analyses (see [30,36]). Note that the momenta of the electrons and pions are not defined in the same way as for the muon, since this would in general involve double counting of the energy. The electron momentum is taken just from the electromagnetic calorimeter energy, and the charged track momentum is used for the pion.

In the barrel region there are 3,308 selected tau pair events. Table 7.1 summarises the number of decay modes identified along with their efficiency and background. Only those events which have a selected decay of one of these three types at *both* ends can be used in the polarisation analysis. It is found that there are 5 events with both taus decaying to a pion, 263 events with two leptons, and 81 events with one $\tau \to \pi\nu_\tau$ decay and one leptonic decay.

In order to be able to analyse these events, it is necessary to produce the distribution of the correlation probability described in the previous section. The distribution for each type of event is known, but to optimise statistics, a combined distribution is produced. This is done by combining the distributions found in the proportions expected from the number of each decay mode seen. In order to imitate accurately the behaviour of the data, it is necessary to simulate the efficiency of the selection as a function of momentum, and also the average polarisation should be considered in order to give more decays with negative polarisation for the τ^-.

This is all done in one stage by producing a simplified Monte Carlo simulation of the momenta of the observed decay products taking into account all the above considerations. It is done in three ways:

1. assuming complete correlation - *i.e.* the taus have opposite helicities arising from the spin-1 of the Z^0
2. assuming no correlation between the two taus
3. assuming the two taus have the same helicity.

This combined distribution for the two extreme cases is shown in figure 7.6(d). In this case only the events with at least one pion have been considered. The shape of the graph can be parameterised as a function of a 'correlation factor' — set to 1 for the expected correlation, -1 for anti-correlation and 0 for no correlation. This variable can then be considered as a continuous variable which measures the degree of correlation. Anti-correlation would imply that the tau pair system had zero spin, in turn implying a zero spin assignment for the Z^0 particle.

With a suitable distribution defined, the data can now be fitted to theoretical prediction. The best fit is shown in figure 7.7. Note that the outer bins actually contain the events which overflow at each end. Obviously statistics are still a limiting factor, and the value given by this technique for the correlation factor is $0.4 \pm 0.8(stat)$.

The systematic error on this measurement is relatively small in comparison to the statistical error. It has been estimated using the Monte Carlo created events which were generated to determine the expected probability distribution. Samples of these were taken and errors introduced at the level expected in data,

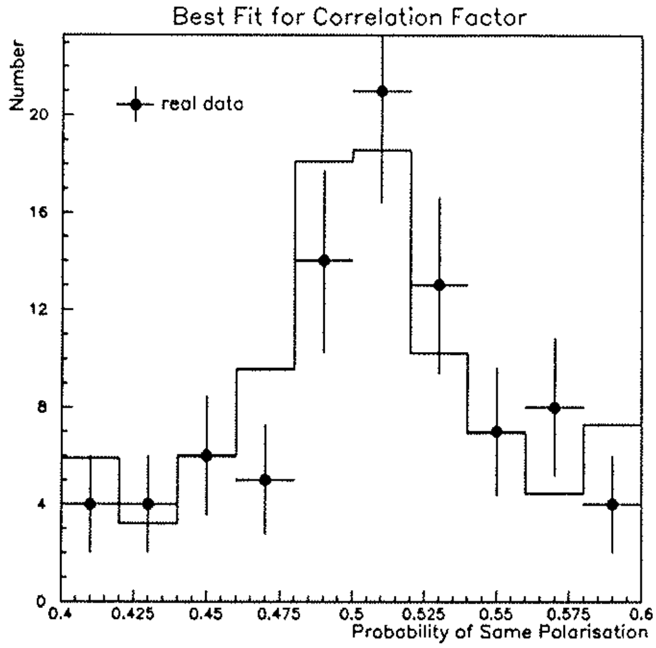

Figure 7.7: The best fit for correlation factor showing data and distribution.

i.e. momenta were smeared and, most importantly, events were 'misidentified' at the background level expected in the selected events. The resulting deviation in the fitted correlation factor was taken to be an estimate of the systematic error — about ± 0.3.

7.2.4 Result of Polarisation Correlation Studies

The final result for the correlation factor was a figure of $0.4 \pm 0.8(stat) \pm 0.3(sys)$. This is clearly not statistically significant as it only just excludes a spin correlation corresponding to zero spin for the Z^0 at the 2σ level. However, it shows that it would be possible to obtain a meaningful result with the sort of statistics which will soon be available. With LEP accumulating data all the time and with the addition of further decay modes into the analysis, this type of analysis should soon give a significant measurement. The next step is then to gather enough data to perform an experiment testing a prediction similar to 'Bell's inequality', as suggested at the start of this section. If LEP does not provide enough data for this, then a tau factory could also be used in a similar way.

Appendix A

The Muon Endcap Data Acquisition System

For purposes of data acquisition, the muon endcap detector is divided into three parts, called systems. These are the Near, Far and Patch systems. The near and far distinction is common to many sub-detectors at OPAL. Far corresponds to $x > 0$, and near to $x < 0$. This is partly to cope with the split nature of the detector and also to aid parallel processing of data. The data from each system are only brought together at a late stage before they are sent to OPAL central data acquisition. The operation of each of the three systems is very similar, and in principle only the readout ordering and numbering conventions are different.

Figure A.1 is a schematic diagram showing the complete processing chain. The purpose of each of the crates and its individual components is outlined below.

A.1 The System Controller Crate — SCC

In the quadrant systems, 8 Branch Controller Crates (BCC) are required to read out all the strips — only 4 are needed for the Patch system. Each one of these is connected directly to one Branch Interface unit (BIN) in the System Controller Crate (SCC). A large part of the task of the BIN is to store the data from digitised events in a Multi-Event Buffer (MEB). This buffer can store up to 14 events giving the readout a very high buffering capacity. The BINs also form an interface between the front-end and the dedicated triggering logic boards, and in

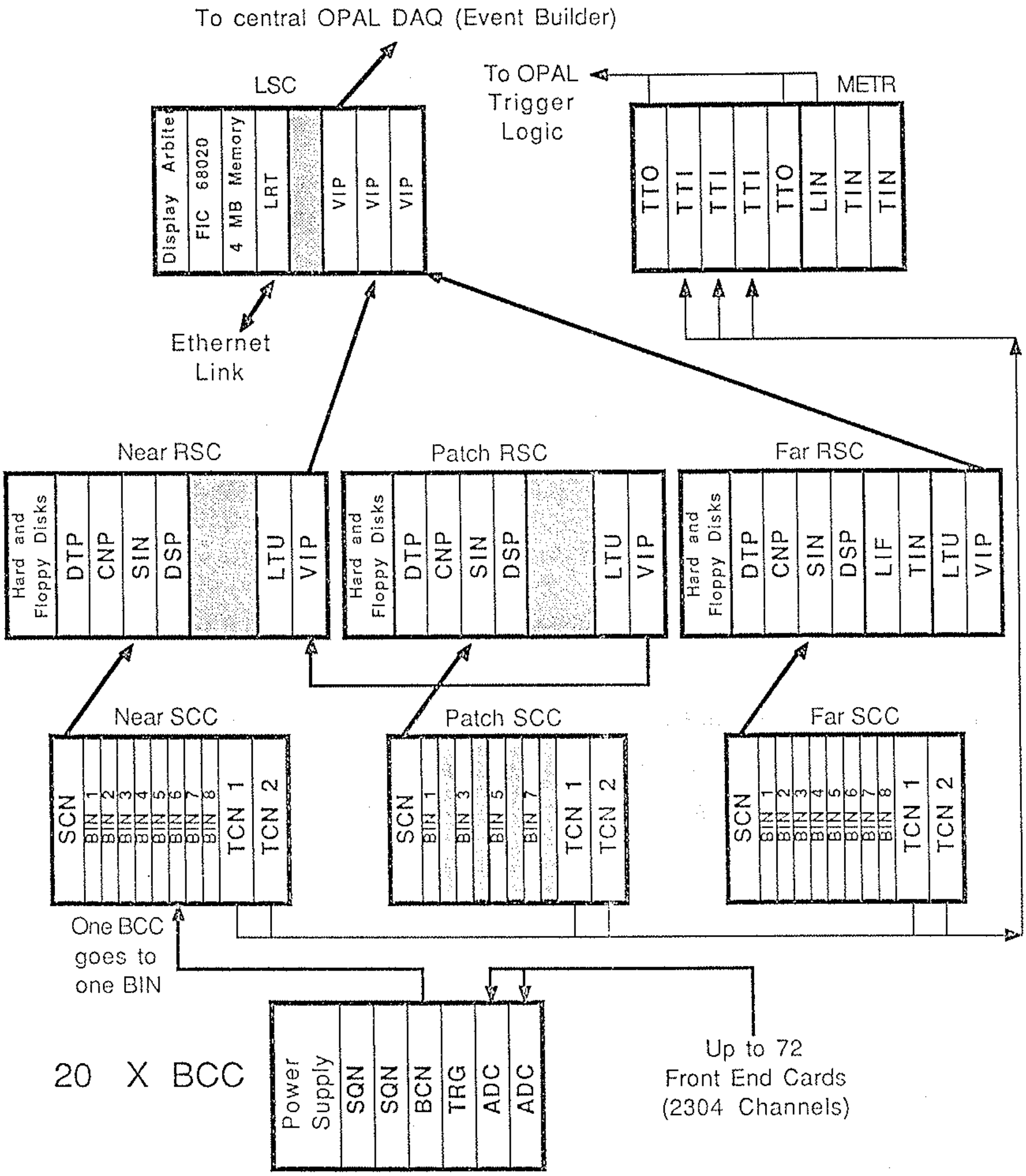

Figure A.1: The complete readout system.

fact perform the grading part of the trigger processing task.

The heart of the SCC is the System Controller board (SCN) which controls all activity within the SCC and BCCs on instructions from processors in higher crates. Its main task during data acquisition is to transfer events from the buffers in the BINs up to the next level of data acquisition and in doing so it uses a re-ordering algorithm programmed into some of its PROMs to organise the data into a more physical sequence than that in which the strips are digitised.

The only other contents of the SCC are the two Trigger Controller boards (TCNs). These form the backbone of the trigger processing from graded trigger channel signals formed in the BINs right through to theta-phi signals for the relevant area of the detector.

A.2 The Readout System Crate — RSC

This is the first crate up the readout chain to contain programmable CPUs rather than hardwired logic. The crate uses a VMEbus environment [37] for integration of processors. There are in fact three separate processors performing different parts of the data processing tasks in parallel to minimise delays in the data handling. The data are received from the SCC into another buffer called the SIN buffer (System INterface), where the processors can begin their tasks. The data are transferred from the Multi-Event Buffers to the SIN buffer in such a way that they are re-ordered from their original readout order to the more physical strip order. This makes the job of the processes running in the RSC microprocessors easier.

Details of the tasks of the three processors are given below.

1. **The Control Processor (CNP)**

   This is a MVME101 [38] processor running an assembler program called the System Control Program (SCP). In normal running, it is the master program which controls everything from the timing of the data processing in the RSC right down to requesting the data readout to start. It does this by sending commands down to the SCN. It also has to interact with the Local

Trigger Unit (LTU) in the crate to attach the correct OPAL trigger words and event number to an event. The LTU has a direct connection to the central trigger logic, and this provides most of the synchronisation signals needed for a sub-detector to fit in with OPAL timing.

2. **The Digital Signal Processor (DSP)**

   This is a dedicated processor for locating signals. It runs a simple algorithm to find streamer signals in the data stored in the SIN buffer [39]. A signal is typically a few strips with a value well above the pedestal value, but to avoid problems of threshold searching if, say, the pedestals drifted coherently, the program in fact looks for noticeable rises and falls indicating the possible edges of a signal. When such an event is found, it is flagged by pointers (called DSP pointers) which are later used by the final RSC process.

3. **The Data Processor (DTP)**

   This is a MVME147 [40] board containing the 68030 microprocessor [41] running under the OS9 operating system [42]. It uses the pointers found by the DSP to create a summary of the interesting parts of the data packed into a format similar to that eventually required by OPAL, although of course only containing data from part of the detector. Thus from the original 17,000 or so original 12 bit data words, the useful data should be packed into about 1 kByte of memory.

   The 147 has plenty of processing capacity, and as a lot of the time it is waiting for a new event to process, there is much scope for using it for monitoring purposes. This is done using SPY events. The SIN buffer contains a second area of data buffers called the SPY buffer. When requested, this can be filled with an exact copy of an event along with DSP pointers and this is maintained until it is released by the requesting program. Using this full information on an event, a useful collection of online histograms has been built up (for example see Appendix B).

The only other component of the RSC not mentioned above is the VIP card, which is a way of making the VME memory in the lower crate available to another

VME crate connected via another VIP. This provides an interface with the top level of the data acquisition.

A.3 The Local System Crate — LSC

The LSC is a standard OPAL online VME crate and common to all detectors as the top of the acquisition chain. It contains a Fast Intelligent Controller (FIC) [43], based on the 68030 microprocessor, as its main processor. For the Muon Endcap, the crate in fact performs little of the readout but instead it combines the data from the readout systems pulling the data over the VIPs and then sends the data up to the OPAL Event Builder where all the data from each detector are combined. It also performs further monitoring and histogramming tasks.

A.4 The Muon Endcap Trigger Crate — METR

This is a simple logic crate which performs two basic tasks. The first of these tasks is to form the final trigger signals to send to OPAL, *i.e.* both the theta-phi (TPM) signals and three single input mode (SIM) signals, as defined in section 2.3.9. It takes the signals in from the TCN boards (via the Trigger Transmitter Input boards — TTI). Then the Trigger Transmitter Output boards (TTO) OR together the signals corresponding to the same θ-ϕ bins. For example this will include the areas where the patches overlap with the quadrants. These are then passed out to their final destination in the OPAL muon theta-phi board. Also various ORing operations are performed in the TTOs and sent across the backplane to the Link Interface Near (LIN). This uses the ORed results to form the three SIM signals for OPAL central logic. There is a strap on the backplane connected to this board, and when the strap is removed, the simple non-collinear form of MELR is invoked (see section 4.1.1).

The other purpose of the trigger crate is to act as a general interface for trigger timing and synchronisation. The Trigger Interface boards (TIN) act as a relay for some of the synchronisation signals between the LTUs and the front end via a connection to the SCN board. There are only two TINs in the METR crate dealing with the Near and Patch systems. The TIN for the Far system is located in the RSC itself, as is the Link Interface Far (LIF). The purpose of the two Link Interfaces is to carry any other necessary information between the two sides. The most important of these for readout purposes is the far trigger strobe. The trigger strobes are flags set by the front end in each system to indicate if the trigger data for that system is ready. The METR crate on the near side has to know if the far system is ready since, until all the systems are ready, the final trigger signals output from the TTOs must be set to zero. This system ensures that no spurious triggers are sent before the logic circuits have settled to a stable value. The final signals are formed about 11 μs after beam crossing in time for the central trigger which starts its logic at 13 μs after beam crossing.